



HAL
open science

Experimental characterization of the interstitial pore pressure of wet concrete under high confining pressure

Abdallah Accary

► **To cite this version:**

Abdallah Accary. Experimental characterization of the interstitial pore pressure of wet concrete under high confining pressure. Chemical and Process Engineering. Université Grenoble Alpes, 2018. English. NNT : 2018GREAI040 . tel-01866716

HAL Id: tel-01866716

<https://theses.hal.science/tel-01866716>

Submitted on 3 Sep 2018

HAL is a multi-disciplinary open access archive for the deposit and dissemination of scientific research documents, whether they are published or not. The documents may come from teaching and research institutions in France or abroad, or from public or private research centers.

L'archive ouverte pluridisciplinaire **HAL**, est destinée au dépôt et à la diffusion de documents scientifiques de niveau recherche, publiés ou non, émanant des établissements d'enseignement et de recherche français ou étrangers, des laboratoires publics ou privés.

THÈSE

Pour obtenir le grade de

DOCTEUR DE LA COMMUNAUTÉ UNIVERSITÉ GRENOBLE ALPES

Spécialité : **Matériaux, Mécanique, Génie civil, Electrochimie (2MGE)**

Arrêté ministériel : 7 Août 2006

Présentée par :

Abdallah ACCARY

Thèse dirigée par : **Laurent DAUDEVILLE**
codirigée par **Yann MALECOT**

Préparée au sein du **Laboratoire 3SR Grenoble**
dans l'**École Doctorale Ingénierie - Matériaux, Mécanique, Environnement,
Énergétique, Procédés, Production (I-MEP2)**

Experimental characterization of the interstitial pore pressure of wet con- crete under high confining pressure

Thèse soutenue publiquement le : **4 Juin 2018**,
devant le jury composé de :

M. Christophe LANOS

Professeur, Université Rennes 1, Président

M. Nicolas BURLION

Professeur, Université Lille, Rapporteur

Mme. Siham KAMALI-BERNARD

Maître de Conférences, Insa Rennes, Rapporteur

M. Christophe PONTIROLI

Ingénieur de recherche, CEA Gramat, Examineur

M. Laurent DAUDEVILLE

Professeur, Université Grenoble Alpes, Directeur de thèse

M. Yann MALECOT

Professeur, Université Grenoble Alpes, Co-Directeur de thèse



"C'est impossible, dit la Fierté C'est risqué, dit l'Expérience C'est sans issue, dit la raison..Essayons, murmure le coeur" William Arthur Ward

Acknowledgment

First, I would like to express my deep and sincere gratitude to my research supervisors Laurent Daudeville and Yann Malecot for the help and guidance through the three years of the thesis. Un *GIGA* Merci pour vous.

In addition a special thanks to Jean-Luc Decosne who guided and taught me how to use the Giga press.

I would also like to thank the members of the jury for their participation in the thesis and specially Nicolas Burlion and Siham Kamali-Bernard for accepting to report my work. Also a Special thanks to my committee members Christophe Pontiroli and Christophe Lanos for accepting to assess the final presentation of my thesis.

I would like to thank all my PhD colleagues in the 3SR laboratory, with whom I have shared moments of deep anxiety but also of big excitement.

I would like to thank my parents, my sisters and brother for their unconditional support, encouragement and love. A big thanks to my mother for her caring and sacrifices for educating and preparing me for my future.

Last, but not least, I am very much thankful to my wife Reem for her love, understanding and continuing support to complete this research work. To my daughter Racha who enlighten my life one year ago.

Abstract

The main objective of this PhD thesis is to identify experimentally the interstitial pore pressure in a very wet concrete during a non drained hydrostatic compression at very high stress level (until 500 MPa). This work is a part of a more general project aiming to understand the concrete behavior under impact during which, a high triaxial stress state occurs. Massive concrete structures keep a saturation ratio strongly depth dependent almost their life time. Moreover, the quantity of free water contained in concrete pores has a preponderant role on its behavior under high confinement compared to other material parameters (e.g: water/cement ratio or the concrete porosity). These observations suggest that under such loading, the closure of concrete porosity causes an increase in the interstitial pressure. This latter exerts a major influence on concrete behavior on both the concrete strength capacity and shape of the limit state curve. However, this pore pressure has never been measured. A new interstitial pore pressure measurement technic, using the triaxial Giga press of the 3SR Laboratory, is proposed and tested in the first part of the this study. The concept consists in replacing the reference R30A7 concrete sample (14 cm in length) by a smaller one (8 cm in length) and a water collecting cap (6 cm in length) below it. Two types of pressure sensor have been developed during this thesis, a Hydrostatic and a Membrane type sensors. Each sensor is placed in the void space of the water collecting cap before the tests. When the sample is under hydrostatic pressure at high confinement, the pressurized free water inside the sample is transmitted to the sensor placed into the cap cavity through micro-holes. The design, protection and calibration of each pressure sensor are discussed. The second part of this thesis is devoted to the analysis of the interstitial pore pressure measurement results carried out on the very wet reference concrete (R30A7). The results reveal that the interstitial pressure can reach a value between 200 and 400 MPa under a mechanical confinement pressure of 500 MPa. Furthermore, analytical modeling, within the poro-mechanical framework based on the effective stress concept, is developed to estimate the interstitial pressure and the volumetric behavior of concrete under high confinement. The model shows promising results while comparing it to the experimental values.

Keywords: Wet concrete, Hydrostatic test, High confinement, Pore pressure measurement, Sensor

Résumé

L'objectif principal de cette thèse est d'identifier expérimentalement la pression interstitielle d'un béton très humide durant une compression hydrostatique non drainée sous forte pression de confinement (jusqu'à 500 MPa). Ce travail fait partie d'un projet plus général visant à comprendre le comportement des structures en béton soumises à un impact au cours duquel, un état de contraintes triaxiales élevées se produit au sein du matériau. Ces structures en béton, souvent massives, gardent un taux de saturation assez élevé durant leur durée de vie. La quantité d'eau libre dans les pores du béton a un rôle prépondérant sur son comportement sous confinement élevé par rapport à d'autres paramètres du matériau (par exemple: rapport eau / ciment ou porosité du béton). Ces observations laissent supposer que sous une très forte charge, la fermeture de la porosité du béton provoque une augmentation de la pression interstitielle. Celle-ci entraînerait à la fois une forte baisse de la résistance au cisaillement et de la compressibilité du béton. Or cette pression interstitielle n'a jamais été mesurée. Une nouvelle technique de mesure de pression interstitielle en utilisant la presse triaxiale Giga du laboratoire 3SR est proposée et testée dans la première partie de cette étude. Elle consiste à remplacer l'échantillon de béton (14 cm en longueur) par un autre plus petit (8 cm de longueur) et une enclume de collecte d'eau (6 cm de longueur) placée en dessous. Deux types de capteurs de pression ont été développés durant cette thèse, un capteur type Hydrostatique et un de type Membrane. Chacun des deux capteurs de pression est placé dans l'espace libre de l'enclume avant chaque essai. Lorsque l'échantillon est sous compression hydrostatique, la mise en pression de l'eau libre de l'échantillon est transmise au capteur dans la cavité par le biais des micro- trous. La conception de chaque capteur, la protection de l'ensemble et les essais d'étalonnage des capteurs de pression sont discutés. La deuxième partie de cette thèse est dédiée aux analyses des résultats de mesure de la pression interstitielle effectuées sur des échantillons très humide d'un béton de référence (R30A7). Les résultats révèlent que la pression interstitielle peut atteindre une valeur comprise entre 200 et 400 MPa pour une pression de confinement mécanique égale à 500 MPa. De plus, une modélisation analytique, utilisant le cadre de la poro-mécanique et se basant sur le concept des contraintes effectives, est développée afin d'estimer la pression interstitielle et le comportement volumique du béton sous confinement élevé. La comparaison des résultats de mesure et de modélisation est satisfaisante.

Mots clés: Béton humide, Essai hydrostatique, Confinement élevé, Mesure de pression interstitielle, Capteur

Contents

Abstract	i
Résumé	iii
Introduction	1
1 Bibliographic study	5
1.1 Introduction	5
1.2 Concrete Meso-constituants behavior	5
1.3 Effect of water presence on concrete behavior	7
1.3.1 Static simple compression test	7
1.3.1.1 Effect of W/C ratio	7
1.3.1.2 Effect of initial matrix porosity	8
1.3.1.3 Effect of saturation ratio	9
1.3.2 Static triaxial behavior of concrete	10
1.3.2.1 Effect of W/C ratio	11
1.3.2.2 Effect of initial matrix porosity	12
1.3.2.3 Effect of saturation ratio	14
1.3.3 Static quasi-oedometric test: effect of saturation ratio	16
1.3.4 Dynamic behavior of concrete	18
1.3.4.1 Dynamic quasi-oedometric test: effect of matrix porosity	18
1.3.4.2 Static and dynamic shear test: effect of free water	20
1.3.4.3 Dynamic tensile test: effect of saturation ratio	21
1.3.5 Conclusion	22
1.4 Modeling of concrete under impact: effect of free water	24
1.4.1 Continuous model	25
1.4.2 Discrete model	26
1.5 Pore pressure measurement under low confinement pressure	28
1.5.1 Test on concrete	28
1.5.2 Test on rock	30

1.6	Poro-mechanic behavior of geo-materials	32
1.7	Conclusion	34
2	Experimental procedure	35
2.1	Introduction	35
2.2	Formulation and conservation of the studied concrete	35
2.3	Specimen preparation	36
2.3.1	Concrete fabrication	36
2.3.2	Coring and Surface machining	36
2.3.3	Porosity measurement: pores accessible to water	37
2.4	Simple compression test	39
2.4.1	Schenck press presentation	39
2.4.2	Test results	40
2.5	Triaxial test set up	41
2.5.1	Device presentation	41
2.5.2	Loading paths	42
2.6	GIGA press instrumentation	43
2.6.1	Introduction	43
2.6.2	Pressure measurement	43
2.6.3	Strain measurement	43
2.6.3.1	Concept	43
2.6.3.2	LVDT calibration test	44
2.7	Water collect cap system	45
2.7.1	Drainage cap conception	46
2.7.1.1	Provisional concept	46
2.7.1.2	Adapted concept	47
2.7.2	Instrumentation and protection	48
2.7.3	Calibration test concept	50
2.8	Conclusion	51
3	Development of the pore pressure sensor	53
3.1	Introduction	53
3.2	Aluminum sensor: hydrostatic type	54
3.2.1	Sensor description and design	54
3.2.2	Sample position	55
3.2.3	Sample protection	56
3.2.4	Sensor calibration test	58
3.2.5	Interstitial pore pressure measurement in concrete samples	61
3.3	Membrane sensor	64
3.3.1	General description and design	64
3.3.1.1	Loading and boundary conditions	66
3.3.1.2	Stress analysis	67
3.3.1.3	Sensitivity analysis	68

3.3.1.4	Geometry validation	71
3.3.1.5	Mechanical effect	71
3.3.2	Experimental procedure	75
3.3.2.1	Sensor protection	75
3.3.2.2	Cap and sensor set up	75
3.3.3	Full bridge: diaphragm patterns	77
3.3.3.1	Numerical application	78
3.3.3.2	Calibration test	79
3.3.4	Quarter bridge: single gage	81
3.3.4.1	Calibration test	81
3.3.4.2	Interstitial pore pressure measurement in concrete sam- ples	84
3.4	Comparison between the hydrostatic and the membrane type sensor	85
3.5	New concept for pore pressure measurement	85
3.6	Conclusion	87
4	Result analysis of the interstitial pore pressure measurements	89
4.1	Introduction	89
4.2	Interstitial pore pressure tests results	89
4.3	Influence of confinement pressure	90
4.4	Influence of loading rate	93
4.5	Concrete volumetric behavior	94
4.6	Conclusion	97
5	Modeling of concrete interstitial pore pressure	99
5.1	Introduction	99
5.2	Effective stress concept in PRM model	99
5.2.1	Serial and parallel approach	100
5.2.2	Poro-mechanical approach	102
5.3	Concrete behavior under high confining level	104
5.4	Evaluation of the pore pressure	107
5.4.1	Influence of the initial porosity and saturation ratio	109
5.5	Pore pressure comparison	111
5.6	Experimental identification of the Biot coefficient	113
5.7	Conclusion	115
	Conclusion and perspectives	117
	Bibliography	121
	List of Figures	131
	List of Tables	139

Introduction

Understanding the response of concrete structures subjected to impact loading became an important issue in the last decades. During extreme loading situations such as denotation load on sensitive structures (e.g. nuclear power plant, bridges and dams), concrete material undergoes complex behavior. Three major phases linked to this type of loading can occur. From concrete scabbing through tunneling and finally spalling in its opposite face, these phases are associated with multiple damage modes, (Figure 1), [Zukas, 1992], [Gran and Frew, 1979], [Daudeville and Malecot, 2011].

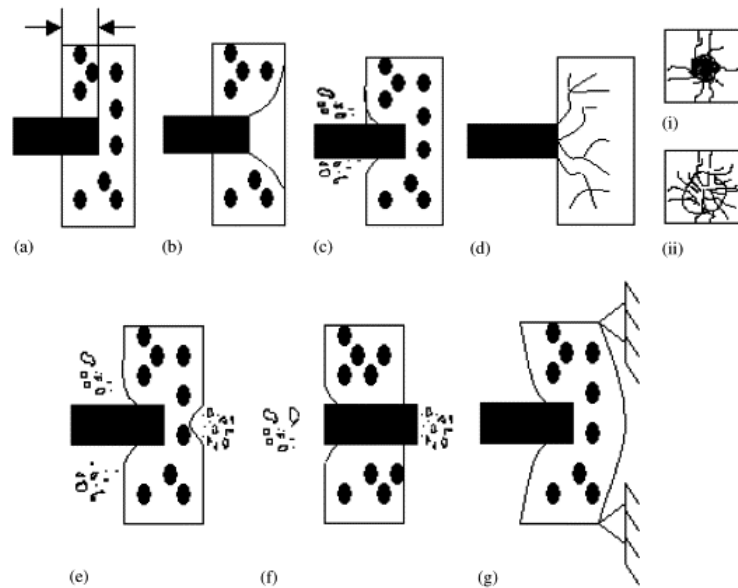


Figure 1: Missile impact effects on concrete target: (a) penetration (b) cone crack-ing (c) spalling (d) cracks on (i) proximal face and (ii) distal face (e) scabbing (f) perforation and (g) overall target response, [Li et al., 2005]

In fact, during the tunneling phase, a uni-axial compressive state stress is observed in front of the projectile nose. High level of confinement occurs due to inertia effect provided from material around the impactor. In consequence, the mortar surrounding the aggregates, known as a porous material, exhibits porosity closure. This solicitation induces damage diffusion in the cementitious matrix and an instantaneous material degradation leading to concrete compaction [Burlion et al., 2001].

Starting from this point, a research project has been launched in 2004 aiming to characterize the concrete triaxial behavior under high confinement. The overall program is financed by the CEA/DGA where their contributions led to install the GIGA press in the 3SR laboratory. Subsequent experimental studies were carried out on the press to study the effect of: loading path [Gabet, 2006], saturation and water over cement ratios [Vu, 2007], coarse aggregates shape and composition [Piotrowska and Forquin, 2014] and the initial matrix porosity [Zingg, 2013] on concrete behavior under triaxial test at high confinement. One of the important results is the observation of the compaction phenomenon and the porosity closure of the reference R30A7 concrete as illustrated in (Figure 2), [Poinard et al., 2012].

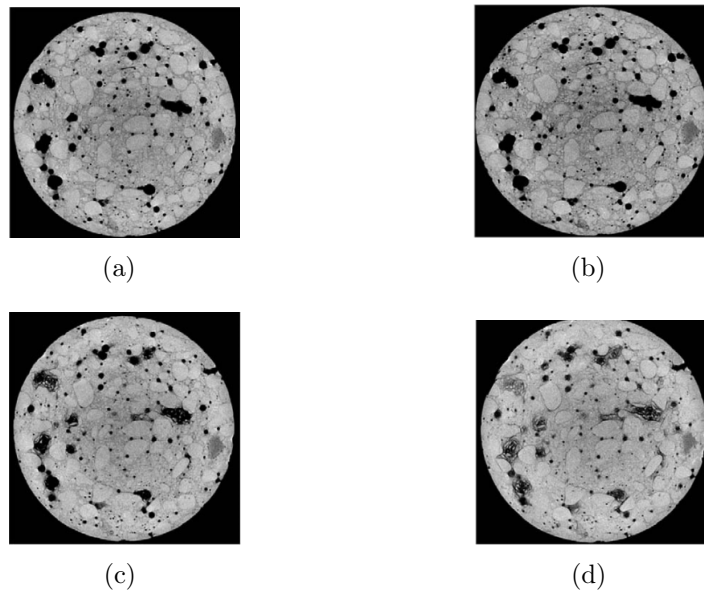


Figure 2: Horizontal slice of the R30A7 sample for an hydrostatic cyclic loading: (a) initial state (b) at 200 MPa (c) 400 MPa (d) 650 MPa, [Poinard et al., 2012]

Since sensitive structures are usually made from massive concrete, their saturation ratio is not homogeneous. They retain a quasi-saturated core throughout most of their lifetime, even though their face dries very quickly, [Baroghel Bouny et al., 1999]. This

means that concrete structure response under impact is highly influenced by the state of water saturation into the material.

Thus, the main objective of this thesis is to measure the interstitial pore pressure due to pores closure into a very wet concrete under high confining pressure and quasi-static loading. The overall work is performed on the Giga press. This objective implies a deep understanding of the concrete behavior under such loading for which the bibliographic study is dedicated. This chapter presents the effect of the water over cement ratio, the saturation ratio and the initial porosity on the behavior of concrete under unconfined and confined static conditions. The influence of these components on the concrete behavior is also investigated under dynamic load conditions (e.g: dynamic tensile, shear and impact solicitations). It is shown that the presence of water inside concrete pores has a preponderant role on its behavior under almost all types of loading. As the pore pressure magnitude remains a pending issue and in order to validate this hypothesis, its measurement becomes necessary. Numerical models of impact test using the finite elements or the discrete elements approach are briefly described. The chapter ended up with some previous pore pressure results conducted on concrete and rock at low confining pressure and with Biot's coefficient identification. Overviews about the technics used to measure the pore pressure are shown. Most of tests are done by applying the pore pressure which is controlled by means of valves and pump. However, in some cases the pressure is measured by means of transducers.

The second chapter is devoted to present the experimental procedure followed in this thesis. On the one hand, concrete formulation, fabrication and preparation procedure are described. Concrete compressive strength validation test with samples conservation are detailed. A general overview of the Giga press and its components serving to conduct test in the good conditions are presented. The Giga press does not have an integrated system to conduct a drained test and since the pore pressure systems shown in the literature review are not compatible with the Giga press mobile device, the chapter ends by presenting a new device called the *water collecting cap*. It allows the passage of water from the sample to its cavity by means of micro-holes. It is worth to note that [Hart, 2000] used the idea of a water collecting cap while performing triaxial undrained tests on rocks. Each specimen was sandwiched between two caps. The lowest cap part was designed to receive a transducer in order to measure the pore pressure, (Figure 3).

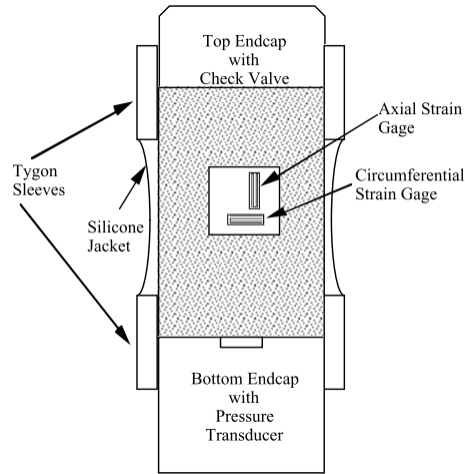


Figure 3: Lower cap equipped with a pressure transducer, [Hart, 2000]

In this study, the designed water collecting cap is equipped with a deformable sensor. Two sensors configurations are presented in the third chapter. The first one is a Hydrostatic type sensor that works under hydrostatic loading. The second is a Membrane type sensor acting under flexure and allowing higher strains. The design of each sensor and the gages choice were inspired from [William and William, 1992] book. The calibration and validation of each sensor by means of hydrostatic tests at high confinement pressure is detailed. The protection of the device should be done very carefully to avoid any mixing between water and confining fluid or the detachment of gages during the test.

In the fourth chapter, the effect of confinement pressure and loading rate during concrete pore pressure measurement are discussed. It is demonstrated that pore pressure could reach very high values during hydrostatic test at high confinement. In addition, concrete volumetric behavior measured during the test is compared to the one performed on the same reference concrete but under undrained condition. Experimental results allow identifying the Biot's coefficient by using the poro-mechanical theory approach. A poro-mechanical approach based on the concept of effective stress is presented in the last chapter. The aim of this model is to simulate the evolution of the concrete pore pressure and the volumetric behavior. At the end, conclusions and discussions are drawn based on the results and the perspectives raised by this work are proposed.

Chapter 1

Bibliographic study

1.1 Introduction

This chapter deals with the understanding of the degradation mechanism of concrete related to the presence of free water under different stress levels and strain rates. These mechanisms which have a very slight influence on concrete behavior under unconfined compression test are strongly pronounced at high confining pressure. The effects of the cement matrix porosity, initial porosity, saturation ratio and strain rate on concrete behavior under static and dynamic loading paths obtained previously will be shown. The static tests presented herein are performed under unconfined and confined conditions. This latter is reached by means of either an active confinement (GIGA press) or a passive one (confinement cell). In addition, the presented dynamic tests performed by many authors are all executed by using the Hopkinson bar technique. By adjusting the bars position and samples shape, they were capable to generates several loadings type such as compressive, tensile and shear. It will be shown that the free water in concrete has a preponderant role. Subsequently, methods used to measure the interstitial pore pressure into geo-materials (e.g. rocks, concrete) during static test at low confinement pressure will be presented.

1.2 Concrete Meso-constituants behavior

In its simplest form, concrete is a mixture of paste and aggregates or rocks. The paste, composed of cement and water, coats the surface of the fine and coarse aggregates. Through a chemical reaction called hydration, the paste hardens and gains strength

to form the concrete. [Akers and Phillips, 2004] have conducted tests on concrete, as well as the two materials that make up its meso-structure, namely rock (dolomitic limestone) and mortar under the following loading paths: simple compression, hydrostatic test up to 500 MPa and triaxial test at 300 MPa of confinement. Results of hydrostatic test on cited material are shown in (Figure 1.1). Aggregates, concrete and mortar show the same behavior due to the compaction process. Yet, the compaction of the mortar is significantly larger than that of concrete. This result is not surprising giving that the porosity of the cement matrix is greater than the concrete which is affected by the presence of aggregates. In opposite, tested limestone shows a brittle elastic behavior without any compaction phase. This reveals a high level of rigidity compared to the mortar and concrete materials.

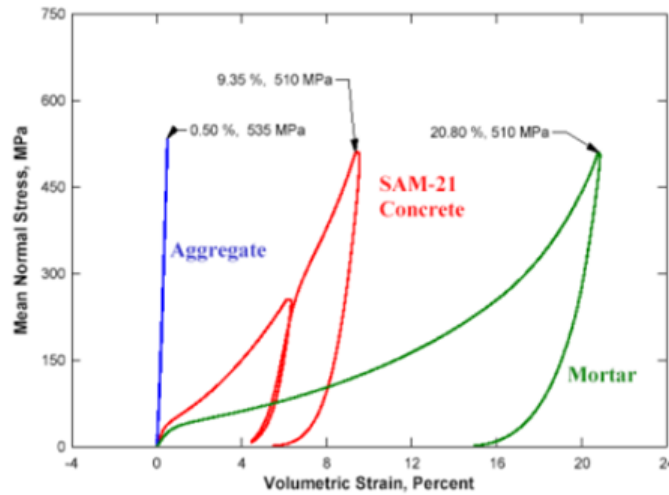


Figure 1.1: Volumetric behavior in hydrostatic test for three materials: limestone rocks, SAM21 concrete and mortar, [Akers and Phillips, 2004]

Similarly, the response of the limestone shows higher rigidity and resistance compared to other material for the simple compression test illustrated in (Figure 1.2: left). However, the ratio between rock and concrete strength decreases considerably from 5.8 for simple compression to 1.2 for triaxial compression (Figure 1.2: right). The behavior of mortar and concrete are relatively close with and without the confining pressure. Nonetheless, beyond a given strain level concrete exhibits plastic-hardening behavior similarly to the rock, while slight softening is observed for mortar.

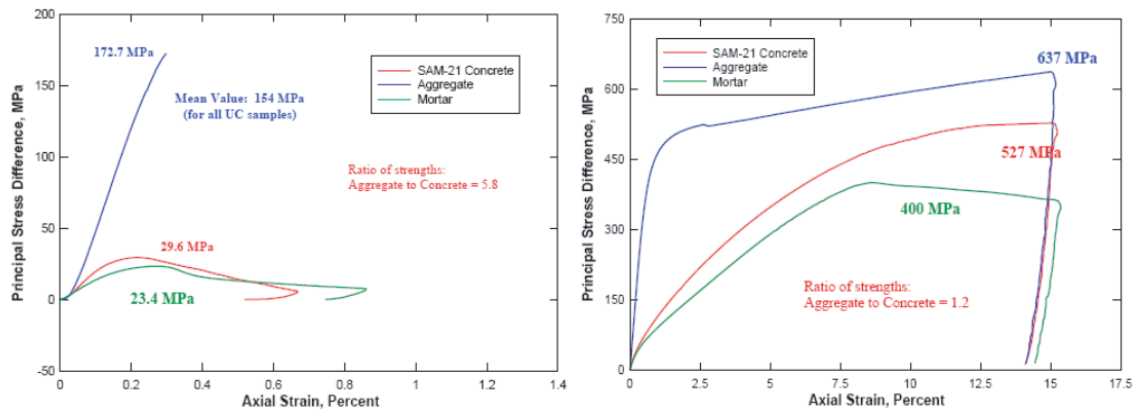


Figure 1.2: Mechanical behavior of the limestone rocks, SAM21 concrete and mortar subjected to: (left) simple compression test (right) triaxial test at 300 MPa of confinement, [Akers and Phillips, 2004]

1.3 Effect of water presence on concrete behavior

Concrete is a heterogeneous material basically made up of cement, aggregates and water. Widely used for construction purpose, it has always been investigated to improve its performance. Several types of concrete exist depending on its usage, from ordinary to ultra high performance concrete, where its macroscopic behavior is directly linked to the characteristics of its components. However, concrete types are obtained by modifying one of its principal components such as water over cement ratio, the initial porosity and even the coarse aggregate composition or shape. Subjected to quasi-static or dynamic loading, concrete behavior is highly influenced by the amount of free water (not hydrated) inside its pores.

1.3.1 Static simple compression test

The effect of water over cement ratio (W/C), initial matrix porosity ϕ_0 and saturation ratio (S_r) on concrete behavior under unconfined compressive are presented herein. It is worth to note that the influence of these properties overlap during tests which makes the analysis more complicated.

1.3.1.1 Effect of W/C ratio

Starting from its basic characteristic, concrete compressive strength has been deeply investigated by means of simple compression test. Many authors, [Ferret, 1892] and

[Bolomey, 1935], have been linked the effect of the water over cement ratio to the concrete compressive strength. The works of [Bolomey, 1935] permits to determine the concrete resistance f_c at 28 days thanks to (eq. 1.1) where G' is the compressive strength at 24 days and K the coefficient which depends on the quality of the cement paste.

$$f_{c28} = KG'(C/W - 0.5) \quad (1.1)$$

High-quality concrete is produced by lowering the W/C ratio as much as possible without sacrificing the work-ability of fresh concrete. So that, for a given saturation state, the higher the W/C ratio is, the higher the void into concrete is. To illustrate on this point, [Vu, 2007] carried out a series of simple compression on the ordinary concrete called (R30A7: f_{c28} equal to 30 MPa and slump equal to 7 cm) with different W/C ratios (0.8; 0.64; 0.4) (Figure 1.3: left). It is observed that the concrete behavior is highly influenced by W/C ratio under unconfined condition. The higher W/C ratio is, the weaker the concrete becomes. Same results are obtained by [Yurtdas et al., 2005] on mortar (Figure 1.3: right).

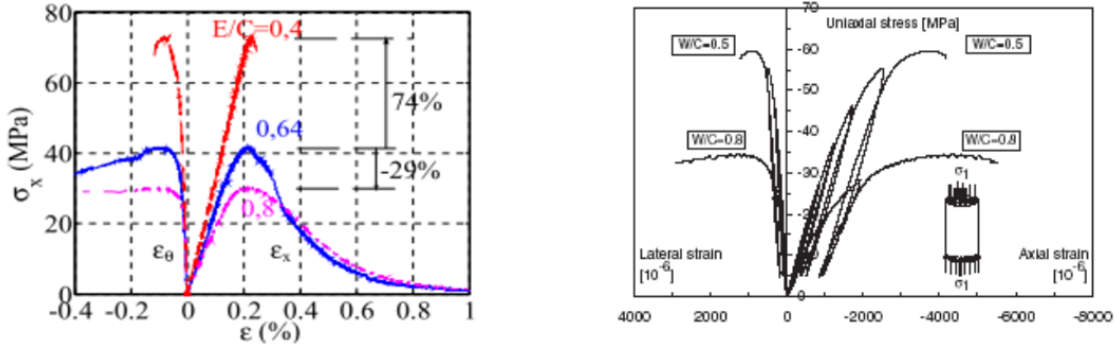


Figure 1.3: Simple compression tests with different(W/C) ratios: (left) R30A7 concrete, [Vu, 2007] (right) mortar samples, [Yurtdas et al., 2005]

1.3.1.2 Effect of initial matrix porosity

The effect of initial matrix porosity has been investigated by performing a series of simple compression tests on three different concrete types by [Zingg et al., 2016]. The ordinary concrete (R30A7), a light porous concrete at the level of capillaries named (LPC: f_{c28} equal to 24 MPa) with an initial porosity equal to 8%, and a high porous concrete named (HPC: f_{c28} equal to 78 MPa) with an initial porosity equal

to 15%. Results revealed that, the higher the porosity is, the lower the compressive resistance of concrete is, (Figure 1.4: left). In consequence, concrete volumetric stiffness decreases as its porosity increases, (Figure 1.4: right).

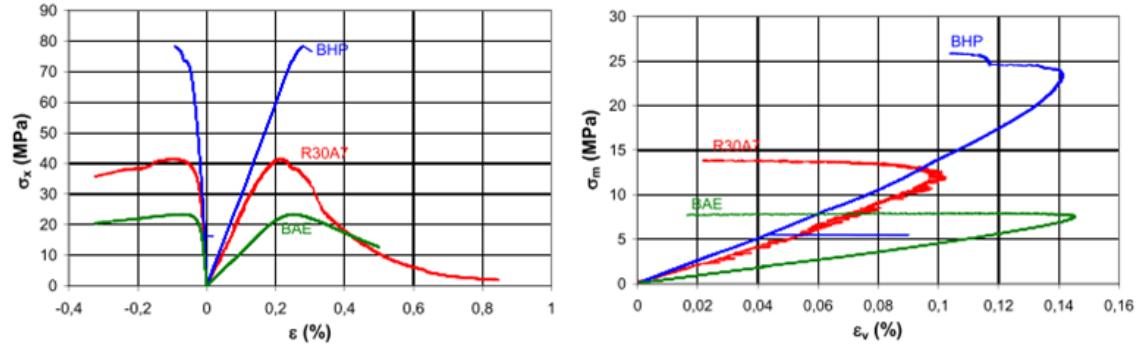


Figure 1.4: Simple compression tests on R30A7, LP and HP concretes with different initial matrix porosities (ϕ_0): (left) axial stress vs. strains (right) mean stress vs. volumetric strain, [Zingg et al., 2016]

1.3.1.3 Effect of saturation ratio

In the same way [Vu et al., 2009] and [Zingg, 2013] have performed simple compression tests by varying the saturation ratio of the ordinary (R30A7) and the high performance (HP) concretes consecutively. Figure 1.5 depicts the evolution of the axial stress versus the strains components for uniaxial compression test on the R30A7 and on the HP concretes.

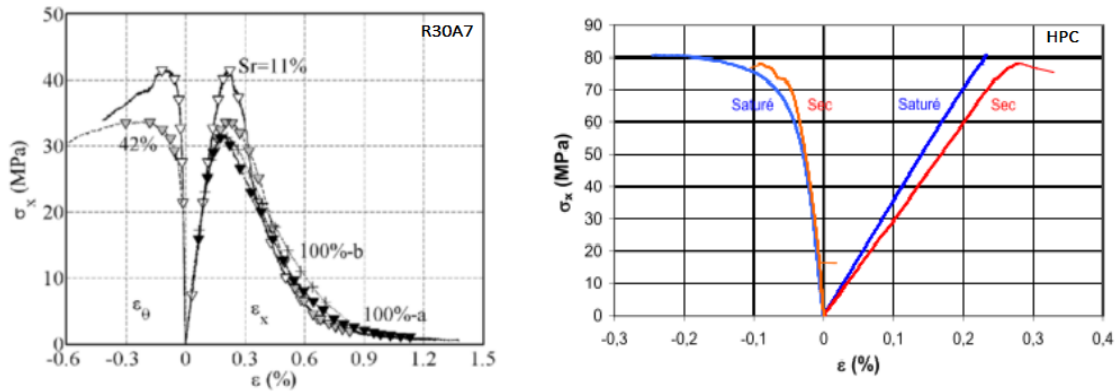


Figure 1.5: Simple compression test compression with different saturation ratios (S_r): (left) R30A7, [Vu, 2007] (right) HP concrete, [Zingg, 2013]

One has to note that the initial porosity of the R30A7 (ϕ_0 equal to 11 %) is higher than the HPC one (ϕ_0 equal to 8 %). The curves show that the concrete behavior in uniaxial compression is not considerably affected by the saturation ratio. A slight difference between the maximum stress reached for both states is clearly observed. Such a result leads to say that free water in concrete has a slight effect on its compressive strength.

1.3.2 Static triaxial behavior of concrete

The behavior of concrete under high levels of confinement is of significant importance in several engineering problems (e.g: pre-stressing reinforcement, bridge piles, high rise buildings and impact of projectiles). Thus, many researchers have studied the behavior of concrete and mortar under triaxial compression, [Bazant et al., 1986][Burlion, 1997], [Sfer et al., 2002], [Gabet, 2006], [Montenegro and Carol, 2007]. During a triaxial compressive test the sample, which is sandwiched between two caps, is first compressed hydrostatically by applying a homogeneous compressive pressure p all around it until the desired value and then it is compressed vertically by applying an axial force F_a , (Figure 1.6: left).

The device might be equipped by an LVDT and three gages, (Figure 1.6: right). The LVDT and the axial gage gives the sample axial strain ϵ_a globally and locally consecutively. The two circumferential gages gives the sample radial strain ϵ_r in tow opposite positions. The relation between the volumetric strain, the axial and circumferential strains during hydrostatic test are given in (eq. 1.2a). In addition, the applied axial force F_a with the known area A serves to estimate the axial σ_x and then the deviatoric q stresses (eq. 1.2b, 1.2c). At the end the mean stress is calculated based on (eq. 1.2d).

$$\epsilon_v = \epsilon_a + 2\epsilon_r \quad (1.2a)$$

$$\sigma_x = \frac{F_a}{A} \quad (1.2b)$$

$$q = \sigma_x - p \quad (1.2c)$$

$$\sigma_m = \frac{q + 2p}{3} \quad (1.2d)$$

In the same manner, this section shows the influence of concrete constituents (e.g: W/C, ϕ_0 and S_r on its confined behavior.

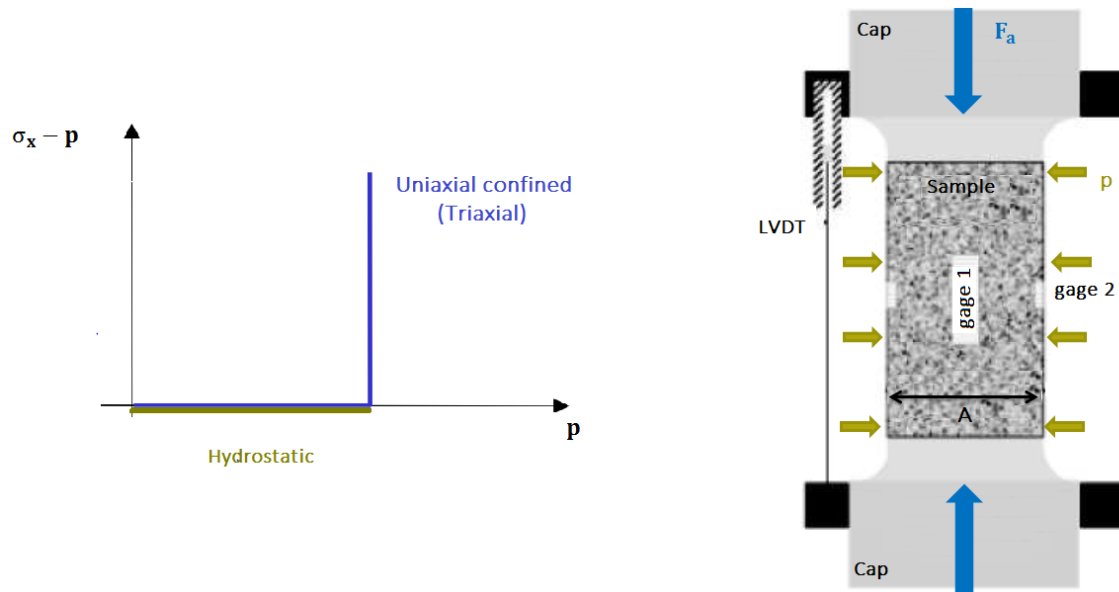


Figure 1.6: Triaxial test concept: (a) loading path (b) sample device used for strain measurement

1.3.2.1 Effect of W/C ratio

The effect of water over cement ratio has been also studied under high mean stress. [Vu, 2007] has pointed out on this subject by performing triaxial tests on the R30A7 concrete for different W/C ratios under intermediate and high confining pressure. The concrete volumetric behavior illustrated in (Figure 1.7) show that decreasing the W/C ratio, which means decreasing the void into the cement paste, tends to decrease the level of volumetric deformations reached at low and high confinement. These results could be explained by the gap of porosity due to the variation of W/C ratio.

The deviatoric behavior of concrete for different W/C ratios is also shown in (Figure 1.8). At low confining pressure (100 MPa), the concrete behavior is strongly linked to the cement paste strength. The concrete with the lower W/C (0.4) ratio reached higher shear strength than the two concretes with W/C (0.64 and 0.8), (Figure 1.8: left). However, at high confining pressure, all the studied concretes with different W/C ratios exhibit the same behavior (Figure 1.8: right). Thus, the concrete behavior is more like a granular stacking under high confinement. It is clearly appearing that reducing the W/C ratio tends to increase the strength of the concrete, as the porosity decreases at low confining pressure. The W/C ratio has an influence on the volumetric behavior of concrete which is not pronounced on its deviatoric behavior under high confining pressure.

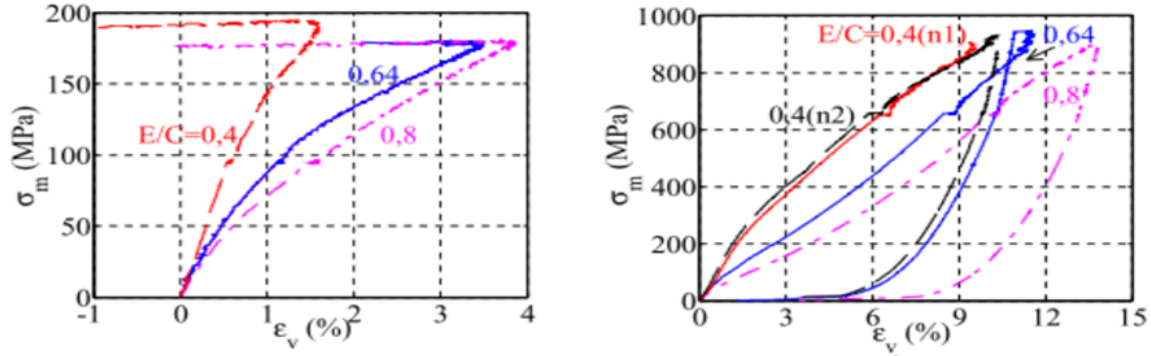


Figure 1.7: Volumetric behavior of ordinary concrete with different W/C ratio under triaxial loading. Mean stress vs. volumetric strain at: (left) 100 MPa (right) 600 MPa of confinement, [Vu, 2007]

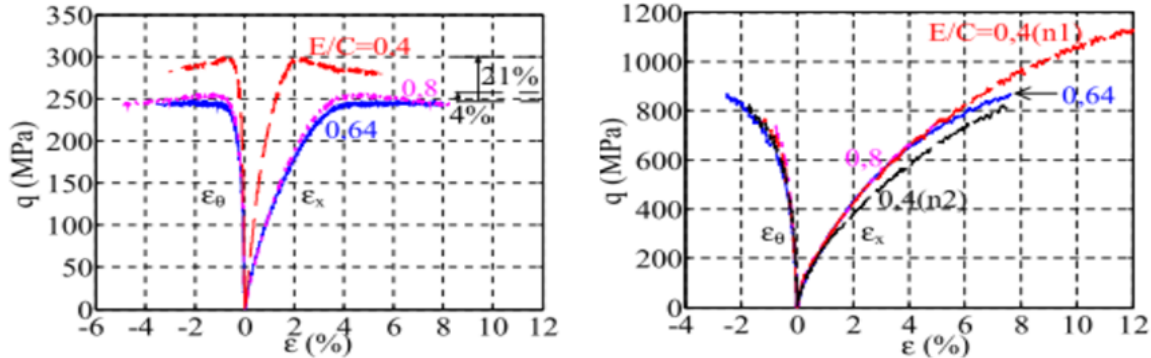


Figure 1.8: Deviatoric behavior of ordinary concrete with different W/C ratio under triaxial loading. Deviatoric stress vs. strains at: (left) 100 MPa (right) 600 MPa of confinement, [Vu, 2007]

1.3.2.2 Effect of initial matrix porosity

In a similar way, the initial matrix porosity effect on the concrete behavior under high confinement is evaluated by performing triaxial tests on the ordinary, light and high performance concretes [Zingg et al., 2016]. Concrete volumetric behavior results for 50 and 600 MPa of confining pressure are displayed in (Figure 1.9).

At low confinement pressure, the cementitious matrix of the three concretes remains very cohesive and a linear behavior response is observed. At high confinement pressure, concrete has a different response according to its initial porosity. The compaction phase starts earlier and is more pronounced for high porous concrete since pores volume are higher leading to a higher volumetric strain. Despite the difference

between concretes behavior at low confinement pressure, the initial deviatoric stiffness increases when the porosity of concrete decreases (the confinement damages the most porous concrete).

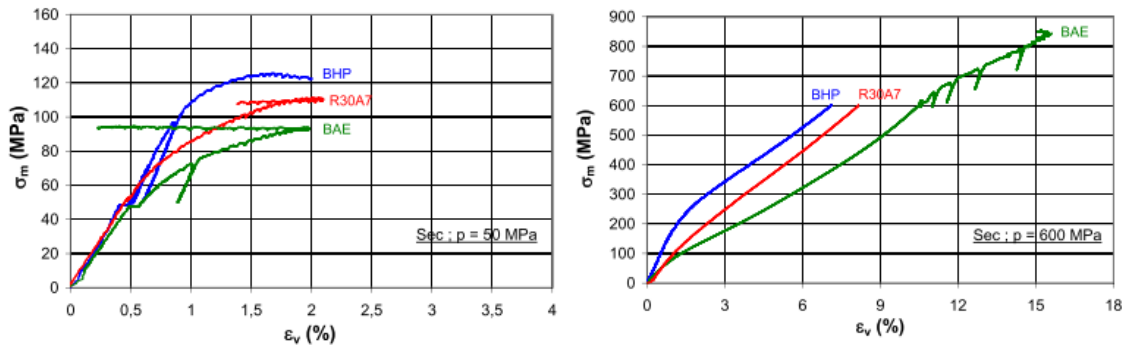


Figure 1.9: Volumetric behavior of R30A7, LP and HP concretes. Mean stress vs. volumetric strain at: (left) 50 MPa (right) 600 MPa of confinement, [Zingg et al., 2016]

This effect vanishes while comparing their deviatoric behavior at high confining pressure refer to (Figure 1.10). The initial deviatoric stiffnesses of the three concretes are apparently identical since the material is considered fully compacted (porous are closed), and thus the granular skeleton, which is the same for three concretes, controls their behavior.

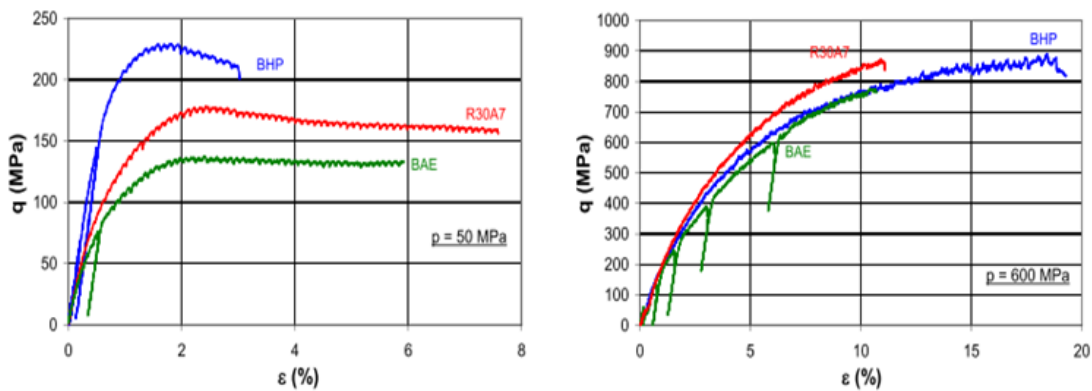


Figure 1.10: Deviatoric behavior of concretes of R30A7, LP and HP concretes. Deviatoric stress vs. axial strain under: 50 MPa (left) (right) 600 MPa of confinement, [Zingg et al., 2016]

1.3.2.3 Effect of saturation ratio

As shown in the previous section, the initial matrix porosity has an influence on the volumetric behavior of concrete at high stress level. However, this effect vanishes while comparing the deviatoric behavior of concretes under high confinement. So that, an important question could appear: what are the consequences on concrete triaxial behavior if those pores are filled by water. To enlight this subject, triaxial tests on the three types of concrete, at the dry and saturated states, have been carried out for different confining pressure, [Vu, 2007] and [Zingg, 2013]. Results are shown in (Figure 1.11).

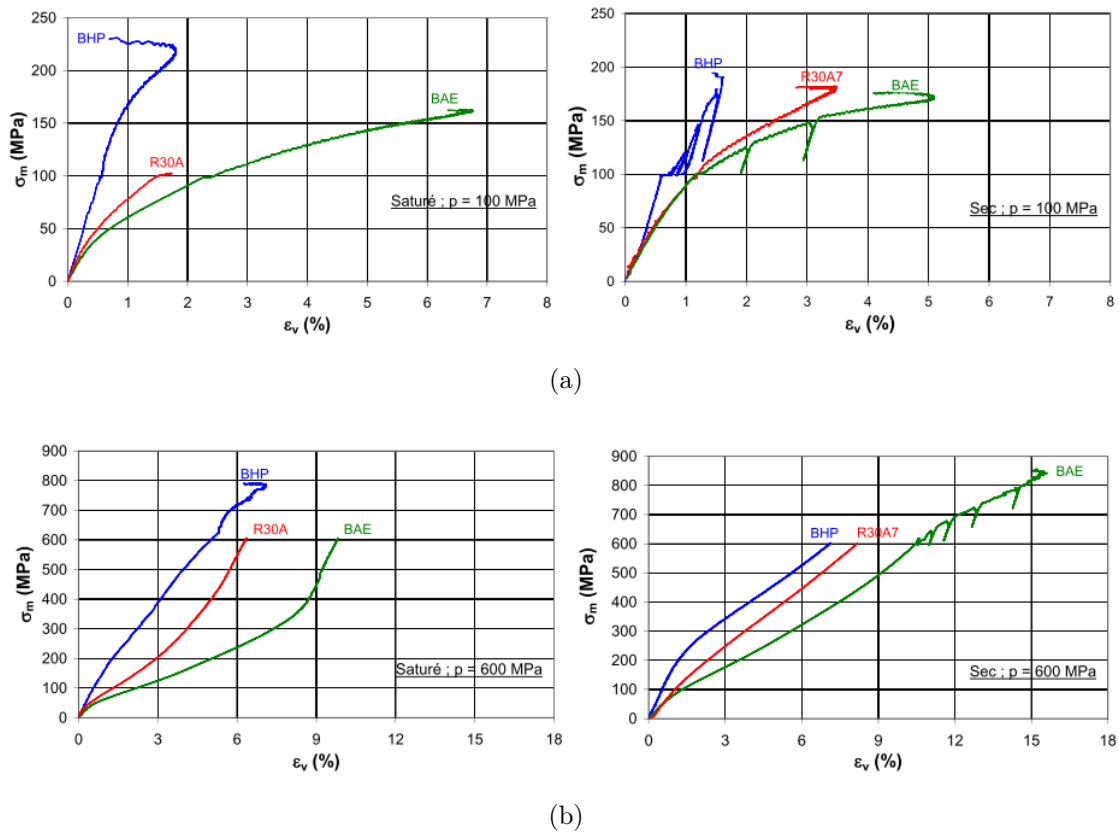
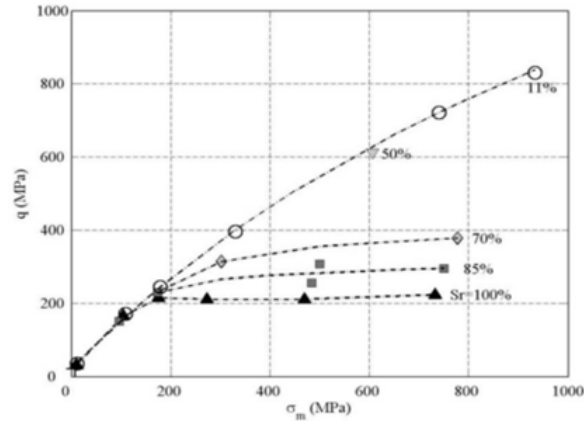


Figure 1.11: Results of triaxial tests on O, LP and HP concretes at the (left) saturated and (right) dried states. Mean stress vs. volumetric strain under: (a) 100 MPa (b) 600 MPa of confinement, [Zingg, 2013]

At low confinement pressure, a slight difference in the volumetric behavior of the three concrete types for different states is observed. Since the HPC matrix is the

most resistant, its tangent modulus decreases less rapidly than the OC and the LPC concretes for both dry and saturated samples, (Figure 1.11(a)). Whereas, at high confinement pressure, a relative difference (about 27%, 21% and 7%) between the volumetric strains of dry and saturated LPC, OC and HPC samples at a mean stress of 600 MPa can be noted, (Figure 1.11(b)). For this stress level, the volumetric strain becomes significant in comparison with the initial air volume of the sample. Concrete samples that had also lost their cohesion behave like an un-drained saturated granular material. Thus, the pore pressure developing within the material rises and exerts a significant impact on the measured stress.

In addition, (Figure 1.12) shows the limits state evolution of the three concrete types for different saturation ratios on a wide range of confining pressure.



(a)

The overall behavior of the three types of concrete is quite similar. At low confinement level, it was observed that there is a slight dependency of the saturation ratio on the concrete behavior where curves of both dry and saturated concrete coincide. In contrast, at high mean stresses, the shear strength of saturated samples becomes limited to a certain maximum value independently of the confining pressure. In other words, the curves of the limit states of saturated samples exhibit a plateau whereas they keep increasing for the dried concretes. This behavior is due to the presence of free water into saturated concrete which tends to limit its deviatoric stress.

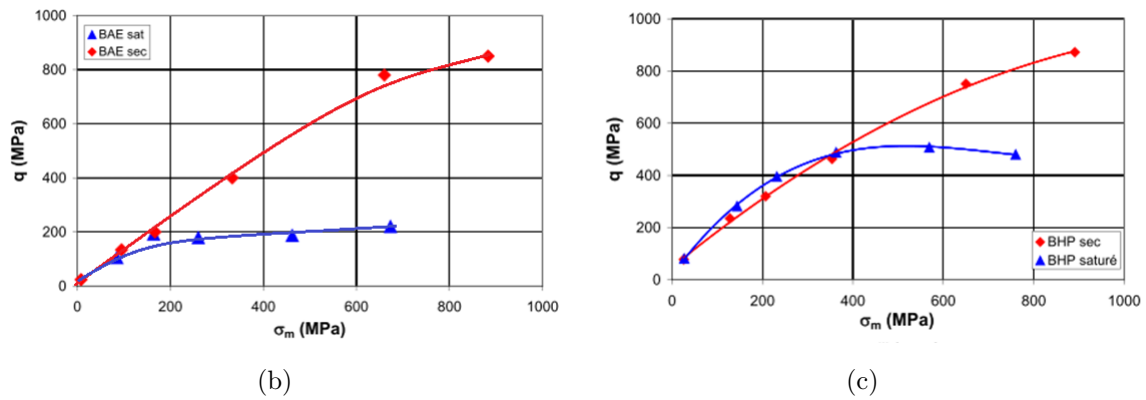


Figure 1.12: Stress limits states. Deviatoric stress vs. mean stress: (a) Ordinary (b) Low performance (c) High performance concretes, [Zingg et al., 2016]

1.3.3 Static quasi-oedometric test: effect of saturation ratio

Static quasi-oedometric compression (QOC) test allows testing the mechanical response of the material under a quasi-uniaxial deformation loading path while applying a passive confinement. During this test, a cylindrical specimen, tightly enclosed in a confinement vessel, is axially compressed by means of high strength compression plugs as shown in (Figure 1.13), [Burlion et al., 1998].

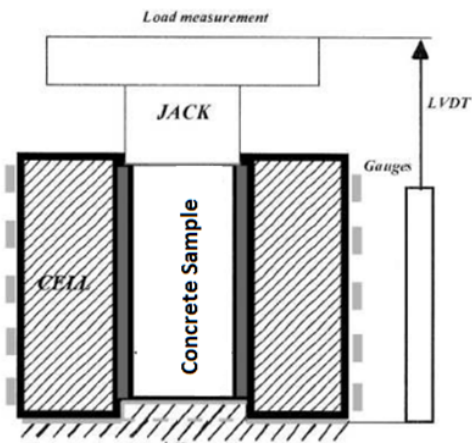


Figure 1.13: Concrete specimen jacketed by the steel confinement cell during quasi-oedometric confined test, [Burlion et al., 1998]

This kind of experiment was also performed by [Gabet, 2006] and [Vu, 2007]. Recently oedometric test was conducted by [Forquin et al., 2013] on an ordinary con-

crete by considering 4 levels of saturation ratio: dry, 60%, 80% and full saturated concrete. Figure 1.14: left, shows that the compaction process is more pronounced when the saturation ratio is low. For a full saturated sample, the mean stress curve is stiffer than for other concretes. A high level of volumetric deformation is reached for dry concrete since pores are free compared to those filled with water in the saturated samples. In addition results presented in (Figure 1.14: right) lead to the same conclusion drawn before. The deviatoric strength is continuously increasing with the increase of pressure in dry concrete whereas it is almost constant for full saturated one. The deviatoric stress exhibits a plateau at 100 MPa under a high hydrostatic pressure reaching 800 MPa. However, in the case of intermediate saturation ratio, moderate deviatoric stress levels are noted.

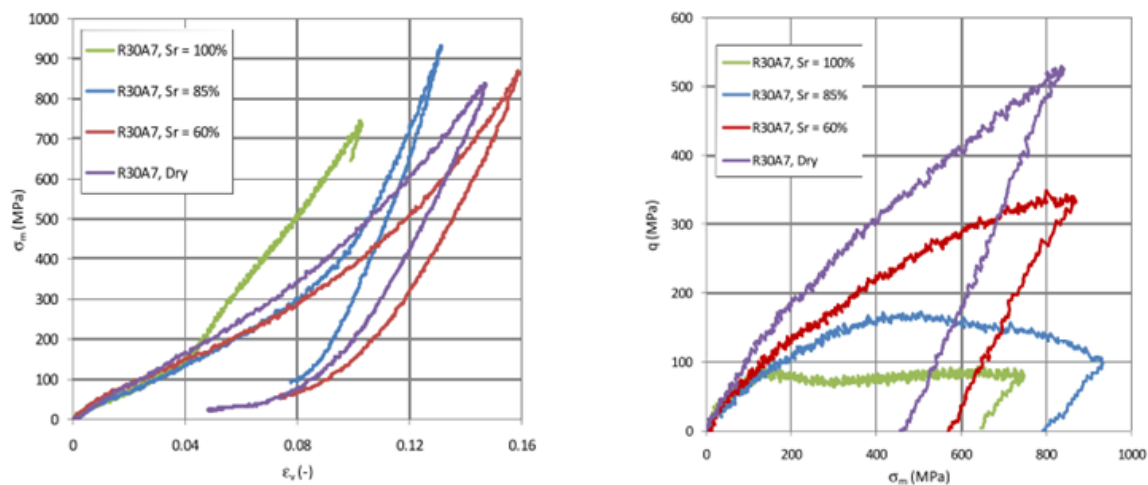


Figure 1.14: Quasi-oedometric tests on ordinary concrete with different saturation ratio: (left) mean stress vs. volumetric strain (right) deviatoric stress vs. mean stress, [Forquin et al., 2013]

Similarly, quasi-oedometric compression tests on high strength concrete (HS) were conducted by [Piotrowska and Forquin, 2014] where the volumetric and deviatoric behavior are displayed in (Figure 1.15). The presence of free water at the compaction stage induces a high pore pressure developing in the material, this effect is supposed to limit the concrete shear strength and increase its volumetric stiffness in the case of saturated samples. One can conclude from these results that whatever the constituent of concrete samples, the presence of water in pores has a big influence on concrete behavior under the quasi oedometric compression test.

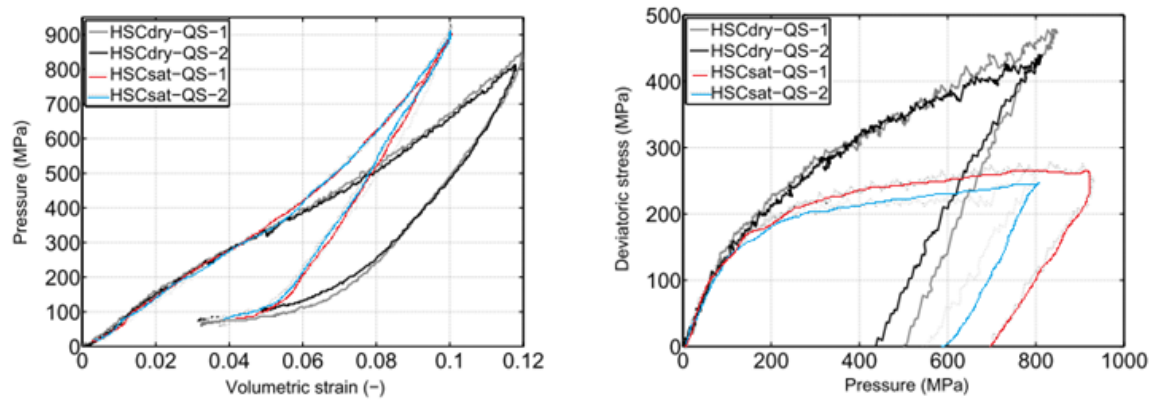


Figure 1.15: Quasi-oedometric tests on high performance concrete with different saturation ratio: (left) mean stress vs. volumetric strain (right) deviatoric stress vs. mean stress, [Piotrowska and Forquin, 2014]

1.3.4 Dynamic behavior of concrete

The purpose of the dynamic tests is to answer two main questions, [Bischoff and Perry, 1991], [Bischoff and Perry, 1995]. The first one concerns the sensitivity of concrete behavior to strain rates and the second one, which is the more important in this study, concerns the role of free water on the dynamic behavior of concrete. In what will follow, a campaign of dynamic quasi-oedometric compression, spalling and shear tests on different types of concrete will be presented.

1.3.4.1 Dynamic quasi-oedometric test: effect of matrix porosity

Concrete compressive strength is investigated under dynamic compression condition using the Split Hopkinson Pressure Bar (SPHB) technique pioneered by [Kolsky, 1949]. After being compressed using a high-strength steel cylindrical plug, the specimen is sandwiched between two input and output bars as illustrated in (Figure 1.16). To emphasize the influence of the initial matrix porosity and the water presence on the dynamic compressive strength of concrete, tests on ordinary and high performance concretes were performed by [Piotrowska and Forquin, 2014].

While comparing the volumetric behavior of both concretes (Figure 1.17), it was clearly shown that concrete composition and water presence affect its behavior. For both states (dry or saturated), the HP concrete is stiffer than the ordinary one leading to a lower volumetric strain. In addition, the volumetric strain for dry OC and HS concretes is more pronounced than the saturated specimens.

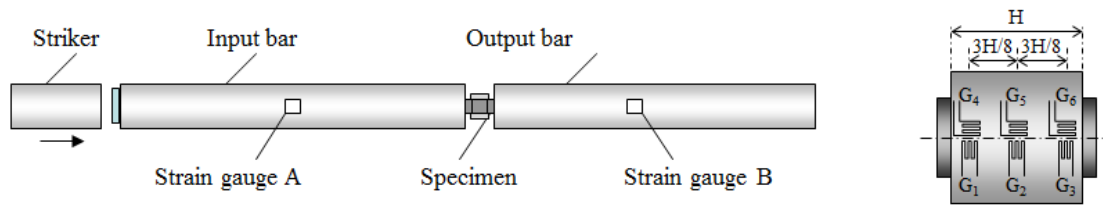


Figure 1.16: Set up of a quasi-oedometric test using the SHPB technique, [Forquina et al., 2008]

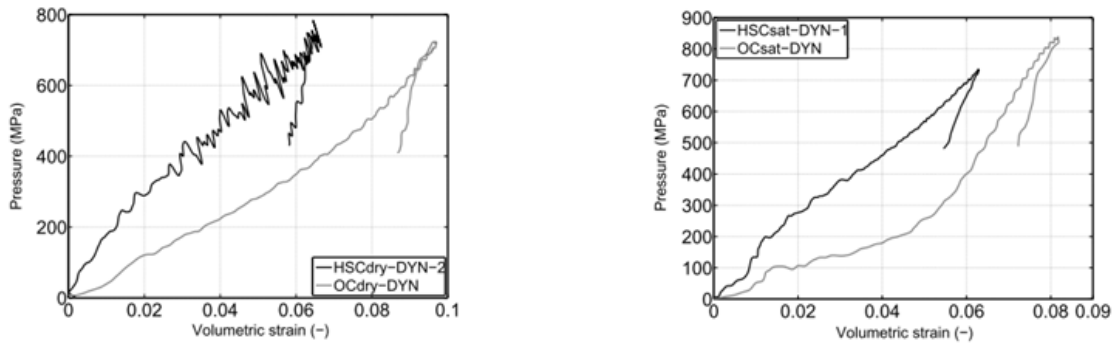


Figure 1.17: Dynamic quasi-oedometric test on ordinary and high performance concretes. Mean stress vs. volumetric strain: (left) dry (right) saturated states, [Piotrowska and Forquin, 2014]

Regarding the shear strength, it is clear that for the dry states, the ordinary and high performance concrete are not affected by their compositions. Meanwhile, a high limitation of shear strength occurred for saturated samples, (Figure 1.18).

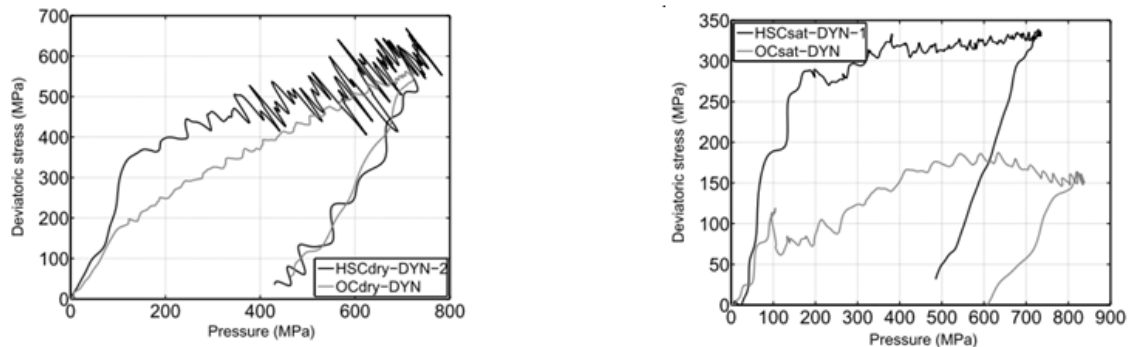


Figure 1.18: Dynamic quasi-oedometric test on ordinary and high performance concrete. Deviatoric stress vs. mean stress: (left) dry (right) saturated states, [Piotrowska and Forquin, 2014]

Coherent results are found when a series of dynamic quasi-oedometric tests with three impact velocities are performed on the micro-concrete (MB50) samples by [Safa et al., 2010]. The strain rate is ranging between 93 and 147 (1/s). The volumetric and deviatoric behavior for concrete sample at the dry and saturated states are shown in (Figure 1.19). These differences are directly linked to the presence of free water in concrete pores. In particular, for a given pressure, the level of compaction is clearly greater for dried specimens. Moreover, above 200 MPa of pressure, the evolution of the shear strength is quasi linear in the case of dried specimens and almost constant in that of saturated ones.

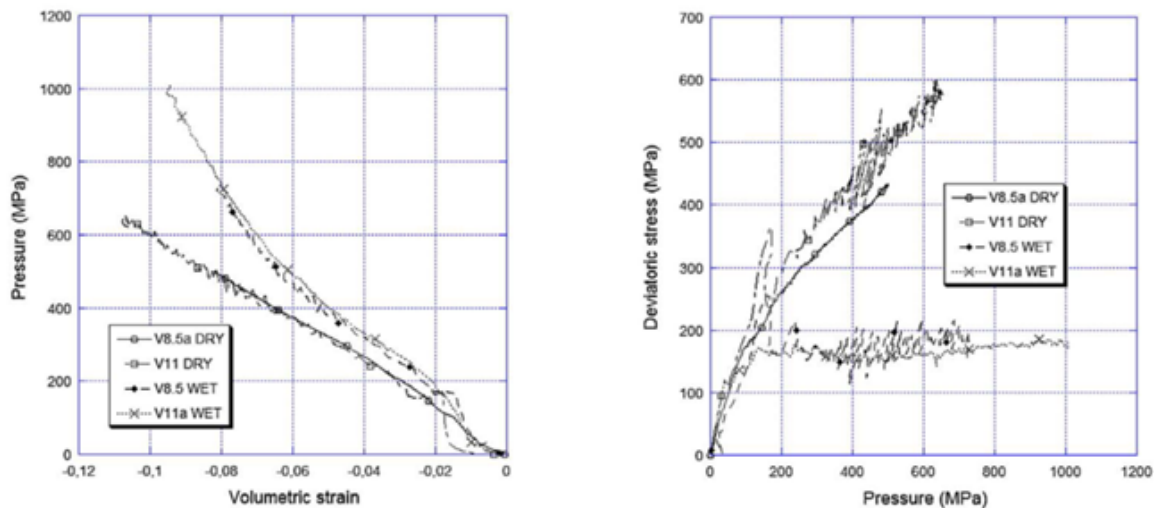


Figure 1.19: Dynamic quasi-oedometric test on the MB50 concrete at the dry and saturated states: (left) mean stress vs. volumetric strain (right) deviatoric stress vs. mean stress, [Safa et al., 2010]

1.3.4.2 Static and dynamic shear test: effect of free water

The shear behavior of concrete has been deeply investigated during the last three decades. Many different technics have been developed to study the fracture under mode II. One of this technic is the punch through shear test known as the PTS test which was introduced by [Watkins, 1983]. This method has been applied to characterize the stress intensity factor in mode II for different types of rock and concrete respectively, [Backers, 2004], [Montenegro and Carol, 2007]. These authors have performed the PTS test by applying an active confinement (hydrostatic pressure) on samples as a first state, then an axial load is added to create the shearing state. Both

experiments revealed a sharp increase of shear strength and fracture energy with the confining pressure as stated by the authors.

Recently, the shear strength of a reference dry and saturated concrete over a wide range of strain rate has been investigated by [Forquin, 2011] using a passive confinement. These tests are performed using a high speed hydraulic press and the Split Hopkinson Pressure Bar technique. Figure 1.20 shows that free water has a slight influence on concrete shear strength for a given strain rate (due to low confinement pressure). In the same way the increase of strain rate induces a small increase of concrete strength for both concrete states, [Forquin and Sallier, 2013]

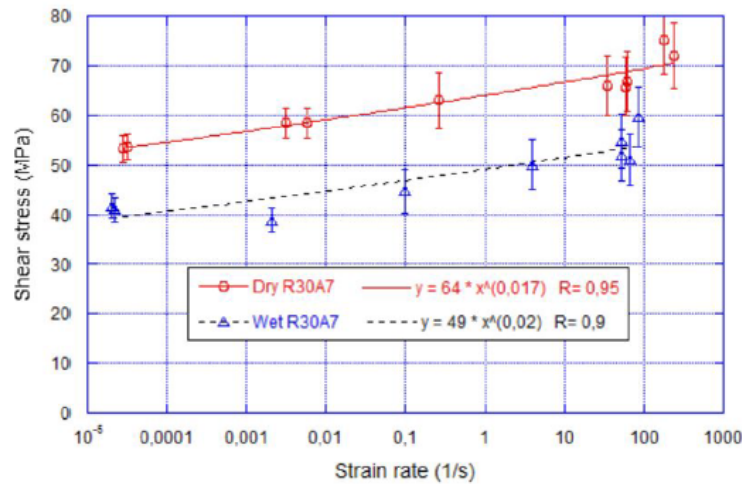


Figure 1.20: Quasi-static and dynamic PTS tests on dry and saturated ordinary concrete: shear strength vs. strain rate, [Forquin, 2011]

1.3.4.3 Dynamic tensile test: effect of saturation ratio

Concrete tensile strength is highly influenced by the strain rate as stated by many authors [Malvar and Ross, 1998], [Klepaczko and Brara, 2001], [Schuler et al., 2006], [Ozbolt et al., 2013], [Ozbolt et al., 2014] while the water presence effect has been recently investigated. To reach this purpose, tests at low, intermediate and high strain rate have been conducted on dry and saturated ordinary concrete, [Erzar and Forquin, 2010]. An experimental device based on the spalling technic is used, (Figure 1.21). The input bar is hit from one side by a striker where the concrete specimen is placed on the outer bar side. This configuration can create a tension wave into the concrete.

Experimental results on the ordinary and micro concrete are gathered in (Figure 1.22), a slight increase of tensile strength is recorded at low and intermediate

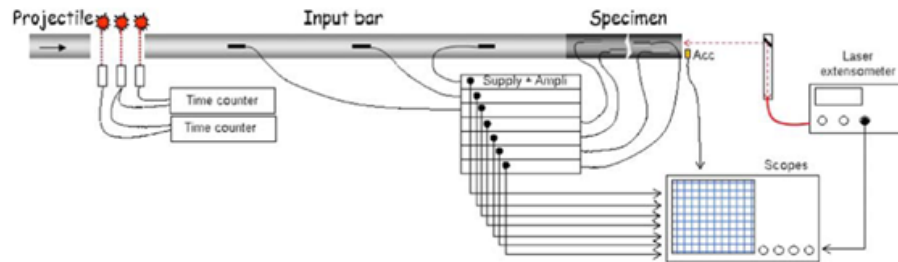


Figure 1.21: Spalling test device and instrumentation: projectile, input bar, specimen and strain gages, [Erzar, 2010]

strain rate with a very small influence of saturation ratio. However, at high strain rate, a surge in concrete tensile strength during tests is noticed by the authors while comparing it to the static test (2-3 times higher). The effect of free water is more pronounced: tensile strength increases from 7-11 MPa for dry concrete to 10-14 MPa for saturated one as illustrated. Same results on MB50 were reported by [Forquin and Erzar, 2010].

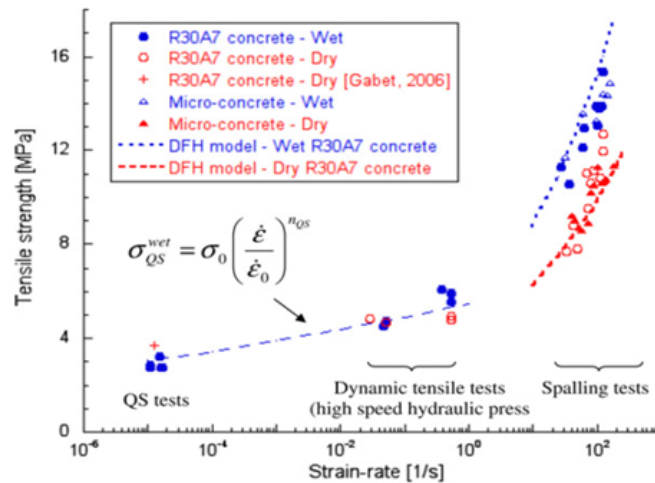


Figure 1.22: Quasi-static and dynamic tensile tests: tensile strength vs. strain rate for both dry and saturated ordinary and MB50 concretes, [Erzar and Forquin, 2011a]

1.3.5 Conclusion

Table 1.1 summarizes all the tests that have been shown in the literature review where the effects of concrete properties on many types of tests are illustrated.

Authors	Type of test	Material	Stress	S_r %	W/C	ϕ_0	$\dot{\epsilon}$
Vu, 2007	SC	OC	σ_c	NI	HI	-	-
Zingg, 2013	SC	HPC	σ_c	NI	-	-	-
Vu, 2007	TXT	OC	σ_m	HI	HI	HI	-
Vu, 2007	TXT	OC	q	HI	NI	NI	-
Zingg, 2013	TXT	OC, LP, HPC	σ_m	HI	-	HI	-
Zingg, 2013	TXT	OC, LP, HPC	q	HI	-	NI	-
Forquin, 2013	S-QOC	OC	σ_m	HI	-	-	-
Forquin, 2013	S-QOC	OC	q	HI	-	-	-
Piotrowska, 2014	S-QOC	HP	σ_m	HI	-	-	-
Piotrowska, 2014	S-QOC	HP	q	HI	-	-	-
Piotrowska, 2014	D-QOC	HP	σ_m	HI	-	HI	-
Piotrowska, 2014	D-QOC	OC, HPC	q	HI	-	NI	-
Safa, 2010	D-QOC	MB50	σ_m	HI	-	-	-
Safa, 2010	D-QOC	MB50	q	HI	-	-	-
Erzar, 2011	D-S	OC	σ_s	SI	-	-	SI
Erzar, 2011	D-T	OC	σ_t	HI	-	-	HI

Table 1.1: Summary of different tests available in the literature showing the influence of saturation ratio (S_r), water over cement ratio (W/C), initial porosity (ϕ_0) and strain rate ($\dot{\epsilon}$) where (SC) simple compression, (TXT) triaxial, (S-QOC and D-QOC) static or dynamic quasi oedometric compression, (D-S and D-T) dynamic shear or tensile tests. O, LP and HP: ordinary, low and high performance concretes. σ_c , σ_m , σ_s , σ_t and q are the: compressive, mean, shear, tensile and deviatoric strengths. NI, SI and HI means: no, slight and high influence

First, it was shown that there is no effect of the saturation ratio on the unconfined compressive strength of concrete. Whereas the water over cement ratio has a considerable influence. This results reveal that concrete compressive strength is linked to the concrete composition and not to the its saturation itself.

Second, triaxial tests on concrete have enlighten on many points such as: when com-

paring the volumetric behavior of the three types of concretes, the saturation ratio and the initial porosity have both a significant effects. However, the effect of the initial porosity vanishes while the effect of saturation ratio persist on the deviatoric behavior of these concretes.

Third and in the same manner, the effect of saturation ratio on concrete volumetric and deviatoric behavior is very high when tested under static and dynamic QOC conditions. In addition, a high versus non influence of the concrete initial matrix porosity on its volumetric and deviatoric behavior were consecutively illustrated. At the end, a slight versus high influence of the saturation ratio and strain rates on concrete behavior under dynamic shear and tensile tests were observed. All these tests reveal that on the one hand, the role of water is preponderant into concrete when subjected to high confinement under static or dynamic loading and on the other hand, it is more pronounced than the other concrete properties.

1.4 Modeling of concrete under impact: effect of free water

Concrete structures can be submitted to impact solicitation during which a wide range of loading are covered (hydrostatic, triaxial, dynamic tension, etc.). Besides, massive concrete structures keep a saturation ratio strongly depth dependent almost their life time (from a quasi-saturated state into the core to an almost dry state near its faces), [Baroghel Bouny et al., 1999]. Thus, the response of these structures under impacts is highly influenced by the state of water saturation into the material. Since it is hard to perform such kind of experiments permanently in normal condition (equipment, cost etc.), many methods were created to model the behavior of concrete under such loading paths. Numerical modeling is an approach used to predict the exact behavior of materials where high stress zones with large material or geometric non-linearities and discontinuous phenomena could occur as explained by [Mellinger and Birkimer, 1966], [Hughes, 1984], [Li et al., 2005] [Erzar, 2010], [Daudeville and Malecot, 2011]. In what will follow, results of two numerical approaches (continuum and discrete element) aiming to predict the behavior of a massive water-saturated concrete slab are presented. The penetration tests have been conducted by CEA-Gramat which consist of launching an ogive-nosed steel projectile into a cylindrical unreinforced ordinary concrete block with different thickness (300 or 800 mm) and (800 mm) of diameter, [Pontiroli et al., 2010].

1.4.1 Continuous model

This method is commonly used by engineers for the analysis and dimension of reinforced concrete structures. One of the issue while modeling impact test is the need to reproduce cracking and fragmentation process during test simulations. To achieve this purpose, many approaches were proposed and implemented. [Mazars, 1984] used the variable of damage varying from 0 to 1 to represent an intact or broken material. However, in the case of strong discontinuities, such as cracking or fragmentation, other authors have introduced an erosion criterion which consists in eliminating each element that has reached a threshold of plastic deformation, [Schuler, 2007]. In order to reproduce concrete behavior under several loading paths (e.g: static, dynamic and impact), a continuum model called PRM (Pontiroli-Rouquand-Mazars) has been developed. This model includes two scalar damage variables that give respectively the loss of stiffness under tensile loading and the loss of stiffness under compressive loading ([Pontiroli et al., 2010], [Pontiroli et al., 2015]). The model uses the effective stress concept and the poro-mechanical approaches to take into account the saturation ratio (e.g: water into pores), [Coussy, 1995], [Rouquand, 2002], [Vu, 2013].

Recently, [Pontiroli et al., 2015] has performed numerical simulations on Abaqus for the impact test conducted at the CEA-Gramat) where a coupled plasticity–damage model (PRM-KST model) was implemented. The KST (Krieg–Swenson–Taylor) plasticity model provides a description of the hydrostatic and deviatoric behavior under high confining pressures, [Erzar and Forquin, 2011c], [Erzar and Forquin, 2011b]. First the model parameters was calibrated by means of numerical simulations which have been carried out on the GIGA triaxial experiments conducted on dried and saturated concrete as stated by the author, (Figure 1.23). The results shows an overall good agreement between experimental and numerical response. However, it was observed that the model overestimate the concrete volumetric behavior at the saturated state.

Second, the model was validated by performing numerical simulations to reproduce the axial deceleration of the penetrator launched at an initial velocity of 350 m/s over a saturated concrete block of 800 mm in thickness, (Figure 1.24). A good correspondence between the simulation results and experimental data is observed and reveals that concrete slab conserves a very wet state in its core.

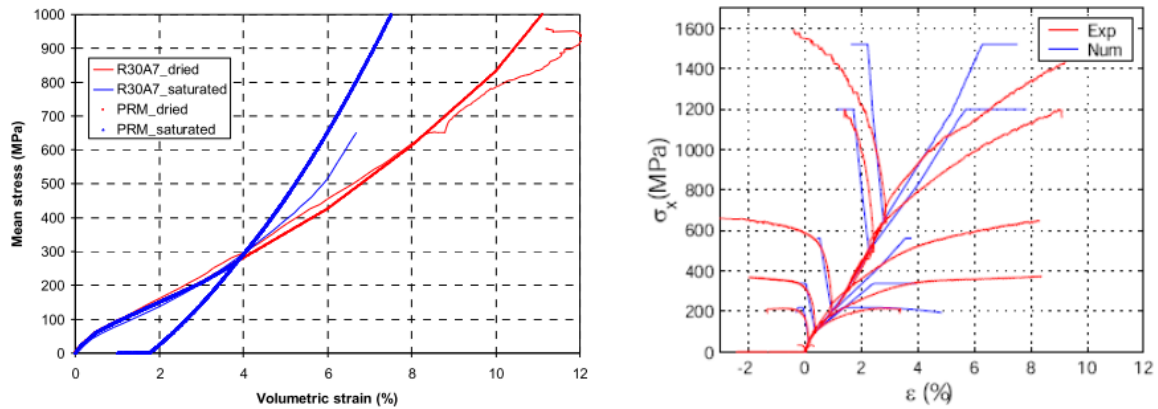


Figure 1.23: Experimental and numerical (FEM) comparison: (left) hydrostatic results on saturated concrete (right) triaxial results on dried concrete, [Pontioli et al., 2015]

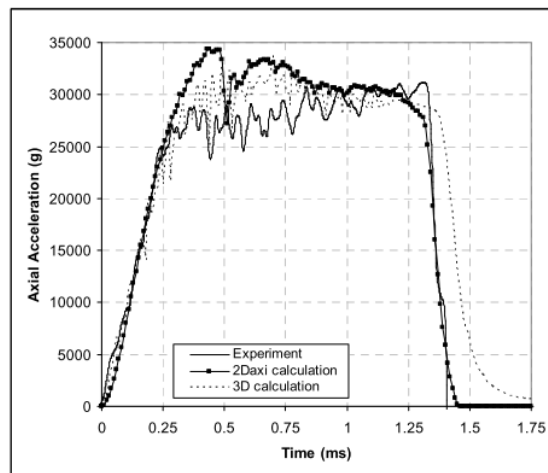


Figure 1.24: Experimental and numerical (FEM) comparison of 800 mm thick target with impact velocity 347 m/s: axial deceleration vs. time, [Pontioli et al., 2015]

1.4.2 Discrete model

To take into account the discontinuities linked to the macro-cracks in continuous method requires important developments. To deviate from these difficulties, a new numerical methods called the discrete elements method DEM has been developed in which the hypothesis of continuity in the medium is discarded. The medium is represented by a set of particles which have simple geometric shape treated independently one from another as solid or deformable bodies. The field of motion is no longer continuous so that it is defined by a finite number of spheres representing the cen-

ter of all particles, [Cundall and Strack, 1979], [Luding, 2008]. [Cundall and Strack, 1979]. In addition, discrete methods is capable to reproduce complex mechanical behaviors from a reduced number of parameters, (e.g: non-linear strain-strain response, fragile-ductile transition, and non-linear resistance threshold). This is accomplished through simple local interaction laws between DE's with failure criteria such as the Mohr-Coulomb criterion, or a tensile breaking threshold. From quasi-static to impact tests, the DEM model showed a high capability to reproduce concrete behavior. Geo-materials (e.g: concrete, soil and rock) behavior haven been also simulated using DEM model, [Hentz et al., 2004] [Donzé et al., 2009]. Saturated and un-saturated concrete behavior under high confining pressure are studied by, [Tran et al., 2011] [Tran et al., 2012]. The high computational cost in the case of impact simulation at the structural scale has imposed the use of coupling DEM/FEM model, [Rousseau, 2009], [Frangin, 2008]. Numerical structural analysis, based on the DEM approach, has been performed on a reinforced concrete slabs under rock fall or missile impact, [Hentz et al., 2005], [Shiu, 2008].

Recently, [Bennioui et al., 2016] has performed numerical simulations for the same impact test by using DE model on YADE (open source code) were strain rate effect on tension was implemented. The model was first calibrated on static compression and triaxial tests by taking into account the concrete saturation ratio as shown in, (Figure 1.25).

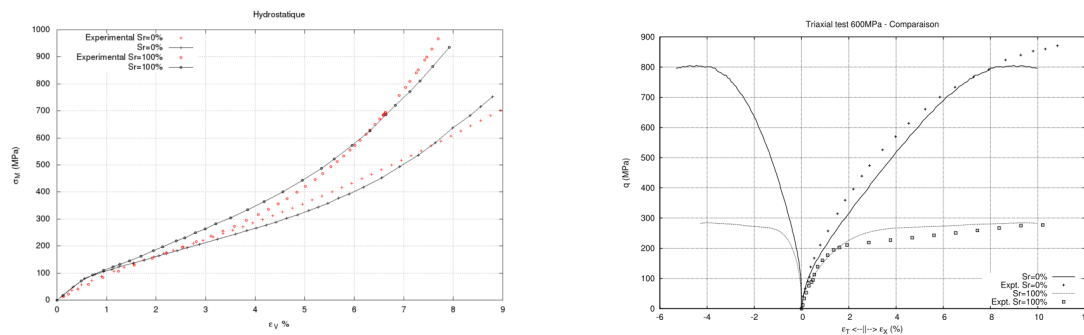


Figure 1.25: Experimental and numerical (DEM) comparison: (left) hydrostatic results (right) triaxial results on dried and saturated concretes, [Bennioui et al., 2016]

Furthermore, the model was validated by conducting numerical simulations on the same target thickness using the same projectile velocity described above. Figure 1.26 depicts the projectile deceleration profiles versus time for the 800 mm thick slab. It is clear that the numerical response does not totally corresponds to the experimental

one in which complex phenomena occur.

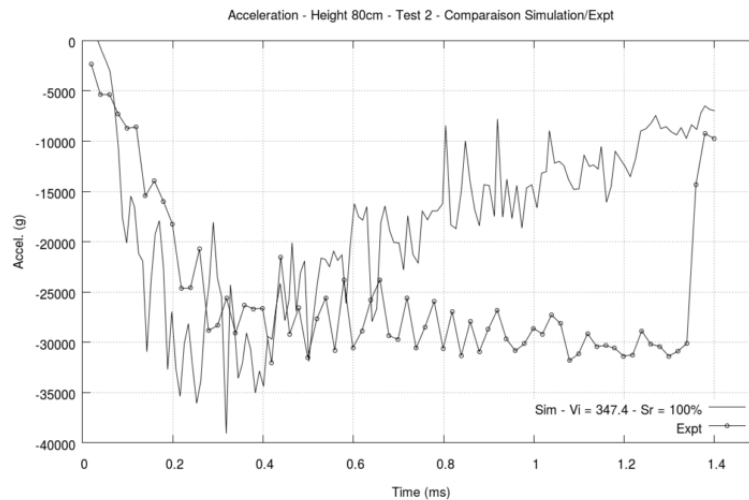


Figure 1.26: Experimental and numerical (DEM) comparison of 800 mm thick target with impact velocity 347 m/s : axial deceleration vs. time, [Bennioui et al., 2016]

1.5 Pore pressure measurement under low confinement pressure

Based on the results shown above, the strong influence of concrete state (dry or wet) on its mechanical behavior becomes evident, whether under static or dynamic compression or tension loads. Concrete volumetric and deviatoric behavior under high confinement are completely different for dry or saturated concrete. Thus, measuring the pore pressure of concrete becomes a need at high confinement level. In what will follow, results conducted by many researchers in order to quantify the pore pressure into geo-materials will be discussed.

1.5.1 Test on concrete

Triaxial test at low confinement pressure on cementitious material aiming to measure the pore pressure were performed under drained and un-drained conditions by [Poirier, 1996]. When the test is conducted under drained condition, the applied interstitial pore pressure is set to a constant value and the water can flow freely from the upper to the lower part. Whereas under undrained condition the volume of the water is

constant but the interstitial pore pressure varies without being able to run outside the press. For drained tests the pore pressure is applied by means of an injection pump where the pressure flow is controlled by means of a valve, (Figure 1.27). When the drainage is not possible the application of a deviatoric stress over a saturated compressible materials causes pore pressure variation within the porous structure of the material as stated by the author. [Poirier, 1996] noted also that this is not the application of the stress which causes directly the pressure variation but the variation of pore volume and that there was no pore volume measuring system during testing. It was found that the pore pressure increases when increasing the deviatoric stress (state of contraction), and conversely the pressure should decrease when the decreasing the deviatoric stress (state of dilatancy).

Results of triaxial tests on concrete with pore pressure measurement at different confinement pressure are reported in, (Figure 1.28). The measured pore pressure is directly affected by the amount of confinement applied, and thus it increases when the latter increases. Indeed, as the application of an important confinement tends to increase the resistance of concrete, the deviatoric stress increases by its turn inducing a small dilatancy and therefore a significant increase in pore pressure.

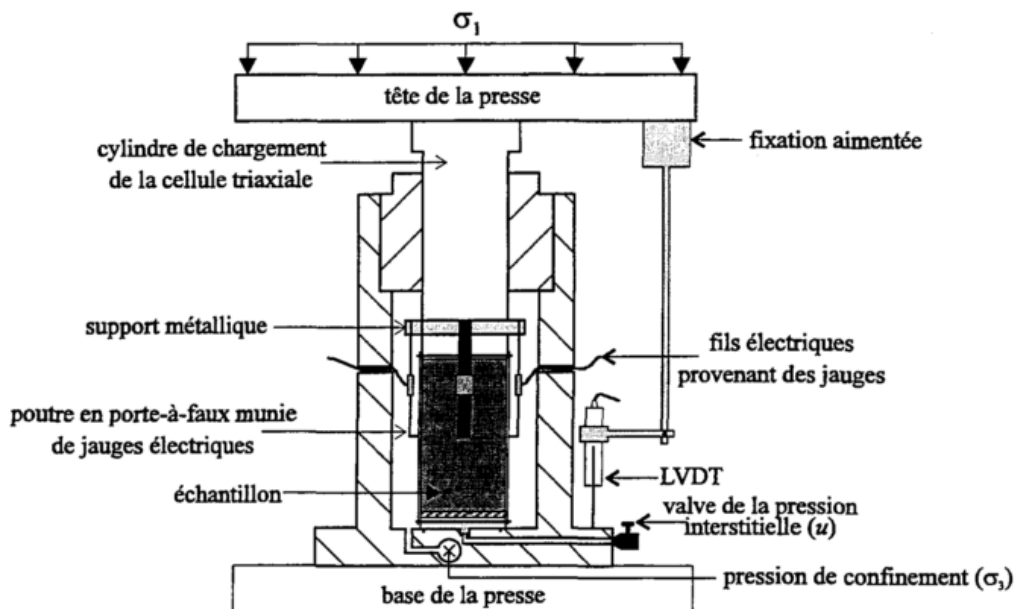


Figure 1.27: Assembly of the triaxial press, [Poirier, 1996]

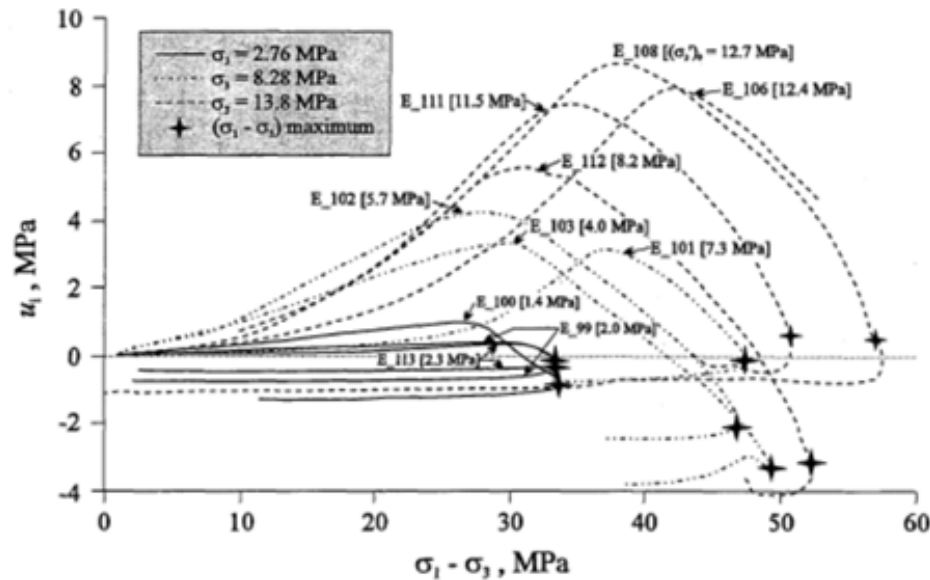


Figure 1.28: Concrete pore pressure evolution vs. deviatoric stress for different confinement pressure, [Poirier, 1996]

1.5.2 Test on rock

Triaxial tests under drained and un-drained condition at various confining pressure (7, 14, 28, 40 and 50 MPa) were performed on sandstone called Fontainebleau by [Sulem and Ouffroukh, 2005]. Triaxial tests were associated with pore pressure measurement, as described, since the lower base of the triaxial cell was equipped with a pore pressure transducer.

The authors notes that at low confinement pressure, the maximum stresses obtained in undrained tests on rock are more important than those obtained in drained conditions whereas this behavior reverses for high confining pressure, (Figure 1.29(a), 1.30(a)). Curves present very well the contractance-dilatancy transition in the volumetric behavior which is observed when the maximum load is reached. The volumetric strain levels achieved in the contractancy phase are lower in undrained conditions due to the pore pressure generated, (Figure 1.29(b), 1.30(b)).

Figure 1.31 shows the evolution of pore pressure in un-drained test on the rock. The authors emphasize that this evolution is strongly related to sandstone porosity, its drained compressibility and water compressibility. The maximum pore pressure reached coincides with the contractance-dilatancy transition point and they are proportional to the applied confining pressure. These pressures are then dissipated when

the dilating phase is reached due to crack opening. [Hild, 2015]

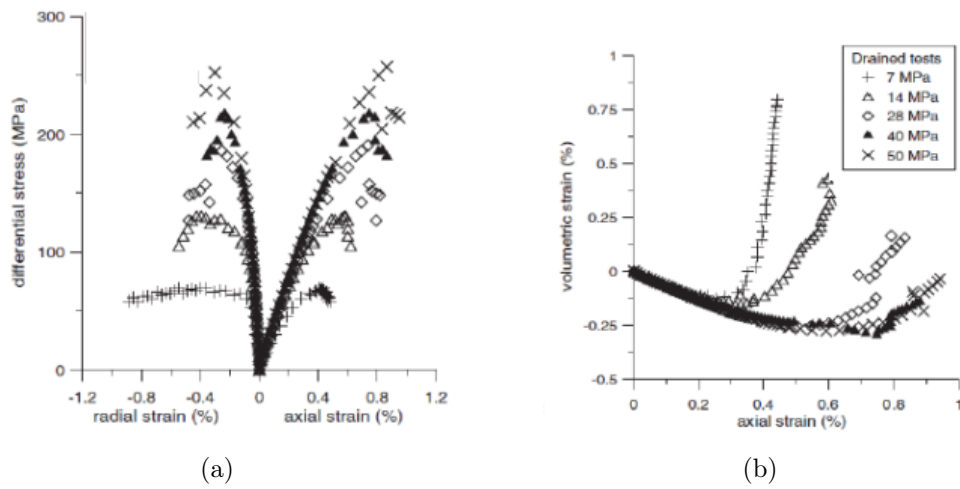


Figure 1.29: Drained tests on rock: (a) deviatoric stress vs. strains (b) volumetric strain vs. axial strain, [Sulem and Ouffroukh, 2005]

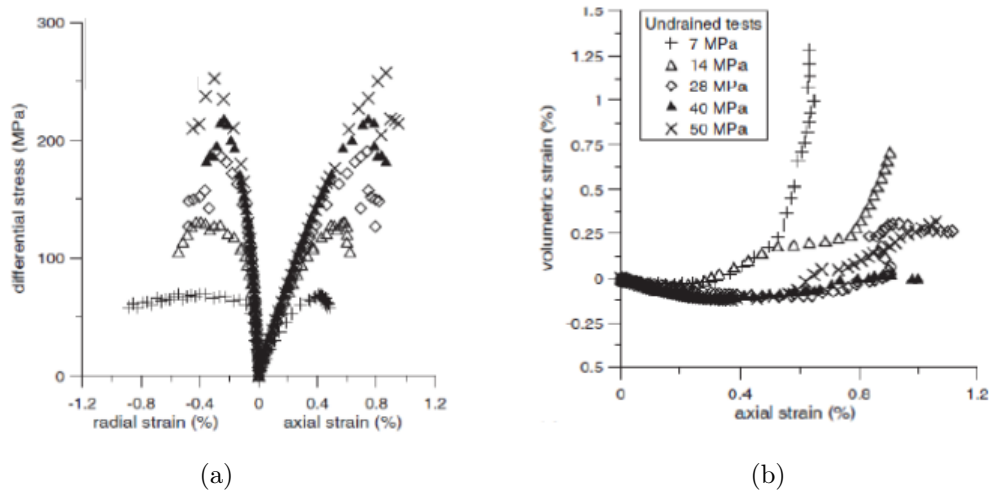


Figure 1.30: Undrained tests on rock: (a) deviatoric stress vs. strains (b) volumetric strain vs. axial strain, [Sulem and Ouffroukh, 2005]

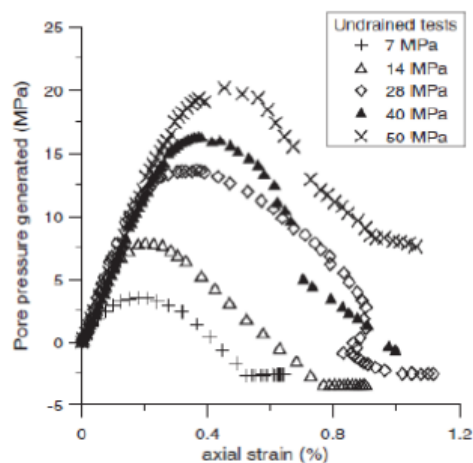


Figure 1.31: Undrained tests on rock: pore pressure vs. axial strain, [Sulem and Ouffroukh, 2005]

1.6 Poro-mechanic behavior of geo-materials

Poro-mechanics is defined as the study of porous materials whose mechanical behavior is significantly influenced by the pore fluid. A large range of porous-materials may be concerned by this definition such as rocks, concrete and soil. The poro-mechanics field is able to treat materials when subjected to many process (e.g: drying and shrinkage, heating and build-up of pore pressure, capillarity and cracking, etc..). In a related context, the poro-mechanical behavior of geo-materials has been widely investigated in the last decades, [Zimmerman et al., 1957], [Zimmerman, 2000], [Ghabezloo et al., 2012], [Ling et al., 2016], [Ingraham et al., 2017]. The notion of effective stress has emerged in continuum mechanics in order to describe a porous medium whose pore space might be filled by pressurized pore fluid. It was first introduced by [Terzaghi, 1936], who was working over consolidation of clayey soil layers and seemingly it was a product of intuitive calculations. [Biot, 1941] has extended this work by introducing the Biot's coefficient b , a dimensionless value which determines how much of pore pressure should be taken into account to become a relationship describing effective pressure (eq. 1.3) where: σ_{ij} : is the macroscopic stress tensor, σ'_{ij} : is the effective stress tensor, p_p : is the pore pressure and δ_{ij} : is the Kronecker symbol.

$$\sigma'_{ij} = \sigma_{ij} - \alpha p_p \delta_{ij} \quad (1.3)$$

[Hu and Skoczylas, 2017] recently studied the poro-mechanical properties evolu-

tion of sandstone issued from a depleted gas reservoir located in the east of France. In order to simulate the hydraulic and mechanical interaction during extraction, the sandstone samples with high initial porosity were tested under triaxial loading at 5, 10 and 20 MPa of confinement. Pore pressure fluid injection was possible by means of a specific pump. The test procedure as explained by the author permits to measure the Biot's coefficient in the axial and lateral directions. It is considered one of the most important parameter for coupling between mechanical variables, stress and strain, and the pore pressure. It has been shown that Biot's coefficient decreases in both direction but its greater in the lateral direction than the axial one. The reason is that under such loading, the number of the irreversible micro-cracks mostly oriented in axial direction increase while it decreases in the lateral direction.

In the same concept, [Nowakowski, 2012] investigates the evolution of the effective stress law for a sandstone rock under triaxial load. During the tests, several effective stresses were applied at a confining pressure ranging from 0 to 100 MPa. The pore pressure injection was controlled by means of a pump where four fluids types were used, two inert (kerosene and nitrogen) and two non-inert (distilled water and carbon dioxide). The Biot's b coefficient and the effective pressure are presented versus the differential strength limit, (Figure 1.32). The obtained results prove that on the one hand, the evolution of Biot's coefficient is linked to the type of the fluid and may be greater than unity. On the second hand, it is clear that whatever the pore fluid type, when the differential strength increases a regular growth of the effective pressure is observed.

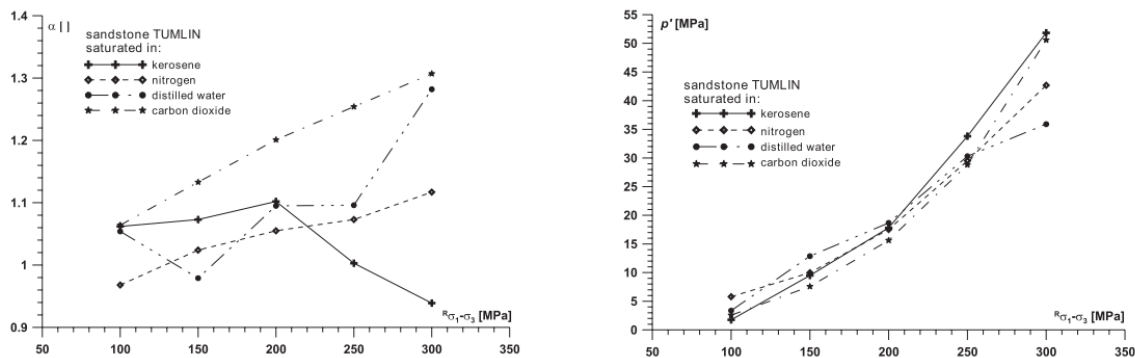


Figure 1.32: Triaxial tests on sandstone rock: (a) Biot's coefficient (b) pore pressure evolutions versus the differential stress, [Nowakowski, 2012]

1.7 Conclusion

The mechanical behavior of concrete is affected by several parameters such as: water/cement ratio, saturation ratio and initial matrix porosity. The water presence has a significant effect on the response of concrete subjected to static and dynamic loading as shown in the first part. The concrete unconfined compressive strength is influenced by the water/cement ratio since it controls the strength of the concrete matrix. However, the influence of the saturation ratio of concrete is mostly significant under high mean stress. On the one hand, it was observed that for concrete having important water content, the pressure volume relationship becomes stiffer than the one observed with a fully dried material. On the other hand, a limitation against linear increase of the shear strength with confining pressure is figured out for saturated and dry concrete respectively. The same trend of curves was observed when the varying the initial matrix porosity and saturation ratio changes. In addition, water presence into concrete has a high influence on its behavior under dynamic loading (e.g: tensile, shear and quasi-oedometric compression). All these results reveal that free water into concrete pores has a preponderant role for almost all types of solicitation. The second part of this chapter discussed two methods ailing to model concrete under impact loading. Numerical simulations issued from an FEM and DEM computational methods have shown a good capability to reproduce the experimental results. However, both approaches can be enhanced by taking into account the behavior of pore pressure under high confinement. The last part of this chapter was dedicated to present previous results of pore pressure measurements on concrete and rock under drained and undrained condition at very low confinement. It was shown that the water has a moderate role under low confinement but it plays a major role on the concrete volumetric and shear response under high confining pressures. However, the pore pressure shown in the previous studies was generated using a pump system linked to the specimen by means of pipes.

The aim of this study is perform interstitial pore pressure measurement tests on a very wet reference ordinary concrete. To do that, two configurations of pressure sensor will be displayed and a new water collecting cap concept will be used. Hydrostatic tests performed on wet concrete will be performed using the Giga press capable to generate very high confinement. A poro-mechanical approach based on the effective stress concept will be modeled in order to simulate the evolution of pore pressure and volumetric strain under high confinement.

Experimental procedure

2.1 Introduction

This chapter presents the experimental procedure followed during this study. The R30A7 reference concrete is selected, prepared and casted to be the material for which pore pressure measurement test will be performed. The behavior of this concrete has been largely investigated under triaxial test at high confinement in the 3SR laboratory, ([Gabet, 2006], [Vu, 2007], [Zingg, 2013]). An overview of the Giga and the schenck press, used to conduct experimental tests, will be shown. However, conducting interstitial pore pressure measurement on the Giga press is not obvious. Since the Giga press had not originally been designed for pore pressure measurements, some modifications should be done to the movable part as it will be discussed at the end.

2.2 Formulation and conservation of the studied concrete

It is essential to define the concrete material that will be used in this study before proceeding for the experiments. This selection is based on several aspects. Since this study is a part of larger project aiming to understand concrete behavior under triaxial test at high confining pressure, it is obvious to choose the same reference ordinary concrete (OC) called R30A7, deeply investigated as it was shown in (Chapter 1).

The formulation of the reference concrete R30A7 is based on the work carried out by [Vu, 2007]. The formulation, preparation and processing of samples in a proper way is very essential for a successful achievement of the tests. Indeed, the mechan-

ical behavior of the concrete should be reproducible on several tests resulting from different castings. For this, the formulation and preparation must be controlled with the aim of having a homogeneous concrete behavior at the macro scale. The R30A7 concrete has a compressive strength of 30 MPa at 28 days and a mean slump of 7 cm using Abrams cone. As a composite material, the fabricated concrete is made of a Portland cement type CEM I 52.5 N PM ES CP2 (Vicat), a good quality of rolled siliceous aggregates (98.7% silica) type BB 0.5/8 and a rolled siliceous sand (97.3%) type SILMIX BB 1800 μ_m/m . The maximum size of the aggregates must be chosen in the interest of homogeneity with respect to the size of the future test samples. For tests under high confinements such as those carried on the GIGA press, the imposed size of the specimens is 7 cm in diameter for 14 cm in height so that the maximum size of the aggregates is fixed at 8 mm. The granular skeleton must also have a homogeneous distribution in order to optimize its compactness. The concrete that we have been casted is then conserved in water for 5 months before being tested.

2.3 Specimen preparation

2.3.1 Concrete fabrication

The fabrication procedure follows the NF-P-18-404 norm, it is so important to cast samples in a proper way in order to guaranty a very good quality. Concrete is casted in a 13.5 liter parallelepiped mold, dry mixing last 60 seconds while mixing with water takes 120 seconds. The vibration is carried on a vibrating table during 30 second. Slump test are then made on the casted fresh concrete using the Abrams cone. After casting, concrete blocks are kept 24 hours protected from air by a plastic film. Samples are then conserved for 28 days in a saturated environment inside waterproof bags immersed in water to insulate concrete both physically and thermally during hydration process.

2.3.2 Coring and Surface machining

Once the conservation period inside the water ends (approx. 28 days) the preparation procedure begin by passing through three stages. The first one is the coring phase which is made directly on the casted concrete blocks to give the desired samples diameter and avoid any edge effects, (Figure. 2.1: left). Samples are then cut using a concrete saw under water to prevent overheating, this task correspond to the second

stage. The last stage consists in grinding concrete samples in order to correct the parallelism between the two sides, (Figure 2.1: middle). The parallelism defect of sample faces should be less than 0.1 mm to ensure a homogeneous distribution of the stress during triaxial tests. Finally, to guaranty the saturation of concrete, samples are immersed into water for more than five months before performing pore pressure measurement test, (Figure 2.1: right). In order to ensure that the concrete samples are well fabricated, two kinds of verification are performed. The first one is a physical where concrete porosity is measured. The second one is the mechanical verification where simple compression tests are performed on concrete samples.

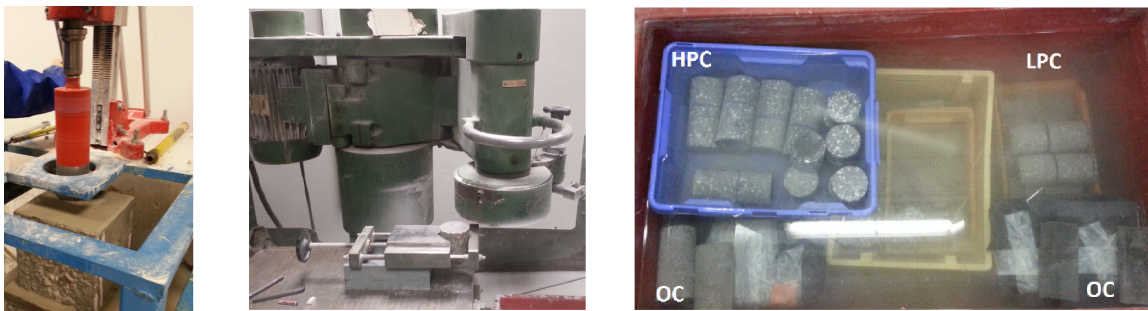


Figure 2.1: Preparation stages: (left) coring of concrete block and samples extraction (middle) concrete surface treatment (right) samples conservation into a saturated environment

2.3.3 Porosity measurement: pores accessible to water

Scope

In this study, only porosity accessible to water measurement is carried out to estimate the concrete sample porosity. This method consists in measuring the weight of sample at three states: full saturated state, totally immersed in water state (hydrostatic) and in its dry state. Some precautions are required to avoid samples swelling or disintegrating when they are immerse into water or oven-dried. The whole procedure is illustrated in (Figure 2.2).

Procedure

- 1) The first step consists in saturating concrete sample by water immersion in a vacuum of less than 800 Pa. Sample is then transferred under water to a bath

equipped with a basket totally immersed in water. The basket is suspended to a balance which permit to determine the saturated-submerged mass M_{sub} .

- 2) The second step consists in taking out the sample from immersion bath and drying its surface with a moist cloth. Care being taken to remove only surface water and to ensure that no fragments are lost. Its saturated-surface-dry mass M_{sat} is then weighed in air.
- 3) The third step involves drying the saturated sample in an oven at 50°C until its weight stabilization according to the criterion $\Delta_{m,2h}/m \leq 0.1$, where $\Delta_{m,2h}/m$ is the change in the relative weight over 2 hours. The mass of the dry sample is called M_{dry} .

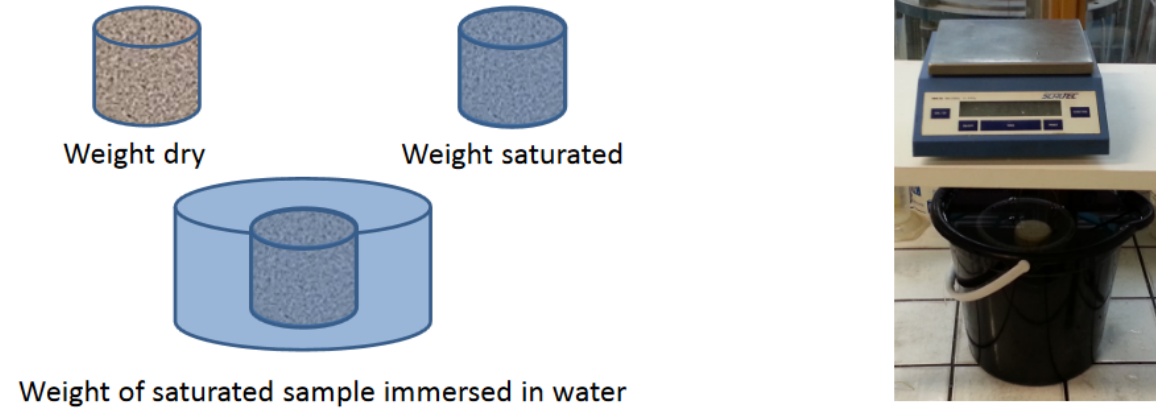


Figure 2.2: Porosity measurement: (left) dry, saturated and submerged sample masses (right) experimental set up used to measure concrete submerged mass

Formula

The porosity accessible to water η , (eq. 2.1), is defined as the ratio between the pore volume accessible to the free water and the apparent volume of the sample which can be related to the masses described above. The measurement is made on a cylindrical concrete sample of 7 cm in diameter and 5 cm in length. Table 2.1 depicts porosity accessible to water measurement results for the ordinary concrete. Values are in a good consistent with the literature, [Vu, 2007].

$$\eta = \frac{M_{sat} - M_{dry}}{M_{sat} - M_{sub}} \quad (2.1)$$

Sample	OC
M_{dry} (g)	486
M_{sat} (g)	514
M_{sub} (g)	273
η (%)	11.6

Table 2.1: Ordinary concrete sample mass for the three states: dry, saturated and submerged with porosity accessible to water estimation

2.4 Simple compression test

2.4.1 Schenck press presentation

To verify the strength of poured concretes, simple compression tests are performed on hardened concrete at 28 days. The Schenck press is used to achieve this purpose. This press has a servo-hydraulic jack with 1000 KN of capacity and a piston with a displacement rate lower than 20 mm/s controlled hydraulically, (Figure 2.3: left). All the tests are controlled in displacement which allows observing the softening behavior of the material during the post-peak behavior. To limit the effect of parallelism during the test, a plate equipped with joint is positioned between the piston and the upper face of the specimen.

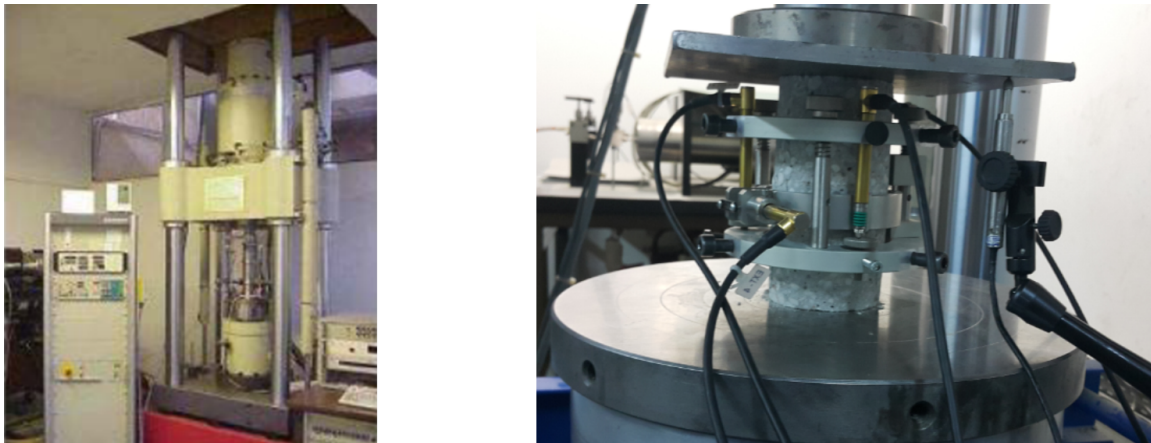


Figure 2.3: Schenck Press: (left) general view (right) instrumentation of a concrete specimen by using the circular steel collar

In order to measure the concrete deformation during the compression test we used a circular steel collar equipped with four LVDT, three of them in the axial position and one on is in the radial position as shown in (Figure 2.3: right). Since this method

gives only one information in the radial position, an additional radial gage is glued on the specimen at the same time.

2.4.2 Test results

Results of simple compression tests on the ordinary concrete is shown in (Figure 2.4) where the axial compressive stress is plotted versus the axial and radial strains. A maximum compressive strength of 34 MPa is reached during the test. This result is in a good agreement with previous studies, [Vu, 2007]. In addition, the average slump and initial porosity are well controlled (table 2.2) which means that concrete fabrication is well reproduced.

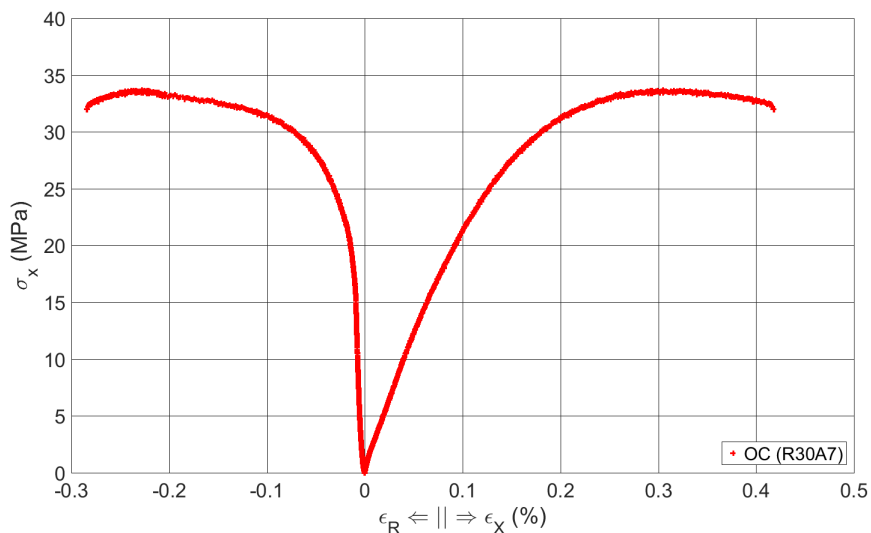


Figure 2.4: Results of the simple compression test on the ordinary concrete: axial stress vs. strains

Mechanical properties	OC
Compression strength at 28 day (MPa)	34
Porosity accessible to water	11.6
Average slumps (cm)	7
W/C ratio	0.64

Table 2.2: Mechanical properties of the ordinary concrete

2.5 Triaxial test set up

2.5.1 Device presentation

The machine used in order to perform the pore pressure measurement is called *GIGA* press [Thiot-ingénierie, 2004]. It is designed and constructed by THIOT engineering company with the financial support of the CEA and DGA in 2004. It is capable to generate a confining pressure up to 850 MPa and an axial stress reaching 2.3 GPa on a specimen with 7 cm in diameter, allowing to perform triaxial test at high confining pressure. The press is installed in the 3SR laboratory as illustrated in (Figure 2.5).



Figure 2.5: Overview of the triaxial press GIGA

Figure 2.6: left shows the main components of the Giga press, the confinement fluid called DOZ: di-2-ethylhexyl azelate, a non-volatile organic, inert and slightly-compressible liquid, is injected into the confinement cell through an upper opening. The fluid is then pressurized by means of a pressure multiplying jack till the desired confinement. The fluid is driven till the jack upper part under 25 MPa. The difference between piston lower and upper part sections is 40 allowing creating a confinement up to 1 GPa. The 13MN axial jack, engaged to generate the triaxial part, is located under the confining cell. The force is transmitted to the sample by a piston passing through the lower plug of the confinement cell. Figure 2.6: right describes in detail the inner part of the press. Samples made of concrete or rocks of 5 by 10.5 cm or

7 by 14 cm in diameter and length consecutively are sandwiched between two main caps made of Tungsten material.

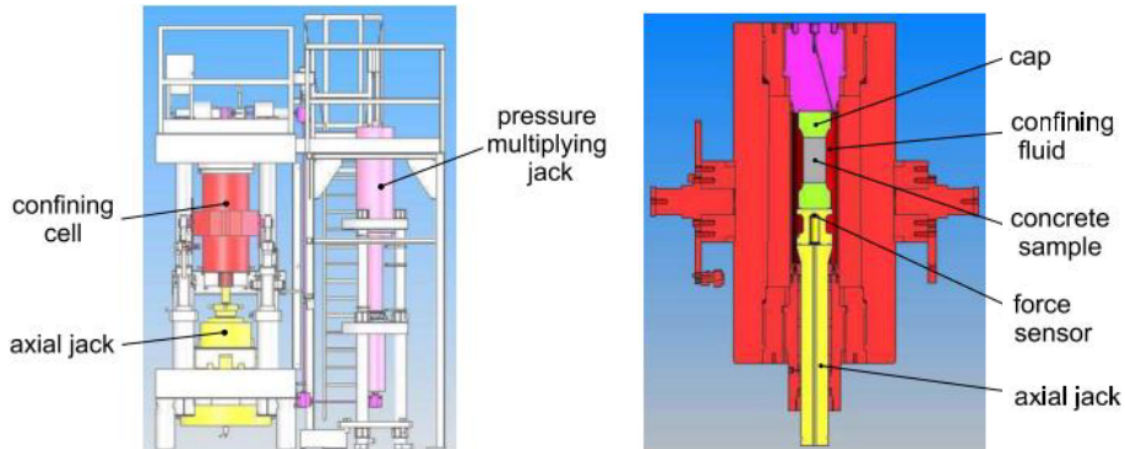


Figure 2.6: Schematic illustration of the triaxial press GIGA: (left) general scheme of the press (right): cross-sectional view of the confining cell

2.5.2 Loading paths

The press is designed to perform several types of tests from classical ones (e.g: uniaxial compression, hydrostatic at high confinement) or even more complicated tests such as oedometric, triaxial and extension. Specimens are loaded both hydrostatically and along their axis. The confining pressure and the axial jack displacement are controlled independently by means of two sensors which allows different loading paths as presented in (Figure 2.7).

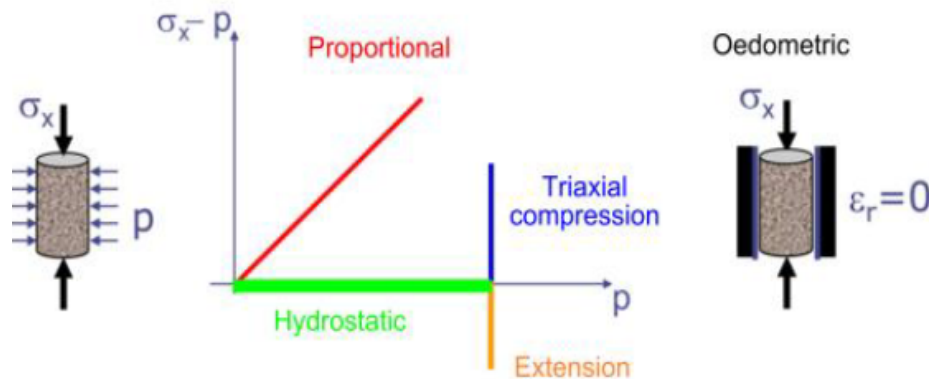


Figure 2.7: Available loading path of the triaxial press GIGA

The triaxial compressive loading is applied in two steps: the hydrostatic one consists in applying a confinement pressure all around the specimen at a constant stress rate of 1.67 MPa/s (maximum pressure rate) up to the desired value. Once the intended confinement has been reached, the specimen is loaded axially at a constant displacement rate of 20 $\mu\text{m/s}$ (e.g: a strain rate of approx. $10^{-4}/\text{s}$) while keeping the confinement pressure constant. The unloading phase proceeds in the reverse order.

2.6 GIGA press instrumentation

2.6.1 Introduction

To guaranty a good proceeding of test on the Giga press, two major sensors have been installed. The first one is a pressure sensor aiming to provide an exact value of the applied pressure and to keep it stable if necessary. The second one is a force sensor which permits to seek the correct axial force applied on the specimen. Both sensors are calibrated separately by the provider. Sample strains are provided by means of an LVDT: *Linear Variable Differential Transformer* or a gages assembly. These facilities can be implemented in the same time or independently to measure concrete strains during test.

2.6.2 Pressure measurement

The Giga press is equipped by a pressure sensor aiming to control the confinement pressure during experiments. It is installed in the inner part of the confinement cell and has an accuracy of 1% (e.g: 10 MPa for 1000 MPa). This sensor is calibrated, certified and replaced every year by the manufacturer. All corrections of force sensor, LVDT and gages signal are based on the pressure signal which remains accurate with the time.

2.6.3 Strain measurement

2.6.3.1 Concept

In order to quantify the volumetric strain of the concrete during interstitial pore pressure measurement under hydrostatic loading, only LVDT will be implemented. Basically strain gages can also be used by being glued on the sample, but since the concrete used in this study has a very wet lateral surface, fixing and conserving a gage

becomes a very complicated task. Two reasons can affect the LVDT measurement as reported by [Vu, 2007]. First, its position regarding the upper cap. In fact it was demonstrated by [Vu, 2007] that the optimal distance between the upper face of the principal cap and the LVDT support has to be set equal to 34 mm. The second reason is the sensitivity of the LVDT to the applied confining pressure. In many previous works on the Giga press, concrete length was maintained equal to 14 cm. In this case, the LVDT calibration test is made once a year or when the LVDT is damaged and has to be changed. Indeed, in this study, the length of the specimen is set equal to 8 cm as it will be shown in (sec. 2.7) and thus, the LVDT calibration test becomes essential.

2.6.3.2 LVDT calibration test

Normally, the LVDT is attached to the two principle caps by means of a cylindrical steel plug. When the confining pressure is applied, the LVDT deforms and measures the strain of the whole system (specimen, caps and support). This excessive strain is corrected by means of the LVDT calibration test. The concrete sample is substituted by a material with a high elastic capacity such as steel. A gage is glued on the sample to measure its axial strain and correct the one registered by the LVDT (Figure 2.8: left). In this study, the concrete specimen has a 8 cm in length which is lower than the normal length (14 cm) adopted in all the previous studies. To meet the new concrete dimensions, the 14 cm steel specimen is split into two sub-specimens of 8 cm and 6 cm, (Figure 2.8: right). The relation between the local u_x and the total u_{total} displacements measured by means of the gage and the LVDT respectively is given in (eq. 2.2a). The effect of the confining pressure u_p is then quantified and a the correction coefficient k_p is then calculated, (eq. 2.2b).

$$u_{LVDT} = u_{total} = u_x + u_p \quad (2.2a)$$

$$u_p = u_{LVDT} - u_x = p_c * k_p \quad (2.2b)$$

Result of the hydrostatic calibration test at 500 MPa of confinement on the 8 cm steel sample is shown in (Figure 2.9). The gage deformation is linear which means that the material remains in its elastic domain. The resultant coefficient k_p is equal to -0.0015 mm/MPa and it will be used to estimate the volumetric strain of the saturated samples during interstitial pore pressure measurement.

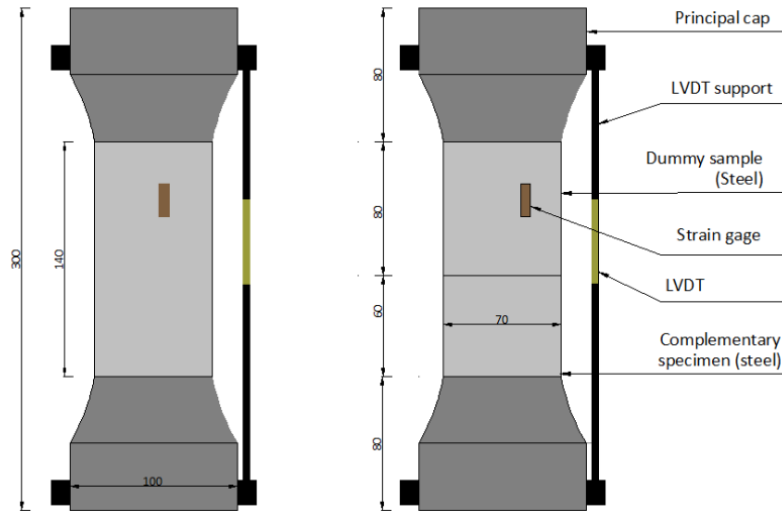


Figure 2.8: LVDT calibration test: (left) 14 cm (right) 8 cm specimen length

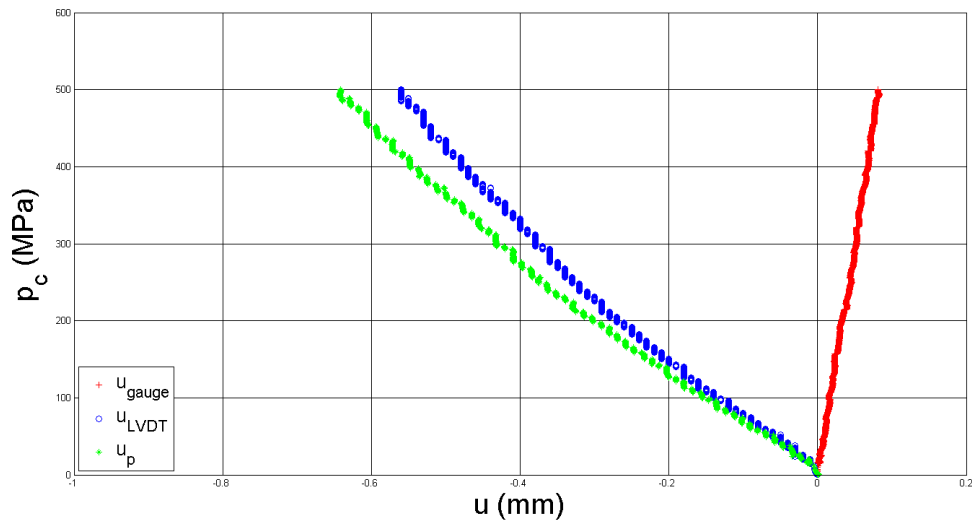


Figure 2.9: Calibration test result on a steel specimen of 8 cm in length: confinement pressure vs. gage and LVDT displacements

2.7 Water collect cap system

To better understand the effect of free water on the macroscopic behavior of concrete under extreme loading, it is particularly essential to measure the interstitial pore pressure into concrete. Till the present, all the tests on wet or saturated concretes performed on the Giga press are carried out under un-drained condition. In

our opinion this condition is satisfied since the free water inside pores can not be pressurized by a pressure higher than the confinement one. To conduct such a test, a water collecting cap already designed is used in this study.

2.7.1 Drainage cap conception

Normally, hydrostatic and triaxial tests on the Giga press are conducted on cylindrical specimen of 14 by 7 cm or 10.5 by 5 cm in length and diameter consecutively. Concrete specimen is sandwiched between two principal caps made of tungsten in order to have a final length of 30 cm as required, (Figure 2.10). The Giga press is not equipped by a system allowing the pore pressure measurement. In addition, the pore pressure can not be measured directly since the geometry and the specification of the movable part make impossible the implementation of a prefabricated sensor. The idea consists in creating a cavity to collect the water coming from the sample subjected to high confinement. This space aims at receiving a deformable sensor, capable to measure the interstitial pore pressure after being calibrated. Many precautions have to be taken into account in the new concept such as respecting the overall dimensions of the system and having a concrete sample with representative dimensions.



Figure 2.10: Principal caps dimensions and shapes adapted for both sample lengths and diameters: (a) 10.5 by 5 cm (b) 14 by 7 cm

2.7.1.1 Provisional concept

The provisional concept consists in conserving the main concrete dimensions and to create a sort of a cavity/holes system into the lower cap at its contact surface with the sample, (Figure 2.11).

This idea permits to conserve the initial concrete dimensions in particular its length. Several technical reasons have led to dispense this concept (high price of the

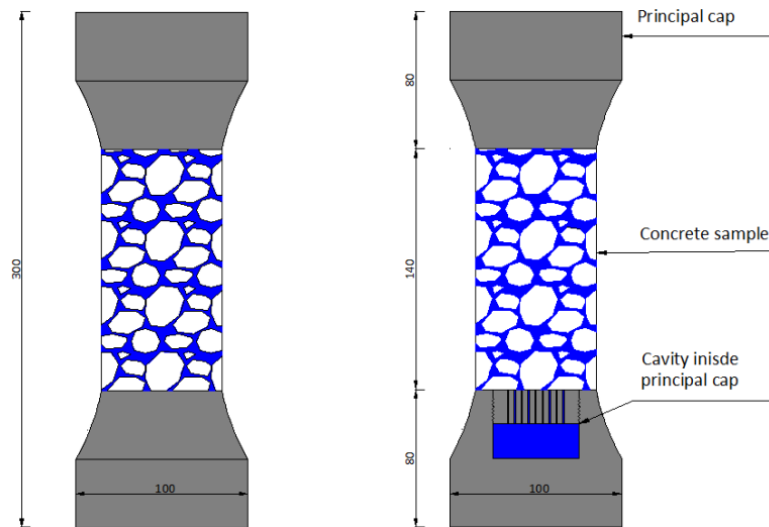


Figure 2.11: Provisional concept: (left) set up before modification (right) modified set up with principal cap and water collect cavity combination

cap material made of tungsten the specific machining needed). In addition, and as I mentioned before, creating the water collect cap does not mean that pore pressure is measurable. Additional sensor has to be designed and implemented in parallel to the water collect cap. It is worth to note that this latter is presented in the drawing without any dimension details and serves only for explanation purposes.

2.7.1.2 Adapted concept

The recent concept consists in reducing the length of concrete sample to 8 cm while conserving its diameter, (Figure 2.12). A water collect cap made of steel is then integrated. With a cylindrical shape of 6 cm in height and 7 cm in diameter the drainage cap occupies the remaining space. It serves to collect water coming from concrete during tests and receives a deformable sensor who can measure the concrete interstitial pore pressure,(Figure 2.13: left). The drainage cap is composed of two parts: an upper one which permits a straight path of the pressurized concrete water to the sensor by means of micro-holes (1 mm of diameter). A lower part which is a movable steel plug allowing an easy access to the cap cavity. The plug is equipped with an O-ring preventing water running out the cavity and DOZ filtering inside it, (Figure 2.13: right).

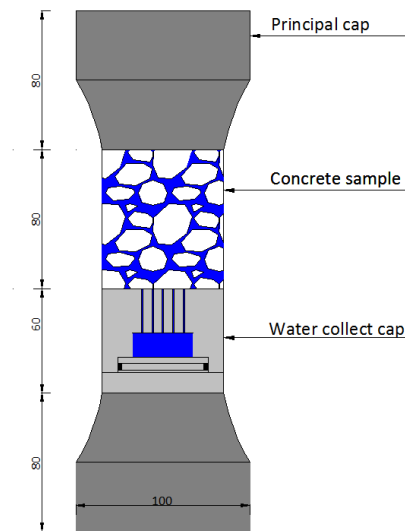


Figure 2.12: Recent concept with the water collect cap integration



Figure 2.13: Drainage cap with micro-holes, plug and sealing joint (left) design (right) real concept

2.7.2 Instrumentation and protection

High confinement pressure generated by the press on the concrete/water collecting cap assembly could disturb the results. The device protection is an essential step to ensure that the experimentation is carried out in good conditions. Normally, the concrete sample and the drainage cap are set as a single body by means of membranes as presented in (Figure 2.14). Two types of membranes are used: the latex and the néoprène membrane. This difference in membrane types is due to the fact that the néoprène membrane resists to the chemical aggression generated by the confinement fluid (DOZ) more than latex membrane, so that, latex membrane can serve to many tests. As for the number of required membranes, it is strongly related to the amount of the applied confinement, (e.g: at 500 MPa of confinement, three layers of latex

membrane each has 2 mm in thickness covered by one layer of néoprène membrane with 1 mm are strongly required. Membranes application technic suggested during previous work is implemented herein, [Gabet, 2006], [Vu, 2007].

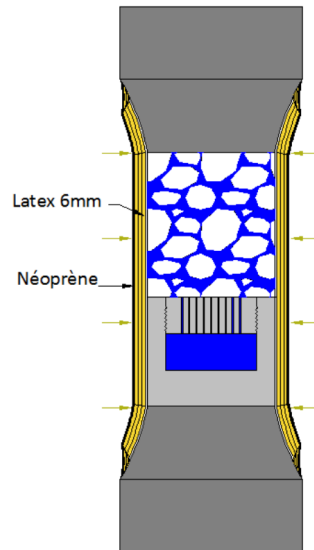


Figure 2.14: Device protection with multiple-layer of *Latex* & *noprne* membranes

In addition, the porous concrete surface has to be well prepared against membrane perforation and fluid penetration under high confining pressure. This penetration can affect concrete properties. To avoid this punching effect, concrete surface has to be carefully prepared before the application of the protective membrane. It consists in opening the surface porosity with a portable milling machine. The opened pores are rubbed and cleaned then filled in with a mortar called *Sikatop*, whose mechanical properties are close to those of concrete, (Figure 2.15).



Figure 2.15: concrete surface porosity and *Sikatop* application: (a) before (b) after

Protection procedure of gage, sensor and wires will be explained in chapter 3.

2.7.3 Calibration test concept

Once the drainage system is defined, a deformable sensor can be placed inside the water collect cap free space. Whatever the shape of the used sensor, its calibration is necessary. Two advantages are provided by performing this calibration: first, it permits to verify both the adapted sensor and the drainage system workability. Second, this test permits to establish a relation between the known applied confining pressure and the sensor deformation. To let the confining pressure be able to reach the cap free space, we suggested to replace the concrete sample by an aluminum cylindrical one. Two holes are driven in the longitudinal and transversal directions of the aluminum specimen. Both holes connects with each other at the middle as shown in (Figure 2.16: left). Thus, once the cap/sensor system is calibrated, we can proceed for pore pressure measurement by using the concrete sample, (Figure 2.16: right)

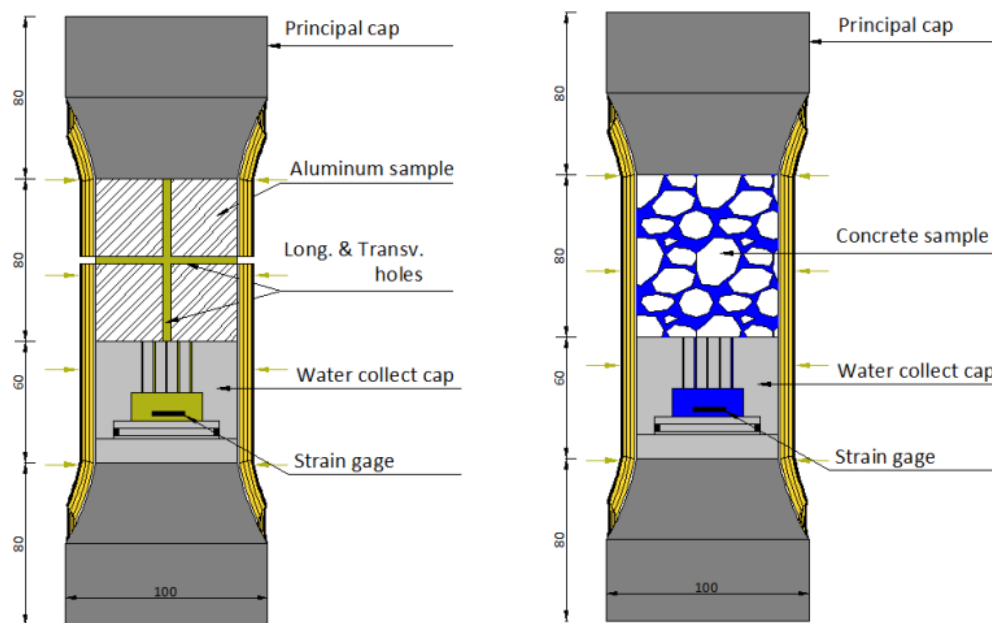


Figure 2.16: Sample and water collect cap arrangement and concept: (left) calibration test on perforated aluminum sample (right) pore pressure test on concrete

As mentioned, the cap alone cannot measure the pressure so that a deformable sensor has to be placed inside its cavity. The idea of [Zingg, 2013] was based on placing a steel metallic thin plat inside the drainage cap. A deformable gage was glued on

the plate top surface. The plate and the gage assembly constitute the pressure sensor where its general concept is shown in (Figure 2.17: left). The author has mentioned that he was able to calibrate the sensor by performing hydrostatic test, (Figure 2.17: right). However, test on concrete sample aiming to measure the pore pressure failed each time. Many reasons are behind the test failure such as: DOZ leakage inside the caps and gage short circuit as he stated. In addition, I found that the thin plate is not adequate for such tests since it might plastically deforms during preparation and thus give wrong results.

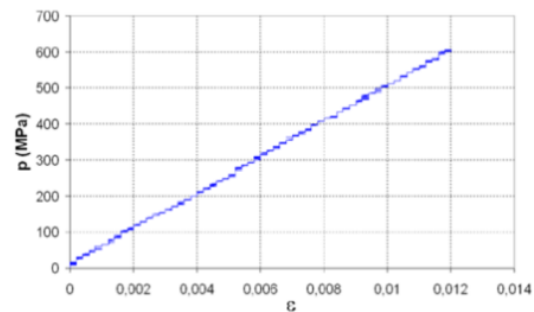


Figure 2.17: Previous results: (left) drainage cap equipped with sensor (right) calibration test result: confining pressure vs. plate strain, [Zingg, 2013]

2.8 Conclusion

The first part of this chapter is dedicated to present the formulation, preparation and conservation of the ordinary R30A7 concrete selected for this study. The R30A7 concrete mechanical behavior is characterized by using the Schenck press. The second part describes the Giga press instrumentation which allows the use of both LVDT and gages for concrete strain measurement. Previous studies have shown that fixing a gage on a wet concrete requires high attention and probably ends by the gage detachment from the specimen. Thus, LVDT calibration test of the new specimen dimension is performed and considered as a reference for concrete strain calculation during hydrostatic tests as detailed. Nevertheless the capability of the press to provide several loading paths, it is shown that drained test can not be performed using the press. Thus, in order to integrate an interstitial pore pressure measurement system, two configurations were discussed. The first one consists in conserving the initial sample length and creating a cavity in the lower principal cap. This idea was not

adapted since the cap material, made of tungsten, is costly and hard to be machined. The second configuration consists in creating a steel water collecting cap having micro-holes on its upper face. This cap, which was equipped by a thin metallic steel plate, is inserted under the shortened concrete specimen. At the end, previous results show the incapability of the proposed sensor to measure any concrete pore pressure. In the next chapter [3](#), a new technics owing to measure concrete interstitial pressure will be presented in detail.

Development of the pore pressure sensor

3.1 Introduction

This chapter presents the experimental campaign aiming to measure the interstitial pore pressure into R30A7 concrete samples subjected to hydrostatic loading at high confining pressure. The water collecting cap described in chapter 2 is used to accomplish the experimental tests. A classic sensor pressure would not be adequate in the presented study due to two main reasons. The first one is the need of a sensor shaped in a specific way and adapted to the case of the GIGA cell, whereas the second reason is the non-availability of small sensor capable to measure high pressure up to several hundred of megapascal. In addition, since the interstitial pore pressure has never been measured in concrete samples under very high confinement, there is a large uncertainty about the magnitude of the pressure to be measured. As a first estimation this magnitude could be based on the fact that it is impossible to get a pore pressure value larger than the confinement applied on the concrete sample during a hydrostatic test. In this study, the pressure is measured indirectly by means of a strain gage glued on deformable sensor. The increase of pressure which surrounds the sensor leads to a change on the strain gage resistance transformed into an electrical output that is recorded by means of a data acquisition system (DAS). Based on this technic, two main configurations were studied to achieve this purpose. The first one consists in using an aluminum cylindrical plate placed in the cap free space saturated with water. The sensor is then subjected to a hydrostatic pressure in all directions that correspond to the interstitial pore pressure. The second configuration consists in creating a steel cylindrical membrane equipped with a sealing joint and embedded in the caps free space. The membrane is then submitted to a deflection

when the pressure to be measured is applied on its upper surface. An overview of the two experimental procedures and devices protection will be presented. Despite a considerable number of failed tests, a specific experimental procedure could be selected to achieve a good measurement of pore pressure during tests. Results of interstitial pore pressure measurement on fully saturated concrete issued from each configuration are then exposed. A new water collecting system developed during this study will be shown at the end.

3.2 Aluminum sensor: hydrostatic type

3.2.1 Sensor description and design

The first configuration consists in inserting a cylindrical aluminum plate into the cap cavity free space, (Figure 3.1: left). The plate dimensions (28 mm in diameter and 10 mm in thickness) are smaller than the one of the cap cavity (35 mm in diameter and approximately 14 mm in height). During a hydrostatic test, the plate is surrounded by the fluid pressure to be measured in all directions where there is no mechanical load on the plate since its dimensions are lower than the cap cavity. Thus, a deformable gage is glued on one of the plate faces. This gage serves to measure the deformation on the sensor during each test (Figure 3.1: right). Figure 3.2 shows the water collecting cap with the hydrostatic sensor placed inside the cap free space. Two holes of 1 mm each were drilled transversely throughout the cap serving to connect gage wires to the DAS.

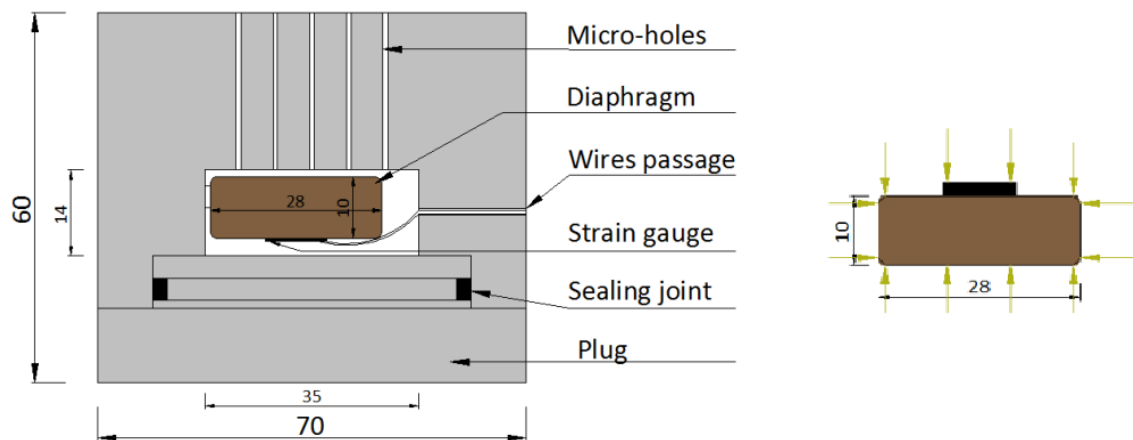


Figure 3.1: Aluminum sensor type hydrostatic: (left) sectional plan of the cap with the hydrostatic load sensor (right) size and loading type of the cylindrical sensor

The aluminum plate has the following elastic characteristics previously identified: Young modulus $E = 80$ GPa, Poisson ratio $\nu = 0.35$. Theoretically, the plate bulk modulus K_{Theo} is equal to 90 GPa refers to (eq. 3.1a). Since this configuration generates an hydrostatic homogeneous stress around the sensor plate, the relation between the applied pressure p and the resultant volumetric strain ϵ_v is given by (eq. 3.1b), where ϵ_v is related directly to the gage deformation ϵ_x by means of (eq. 3.1c). If we consider that this sensor is subjected to a confinement pressure equal to 500 MPa, the plate will deforms homogeneously and in every direction with a magnitude of $\epsilon_x = 0.184$ % which corresponds to a volumetric strain equal to $\epsilon_v = 0.552$ %.

The relation between the Young modulus E , the Bulk modulus K , the confining pressure $p > 0$ and the plate deformations $\epsilon_v < 0$ are given below:

$$K = \frac{E}{3(1 - 2\nu)} \quad (3.1a)$$

$$p = K\epsilon_v \quad (3.1b)$$

$$\epsilon_v = 3\epsilon_x \quad (3.1c)$$



Figure 3.2: Picture of the aluminum sensor type hydrostatic: (left) water collect cap, plug, sealing joint and the hydrostatic sensor (right) sensor placed inside the water collecting cap

3.2.2 Sample position

This section describes how the calibration is carried out and the preparation of pore pressure measurement tests. At the beginning, the sensor described in the previous

section is placed into the cap cavity where the connection wires pass through two perforated holes. In order to conduct the calibration test, a hollowed cylindrical aluminum specimen able to perfectly transmit the confining through the sample is used instead of a concrete sample.

To verify the drainage system efficiency, two types of configuration were adapted. The first configuration called reversed calibration (Figure 3.3) consists in putting the cavity free space in direct contact with the aluminum sample without using the plug. This method guaranties the passage of the confining fluid to the sensor inside the cap and allows testing the system efficiency.

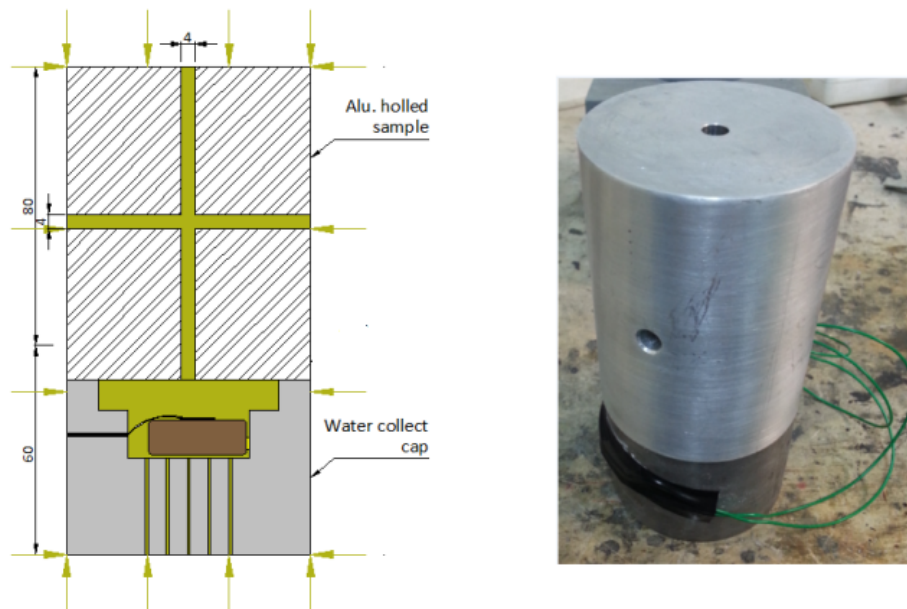


Figure 3.3: Hydrostatic type sensor: reversed calibration test (left) design (right) real picture

The second configuration called normal calibration (Figure 3.4) is similar to the one used for pore pressure measurement, in which the cavity micro-holes meet the longitudinal hole of the aluminum specimen.

3.2.3 Sample protection

To prevent concrete from losing humidity during the preparation process, a sponge is attached on its lower face, (Figure 3.5: left). Once the set is ready, the protective membranes are applied and the connections wires are taken out gently using a specific technic, (Figure 3.5: middle). Finally, the cap cavity is pre-saturated by the adequate

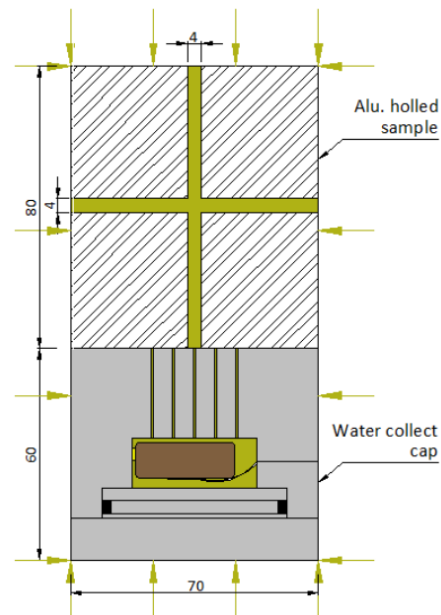


Figure 3.4: Hydrostatic type sensor: normal calibration test design

fluid before the test, (e.g.: by the DOZ for calibration or by water for pore pressure measurement), (Figure 3.5: right).



Figure 3.5: Experimental procedure: (left) sponge attached on concrete lower surface (middle) applying of protective membranes (right) saturation of the water collecting cap before the test

The protection process is the most important step in the preparation procedure. It permits to conserve the continuity of gage signals and protect wires from being cut

during a test. The movable part of the drainage cap is equipped with an O-ring joint to avoid any mixture between the confining fluid (DOZ) acting from the outer side and the water locked inside the cavity free space. In addition, there are two critical zones under high confinement that correspond to the two wires passage holes. These zones may cause wires cutting and membrane perforation inside the cavity, (Figure 3.6:left). Yet, another wire weak point lies at cap/specimen interface causing signals discontinuities, (Figure 3.6: right).



Figure 3.6: Device weak points: (left) membrane penetration (right) wires cut at cap/specimen interface

To get rid of these situations, first two pieces of latex is put under the wires to reduce the friction near both holes, (Figure 3.7(a)). Second, a cylindrical shaped plastic shield is applied on wires holes as a protection from confining pressure. The assembly is then protected by means of an insulating paste (CAF-4) along all edges, (Figure 3.7(b)). In addition, a rectangular piece of latex membrane is glued on the cap/sample interface before applying the main membranes on which connection wires passes smoothly, (Figure 3.7(c)). During preliminary tests, a signal perturbation was observed during measurements and we found that the fact of filling the cavity by water without protecting the gage might be the reason behind. Thus, a protective mastic called *Dow – Corning* is then applied on the top of the gage as shown in Figure 3.7(d).

3.2.4 Sensor calibration test

The main objective of these tests is to establish a relation between the hydrostatic pressure on the sensor and the sensor deformation. Four succeeded hydrostatic calibration tests up to 400 or 500 MPa were conducted on the aluminum cylindrical plate

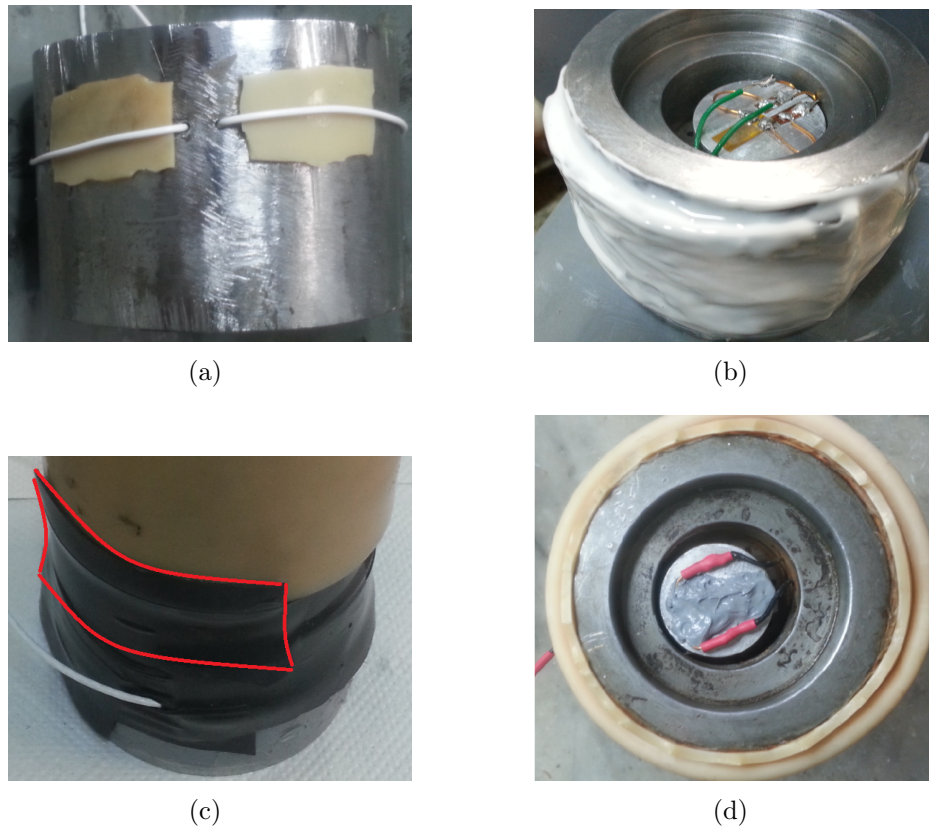


Figure 3.7: Device protection: (c,d) wires passage protection (e) protective membrane at the interface (f) gage protection

for both sample/cap position as described in (table 3.1). The cavity is filled by the confining fluid (DOZ) before the beginning of each experiments. Three tests were performed without any gage protection while the gage of the last one was protected to study its effect on the overall behavior of the sensor/gage system.

Experimental calibration test results are presented in Figure 3.8 where the loading pressure is plotted versus the gage volumetric strain. A quasi linear increase of the sensor deformation is observed as the pressure increases. The slope of each curve corresponds to the sensor bulk modulus. It is clear that the repeatability of the calibration test was good. A maximum difference of 3% between the theoretical value (aluminum bulk modulus) and the experimental one is also observed. This difference is probably due to a very slight mechanical effect during the experiments where the sensor outer side can slightly be in contact with the cap cavity wall and thus minimize its deformation. A mean value of 93 GPa for the bulk modulus can be deduced and will be used to calculate the concrete interstitial pore pressure.

Test No.	Position	Protective mastic	p_c (MPa)	Slope K (GPa)
Calib-1	reversed	Non	500	94
Calib-2	reversed	Non	500	92
Calib-3	normal	Non	400	93
Calib-4	reversed	Yes	400	93
Theoretical	—	—	500	90

Table 3.1: Description of calibration test: sample/cap configuration, condition and identified slope value

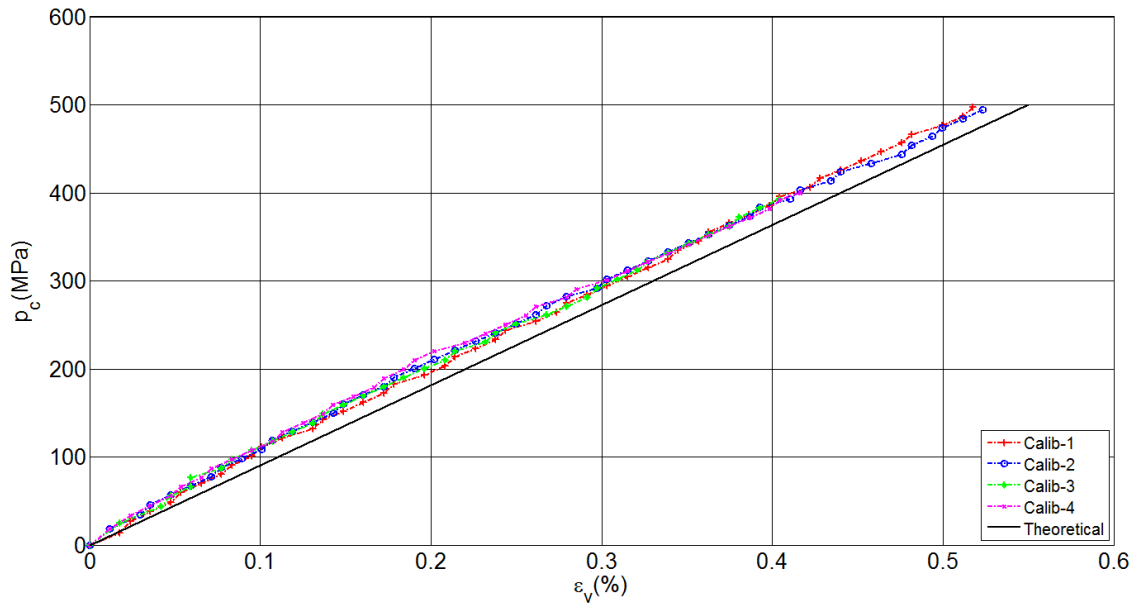


Figure 3.8: Calibration test results on the aluminum sensor type hydrostatic: hydrostatic loading pressure p_c vs. sensor volumetric deformation ϵ_v (positive in compression)

3.2.5 Interstitial pore pressure measurement in concrete samples

The hydrostatic sensor is used to measure the interstitial pore pressure in a concrete sample after being calibrated. Several tests on saturated ordinary concrete specimens are performed under hydrostatic loading up to high confining pressure. The cylindrical sensor equipped with the gage is protected with a mastic and then placed into the cavity of the cap. Once the protection and instrumentation procedures of the test are achieved, the cavity is filled with water then plugged. It is worth to note that, many tests were interrupted from the beginning. This has led to an improvement of the device protection along the experimental campaign.

Preliminary results

The first attempt tests were performed on fully saturated ordinary concrete (O.C) specimens issued from an old block that had a composition close from the R30A7 reference concrete. The block itself was conserved more than two years in water. Table 3.2 shows results of five hydrostatic tests performed up to high confinement and indicates the maximum interstitial pore pressure reached.

Test name	Concrete	p_c (MPa)	Δt (min)	Interrupted	$p_{i,max}$ (MPa)
p_i -1	O.C	600	5	Non	150
p_i -2	O.C	500	5	Non	350
p_i -3	O.C	500	5	Non	360
p_i -4	O.C	500	15	Yes	380
p_i -5	O.C	400	15	Non	420

Table 3.2: Description of the preliminary hydrostatic test on concrete using the hydrostatic sensor type: test name, concrete type, loading time, test condition, maximum interstitial pore pressure

Results of the first attempts tests are also gathered in (Figure 3.9) where the interstitial pore pressure p_i is plotted versus the confinement pressure p_c . Similar behavior of $p_i(p_c)$ is observed at the beginning of tests 1 and 4 where the pore pressure remains null until 50 MPa of confinement. Many reasons can explain this kind of behavior: first the water collecting cap may not be completely saturated before the test which induces a late response of the deformable sensor even though the confining pressure starts to increase. Second, this behavior can be related to a default in the sensor itself, this means that the real p_i is not the one measured into the cap. Beyond

a confining pressure of 50 MPa tests 2,3,4 and 5 show a similar behavior where the interstitial water pressure increases quasi-linearly until the end of each test. In addition, test number 1 is the only one that shows a plateau starting from 200 MPa of confinement after which the pore pressure slightly increases. This behavior can be related to concrete compaction and granular degradation beyond which may block the cap micro-holes and thus prevent water from infiltrating inside the cap cavity.

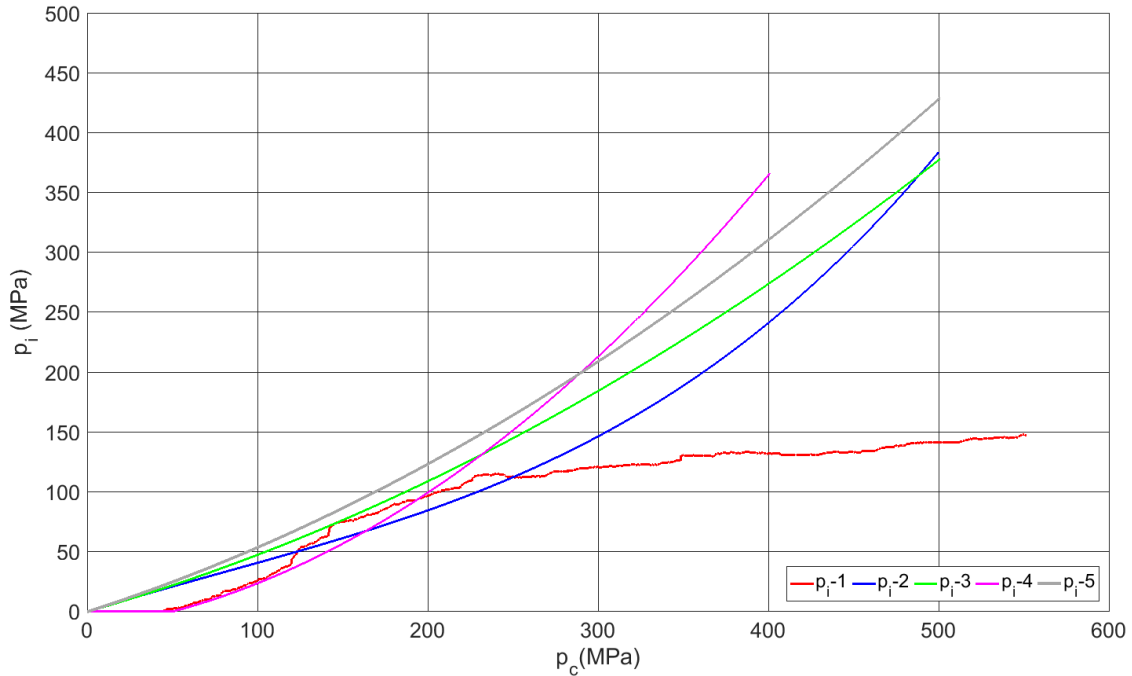


Figure 3.9: First interstitial pore pressure measurement results on R30A7 concrete: pore pressure vs. confining pressure

The second attempt tests are performed on fully saturated reference concrete specimens R30A7 issued from a new casted concrete block that were well controlled in term of composition and making process. The saturation period between concrete casting and the first test was approximately five months. Table 3.3 shows four hydrostatic tests conducted at a high level of confinement with the maximum interstitial pore pressure attained. Figure 3.10 depicts the amount of interstitial pore pressure measured versus the applied confining pressure. The signal of tests 6 7 and 8 are conserved until the end of the loading and show a linear increase of the pore pressure along the loading phase. However, test 7 displays a similar behavior compared to the test 1 but with one difference, the plateau of the test 1 curve starts at a confining pressure of 300 MPa against 200 MPa for the test 1. Test 9 is coherent with pre-

vious tests at the beginning, but unfortunately, the signal was lost at 150 MPa of confinement due to a gage dis-functioning.

Test name	Concrete	p_c (MPa)	Δt (min)	Interrupted	$p_{i,max}$ (MPa)
p_i -6	R30A7	400	5	Non	200
p_i -7	R30A7	500	5	Non	215
p_i -8	R30A7	500	10	Non	250
p_i -9	R30A7	500	5	Yes	140

Table 3.3: Description of the preliminary hydrostatic test on concrete using the hydrostatic sensor type: test name, concrete type, loading time, test condition, maximum interstitial pore pressure

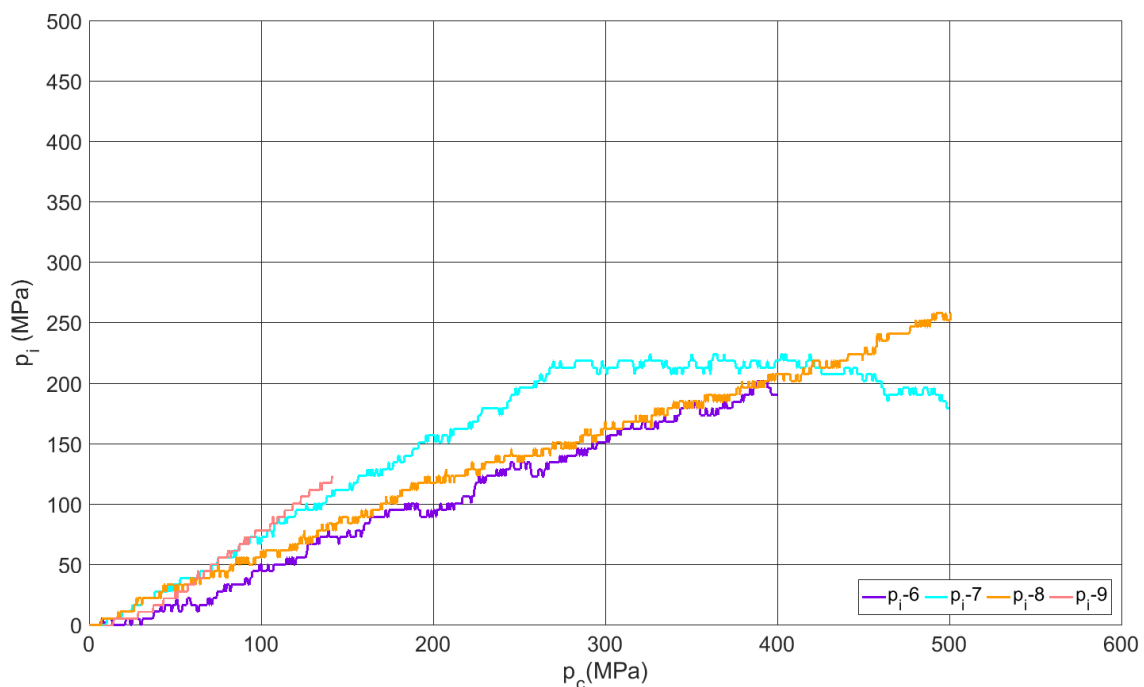


Figure 3.10: Hydrostatic test on saturated R30A7 samples: pore pressure vs. confining pressure

Test 6 is the only test who conserved a null pore pressure from the beginning until 30 MPa of confining pressure. A very close behavior of tests 6 and 8 is observed, however, since the confinement applied during test 8 is higher than the one of test 6, a higher value of pore pressure is reached. However, one can see that the slopes of tests 7 and 9 are steeper than those of the tests 6 and 8. Since no leakage of confining fluid was detected into the cavity for these tests, so there is no outer pressure (except the

water pore pressure) acting on the sensor. The observed difference is then probably due to the pores distribution in the concrete samples that may change from one sample to the other.

3.3 Membrane sensor

3.3.1 General description and design

The design of the second configuration of pressure sensor is presented hereafter. The new concept has to respond to many specifications such as: guaranty a good sealing of the gage and the wires from the confining fluid, amplifying the sensitivity of the sensor and having more precise measurement. Thus, the idea is to create an element that can deflect under a certain amount of pressure force and remain in the elastic domain. One of the most compatible devices to use is the diaphragm pressure transducer equipped with some sort of measuring system inspired from Murry and Miller work [William and William, 1992]. To reach this purpose a cylindrical sensor is built acting as a flexible membrane once the pressure is applied on its upper surface, (Figure 3.11).

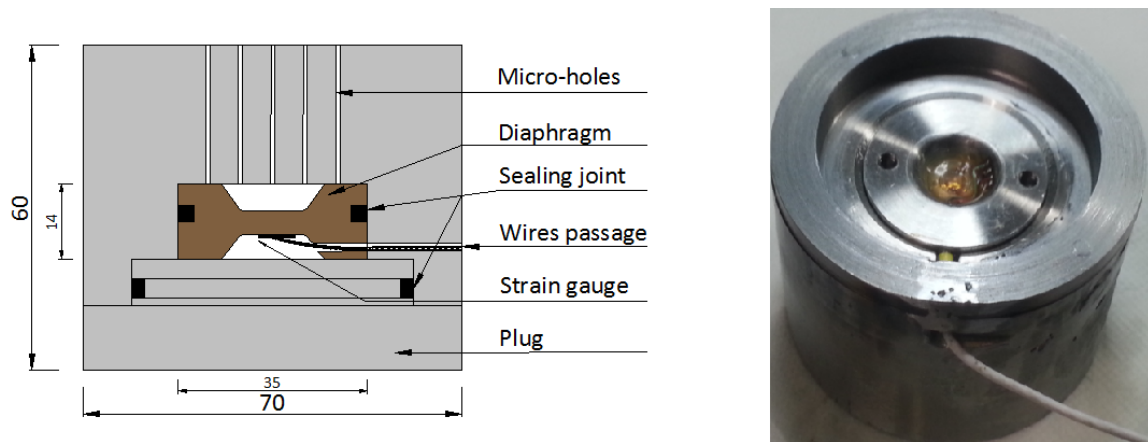


Figure 3.11: Steel sensor type membrane (a) sectional plan of the cap with the membrane sensor (b) picture of the cap with the membrane sensor

The sensor has the same dimensions than the cavity of the water collect cap (approx. 35 mm in diameter and 14 mm in height). Sensor deflection is emphasized by the difference between its inner and outer thickness. Gage position is selected at the center of the sensor back face where the strain is the largest. To facilitate the wires passage, it was decided to drive only one hole of 1.5 mm in the transverse cap

direction in order to connect gage wires with the DAS. In order to have a maximum gage/wires protection from fluid leakage, a sealing joint groove was shaped at the sensor outer diameter. To guaranty an elastic sensor behavior under pressure, its thickness, superior and inferior length have to be well chosen (Figure 3.12). Thus, three sensor geometries were studied to evaluate their resistance and sensitivity. The appropriate sensor is the one who can deforms the most giving a maximum sensitivity under a certain amount of pressure and remains in the elastic domain. Therefore, three sensors with different initial thickness of 2.5, 4.5 and 7 mm are modeled on Abaqus. To facilitate the gage implementation, the sensors inferior length is fixed equal to 4.5 mm. In consequence and since all sensors have the same total length, their superior length varies as described in (table 3.4) and shown in (Figure 3.13).

Sensor	l_{sup}	l_{mid}	l_{inf}	l_{total}	d
s_1	7	2.5	4.5	14	35
s_2	5	4.5	4.5	14	35
s_3	2.5	7	4.5	14	35

Table 3.4: The dimensions of the different proposed sensors (in mm)

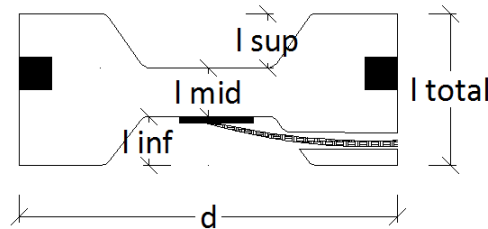


Figure 3.12: General design of the membrane sensor with the gage and sealing joint positions

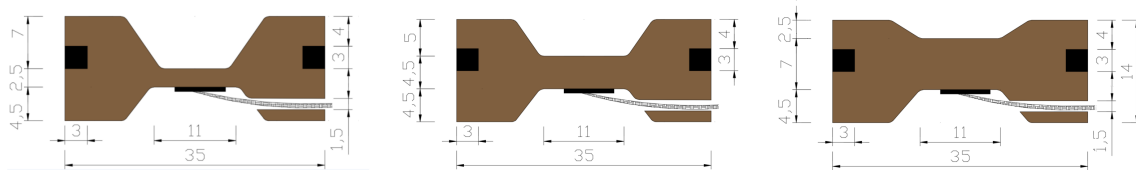


Figure 3.13: The design and geometry of different suggested sensors (left) s_1 (middle) s_2 (right) s_3

3.3.1.1 Loading and boundary conditions

During a test, the sensor can be subjected to two kinds of solicitation. The first kind of load represents the interstitial pore pressure p_i that is to be measured acting on the sensor upper surface and on the upper point of the lateral surface up to the sealing joint. This pressure is supposed to be in equilibrium with the pressurized free water inside the concrete sample, (Figure 3.14).

The second kind of loading is more difficult to characterize. It corresponds to a potential mechanical effect (ME) due to the interaction between the cap and the sensor. The confining pressure p_c acting on the cap outer surface generates a displacement u_{pc} on its inner surface (Figure 3.15). This displacement might be transmitted from the cap to the sensor lateral surface once the contact between them occurs (Figure 3.16). The radial tolerance between cap/sensor diameters is imposed by the manufacturer and is equal to 0.015 mm. Thus, the real imposed displacement will be $u_{pc} + u_{tol}$.

Regarding the boundary conditions, the sensor upper and lower surfaces are constrained in displacement in the vertical direction and free in the horizontal one. The vertical contact between the sensor surfaces from one side and the water collect cap and the plug from the other side is not well known. Therefore, it is suggested to apply two types of boundary conditions in order to study their effects on the stress and strain distribution inside each sensor. The first consists in blocking the vertical displacement of all the upper and lower nodes, where in the second only half of the nodes are blocked.

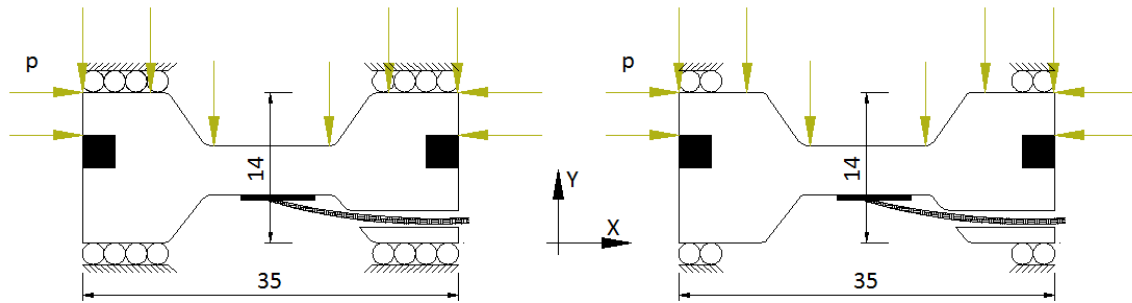


Figure 3.14: Applied pore pressure p_i on the sensor upper surface (left) all nodes blocked vertically (right) half nodes blocked vertically

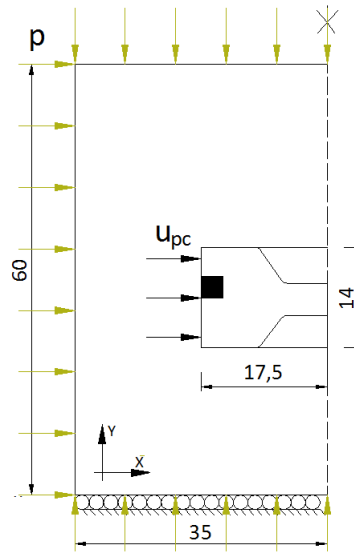


Figure 3.15: Mechanical effect on the water collect cap lateral surface with the boundary condition: displacement u_{pc} due to the confining pressure

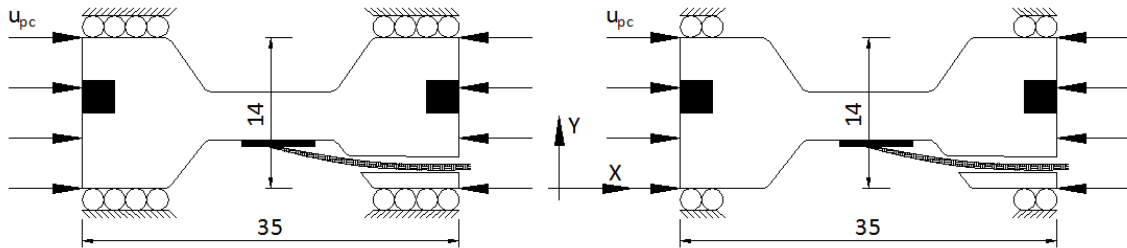


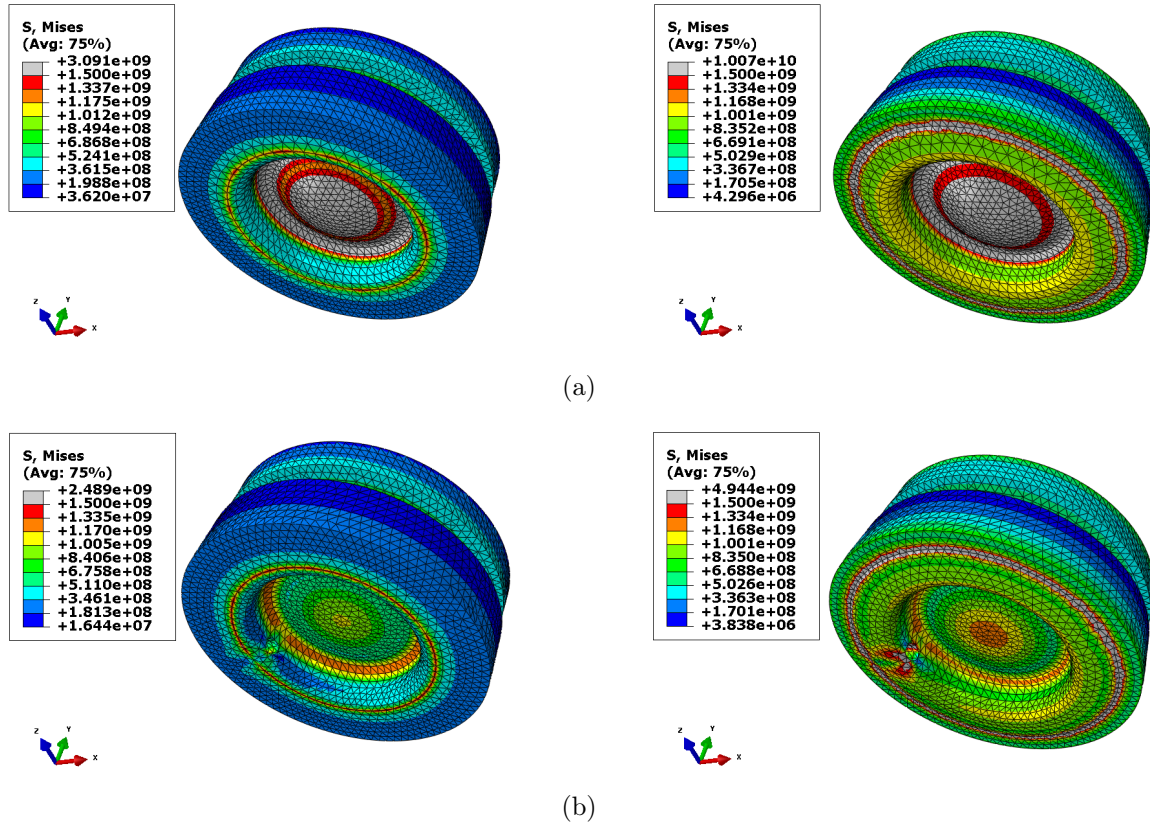
Figure 3.16: Mechanical effect on the sensor lateral surface: transmitted displacement from the cap to the sensor (left) all nodes fixed (right) half nodes fixed

3.3.1.2 Stress analysis

During a hydrostatic test, the measured interstitial pore pressure magnitude is lower than the confining pressure. This statement has been proved by means of experimental tests where the pore pressure reached is 400 MPa for 500 MPa of confinement, (sec. 3.2.5). Therefore, we choose that the future sensor will be adapted to sustain 400 MPa of pore pressure measurement. In order to know the maximum stress reached in each sensor, elastic calculations were performed using Abaqus software. A passage hole of 1.5 mm for wires connection and a groove to receive the joint of 3 mm in depth were created to meet the real design. Sensors mechanical properties were selected as the following: Young modulus $E = 210$ GPa, Poisson ratio $\nu = 0.3$. Only the interstitial pore pressure $p_i = 400$ MPa with both types of boundary conditions

were applied on each sensor as explained in (sec. 3.3.1.1). Figure 3.17 depicts the Von Mises stress as obtained from the numerical simulations and (table 3.5) gathers the maximum Von Mises stress due to the sensor flexure located at the central part of each sensor back face.

First, when the thickness of the sensor decreases the stress on its central part and inner corner side increases. Therefore, the thinner sensor $s1$ shows a very high stress level (Figure 3.17(a)) whereas the $s3$ sensor shows the lowest stress level (Figure 3.17(c)). Second, the effect of the sensor boundary condition is clear on the stress results. For example, the stress level of the $s2$ sensor, when all nodes are blocked vertically, is lower than the stress level when only half of nodes are blocked vertically (Figure 3.17(b)). Third, the excess of the stress shown in the results of the $s2$ and $s3$ sensor is due to the influence of the imposed boundary condition.



3.3.1.3 Sensitivity analysis

Sensors sensitivity is also an important factor leading to choose the adequate sensor thickness. Referring to the same numerical simulations, the applied pressure is plotted

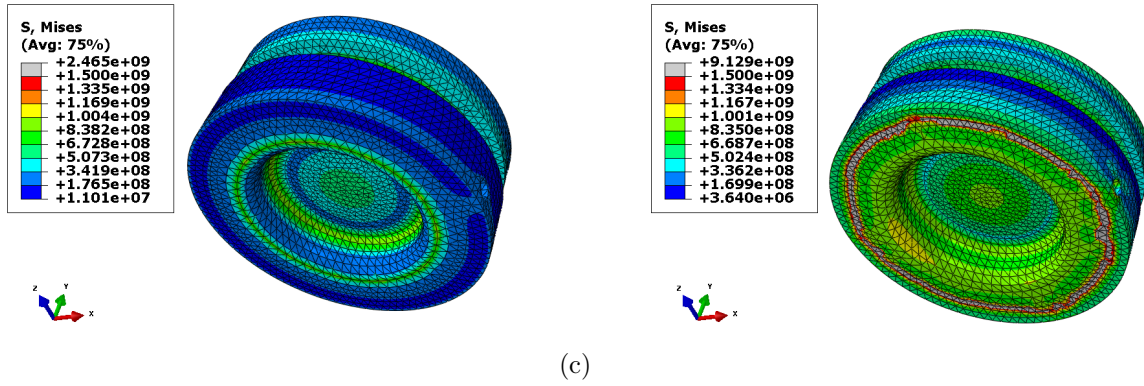


Figure 3.17: Sensor Von Mises stress distribution for 400 MPa of water pressure and both kind of boundary conditions. Left column nodes are all fixed, right column half of nodes are fixed: (a) s_1 (b) s_2 (c) s_3

Sensor	$\sigma_{V.M.}$ (MPa) all nodes	$\sigma_{V.M.}$ (MPa) half nodes
s_1	2600	2800
s_2	1000	1240
s_3	590	860

Table 3.5: The maximum Von Mises stress for the three types of sensor for both boundary conditions

versus the sensors radial strain located at the center of their back faces, (Figure 3.18). Values are derived from the strain field results shown in, (Figure 3.19). It is worth to note that the radial and tangential strains are equal at the central part of the sensor.

It is clear that a sensor with a thinner thickness is more sensitive to the applied load. The sensor strain tends to increase when the thickness decreases. For example, the strain obtained for the s_1 sensor is three times higher than the one observed for the s_3 sensor. Regarding the boundary conditions effect, when the number of constrained nodes is lower the three sensors tend to deflect more. It is also obvious from (Figure 3.19) that the interstitial pore pressure causes sensor tension at its back face which leads to positive strains.

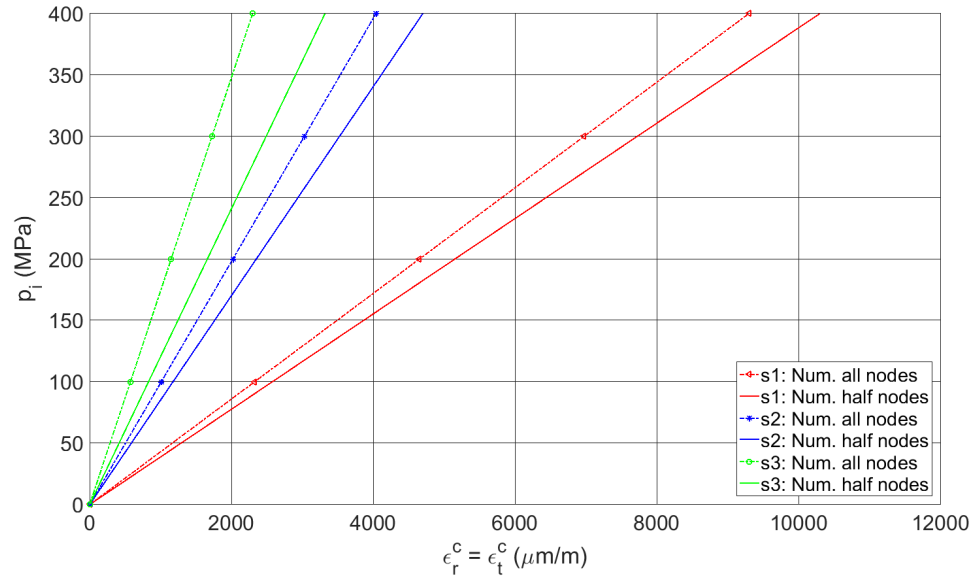
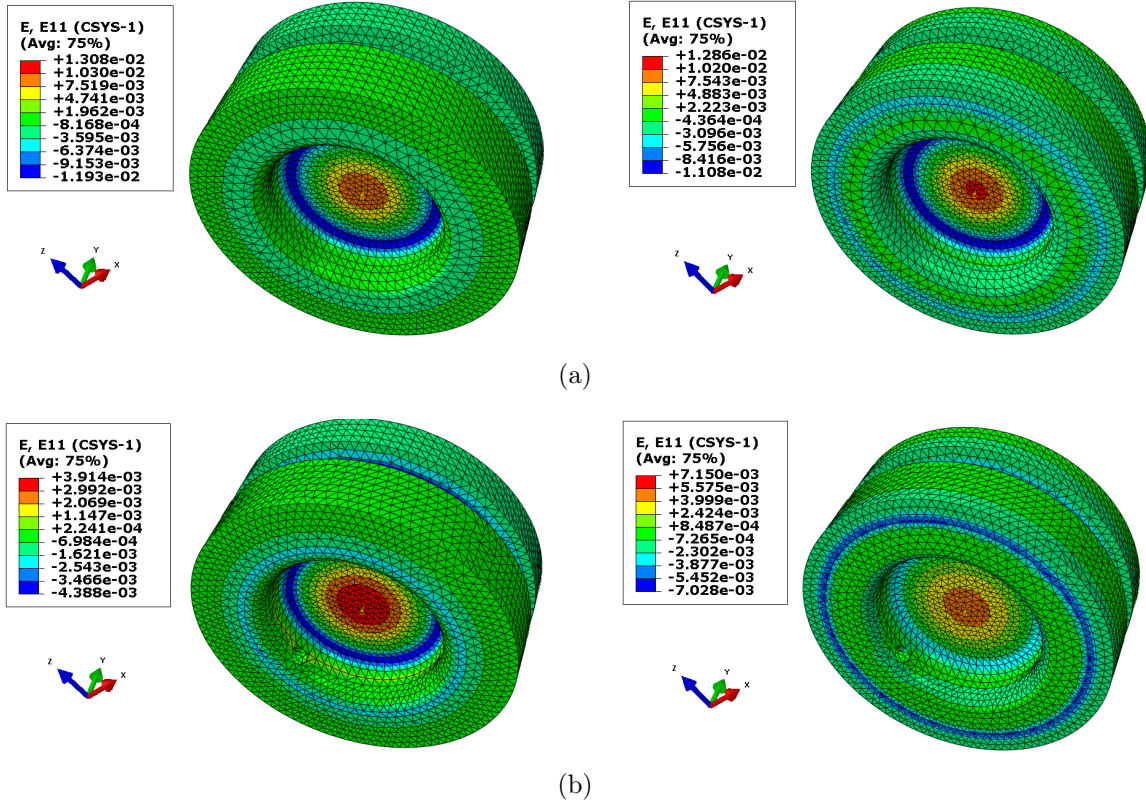


Figure 3.18: Sensor sensitivity: strains comparison for the three types of sensor for both boundary conditions: applied pressure vs. radial (or tangential) strain at the sensor center back face, (positive strain in tension)



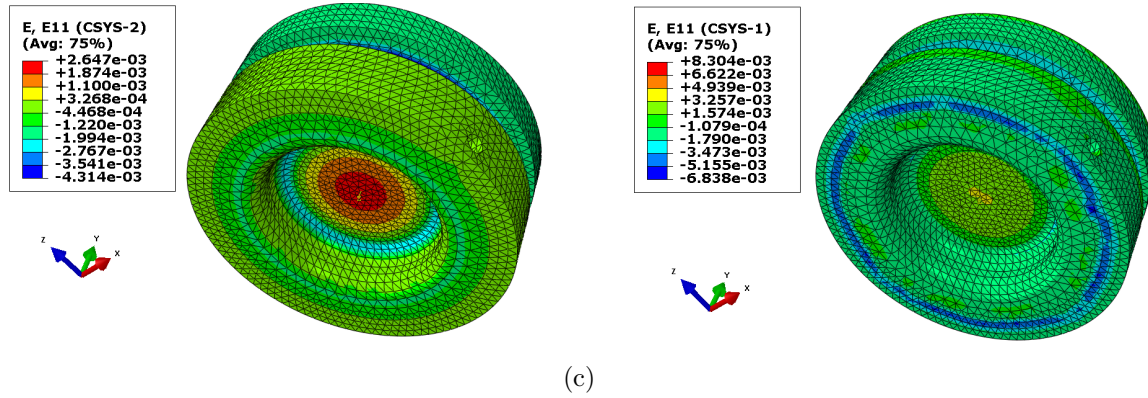


Figure 3.19: Sensor radial (or tangential) strain field at the sensor central part calculated for 400 MPa of pressure for both boundary conditions. Left column all nodes fixed, right column half nodes fixed: (a) s1 (b) s2 (c) s3

3.3.1.4 Geometry validation

Sensor geometry is selected carefully to meet two major aspects in the same time. The first one is based on sensor capability to deflect properly while remaining in the elastic domain. Calculations have shown that the s_1 has a very high Misses stress. The s_2 and s_3 sensors display a maximum stress which not exceed the 1300 MPa. Thus, a steel called *TOOIX44* having a high elastic resistance $\sigma_e = 1400$ MPa is hence chosen for the material fabrication process. The second aspect is the sensor sensitivity with respect to its thickness as it is explained in (sec. 3.3.1.3). The s_1 sensor is eliminated since it is unable to resist the desired load in spite its high sensitivity. On the contrary, the s_3 sensor displays a high resistance capacity but has a low sensitivity in particularly for low and intermediate pore pressure. Thus, the s_2 sensor has been selected as the deformable membrane for the rest of this study as it responds the most to the technical requirements.

3.3.1.5 Mechanical effect

The mechanical effect on the cap/sensor is studied numerically on Abaqus following the explanation in (sec. 3.3.1.1). In the first step, the water collect cap is numerically simulated on Abaqus by applying a confining pressure p_c of 400 MPa on its outer lateral surface. Figure 3.20 shows a homogeneous displacement field at the cap inner surface with a maximum displacement u_{pc} of -0.0418 mm.

Figure 3.21 depicts the confining pressure versus the inner cap displacement for different pressure values. When the initial distance between the cap/sensor (tolerance

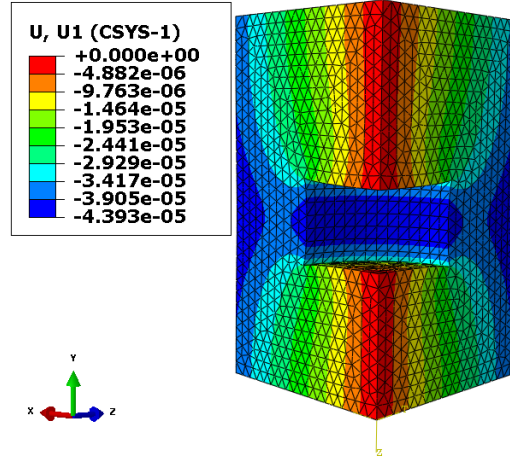


Figure 3.20: Water collect cap displacement for 400 MPa of pressure: simulation result of the lateral displacement field

u_{tol} 0.015 mm) is considered, the effect of the cap displacement begins to appear at 145 MPa of confinement ($u_{pc} + u_{tol}$, red curve). It is worth to note that the effect of the vertical cap displacement on the sensor upper and lower surfaces is negligible compared to the displacement generated from the pore pressure. In the second step, the resultant displacement (red curve) is applied on the $s2$ sensor lateral surface. It is observed that the mechanical effect has a negative influence on the sensor causing its deflection upwardly (opposite to the interstitial pressure direction) leading to negative strains at its central part, (Figure 3.22). For each confining pressure, the cap displacement, the resultant one applied on the sensor after adding the tolerance and the sensor response in term of deformation are calculated as given in (table 3.6).

p_c	water collect cap		$s_{2,half-nodes}$	$s_{2,all-nodes}$
	u_{pc} mm	$u_{pc} + u_{tol}$ mm	ε_r $\mu m/m$	ε_r $\mu m/m$
0	0	0.015	0	0
100	-0.01045	0.00455	0	0
200	-0.0209	-0.0059	-400	-409
300	-0.03135	-0.01635	-1127	-1133
400	-0.0418	-0.0268	-1840	-1890

Table 3.6: Calculation details: cap displacement and sensor deformation

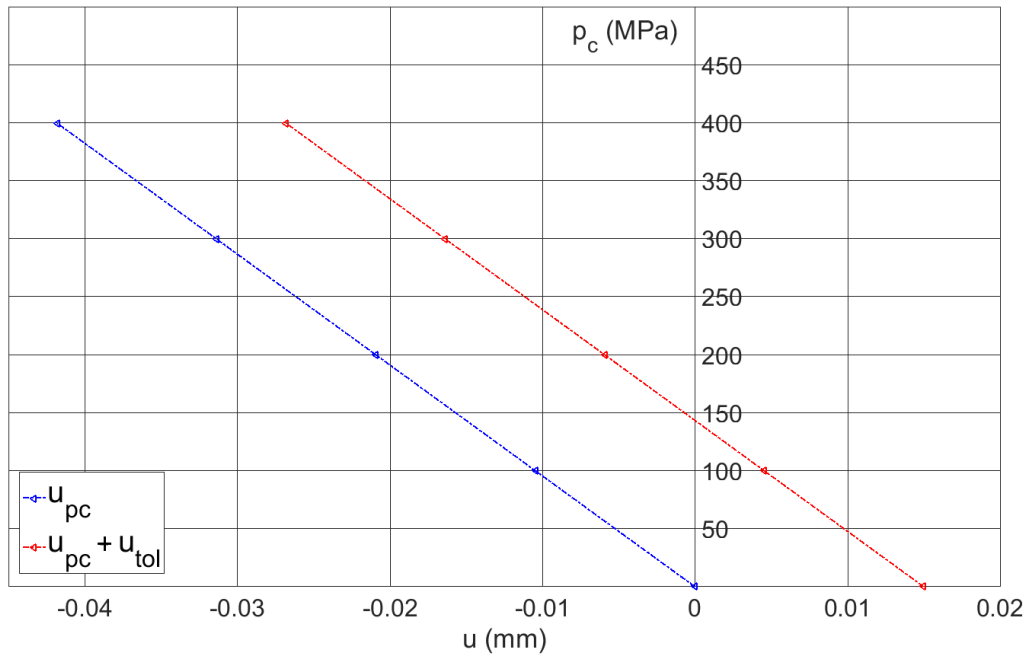


Figure 3.21: Water collect cap displacement for 400 MPa of pressure: applied pressure vs. cap inner displacement with and without counting the tolerance

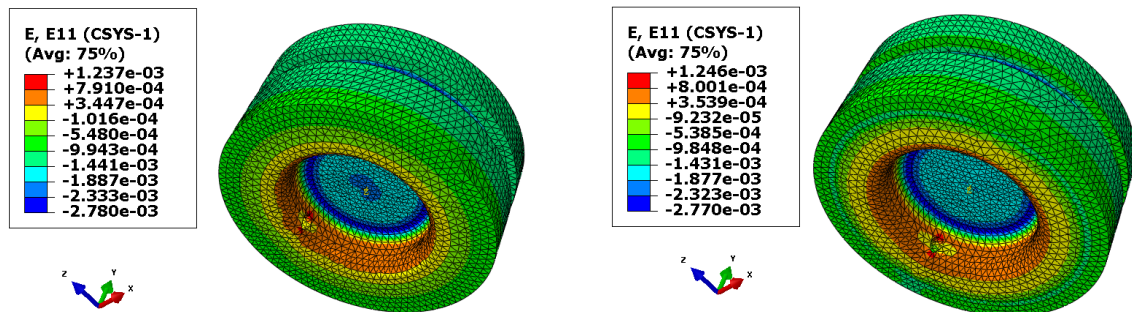


Figure 3.22: Sensor $s2$ radial (tangential) strain field at the central part for an applied displacement ($u_{pc} + u_{tol.}$) equal to -0.0268 mm: (left) all nodes (right) half nodes fixed

For the seek of simplicity, the pressure applied on the cap outer surface is presented versus the corresponding sensor deformation, (Figure 3.23). In the same way this effect starts to appear on the sensor at 145 MPa where a slight effect of the boundary conditions is observed. Simulation results for both calibration and mechanical effect are gathered in (Figure 3.24) where the sensitivity of the sensor regarding the pore pressure is higher than the displacement coming from the water collect cap.

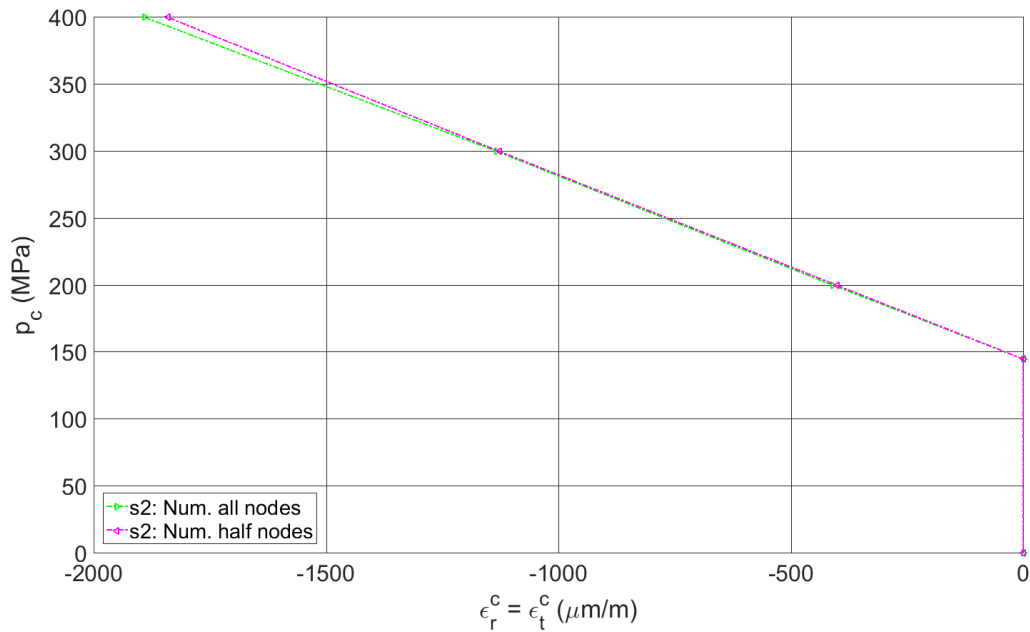


Figure 3.23: Mechanical effect on the sensor sensitivity after applying the tolerance: p_c vs. $\epsilon < 0$ in compression

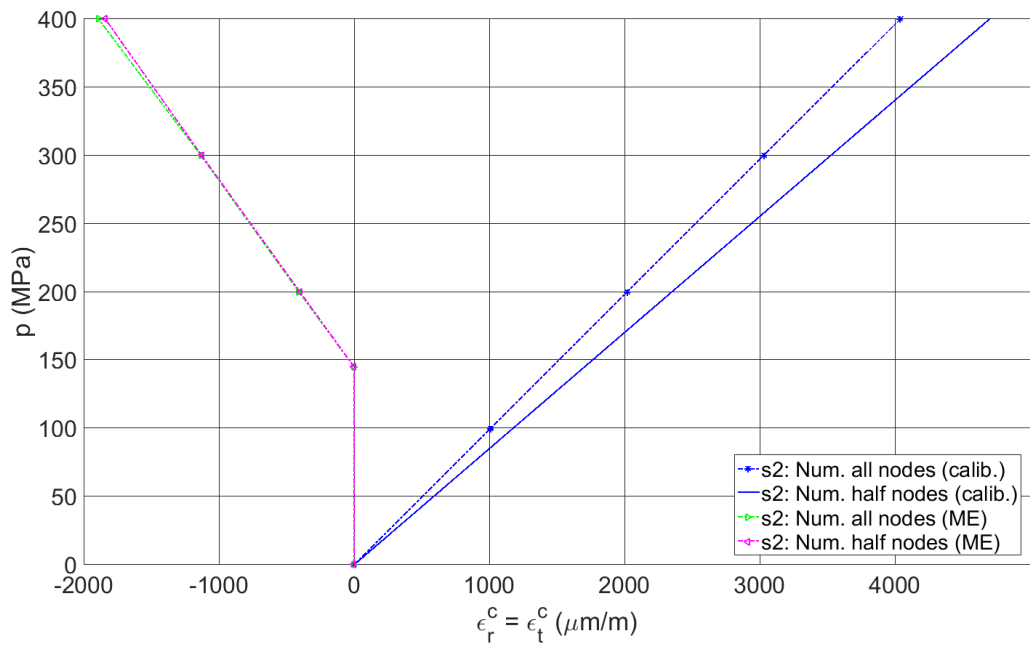


Figure 3.24: Calibration and mechanical effect on the sensor sensitivity after applying the tolerance: p vs. strain ϵ

3.3.2 Experimental procedure

3.3.2.1 Sensor protection

Several types of gage and wires protection are applied to assure a good system performance. First, a cylindrical sealing ring of 3x3 mm in thickness and depth is placed at 4 mm from the sensor upper surface so that the fluid infiltration to the gage is stopped. The joint is made of two sub-items: the first item (Fig. 3.25(a)) is made of a high elastic ring which can be easily introduced once it is stretched. The second item (Fig. 3.25(b)) which is more rigid than the first one is immersed in hot water at 50°C then expanded using a conical system with higher diameter. Both items are then embedded in their specific place on the sensor by applying a metal clamp for one hour as shown in (Figure 3.25(c)). Second, to minimize the risk of gage degradation during the preparation process and tests, a kind of resin epoxy is applied on the upper gage surface, (Figure 3.25(c)). Finally, an aluminum shield grooved on its inner side and having the same cap curvature is used to protect the connection wires passing through cap holes, (Figure 3.25(d)).

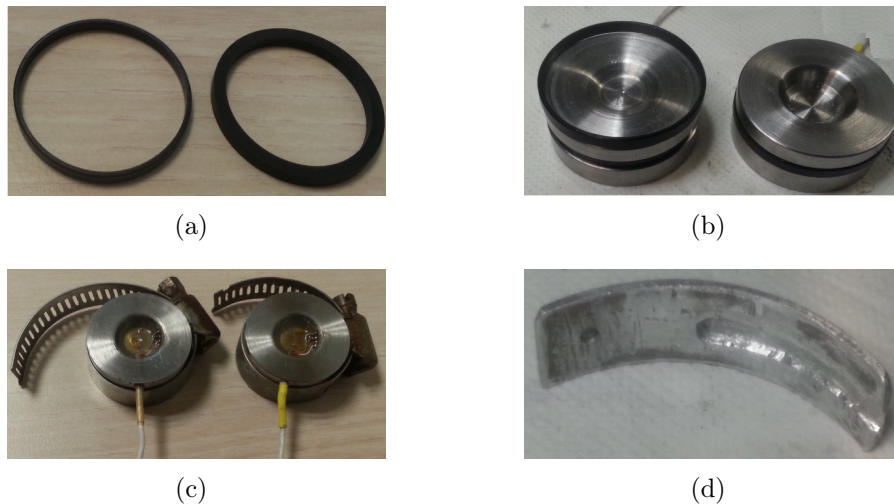


Figure 3.25: Sensor protection (a) joints made of two sub-items (b) joint insertion (c) application of the metal clamp (d) aluminum grooved shield

3.3.2.2 Cap and sensor set up

The preparation procedure of this sensor configuration is more complicated than the first one (sec. 3.2.2). In fact, the saturation of the cap cavity has to be accomplished

carefully for both calibration and pore pressure tests before the application of the protective membranes. Some rapidity is required while applying wires protection as it will be explained. The two existing cap holes of 1 mm each was closed by means of a welder and only one hole of 1.5 mm created to facilitate the insertion of wires/sensor system without any damage. The water collect cap is placed inside a tank filled by the adequate liquid. In parallel, the connection wires passing throughout the hole and the sensor are inserted gently inside the cavity, (Figure 3.26: left). After that, the cap is moved to a smaller tank to maintain a wet environment, (Figure 3.26: right). Then, a silicone (*Dow – corning*) which acts as an additional protection is applied on the sensor upper surface. Once it's dry the cap is closed by its movable part and the aluminum shield wires protection is glued. Finally, an insulating paste (CAF-4) is used to cover the shield border and a metal clamp tool is fastened around the cap to assure shield-caps solidarity, (Figure 3.27: left). After this stage, the preparation process becomes the same as the first configuration explained in (section 3.2.2). In addition, difficulties are faced while taking out the sensor after being inserted in the cap cavity. Practically, installing the sensor is done by applying a moderate force on its upper face due to the joint friction. The joint takes its place once the sensor is introduced. Dismantling by hitting on the cap is not an adequate idea, it may lead to ruin the cap, sensor and gage. Thus a lifting device equipped with four screws is machined then used. The two inner screws are driven in the sensor threaded hole so that the lifting device is attached to the sensor. The two outer screws act like a support on the cap outer edge. This solution is easy and protective. once the inner screws are connected to the sensor, the outer screws are driven up gently until the sensor is released, (Figure 3.27: right).



Figure 3.26: Test preparation: (left) cap saturation (right) sensor insertion



Figure 3.27: Test preparation: (left) application of the wires protective metal clamp shield (right) sensor lifting device

3.3.3 Full bridge: diaphragm patterns

The sensor is acting as a flexure membrane with positive and negative bending. As a first suggestion, and in order to cover a wide range of deformations, a diaphragm pattern equipped with a set of two radial and two tangential gages fixed on a circular support is glued on the sensor back face by the supplier. To calculate the strain on the membrane, the following hypotheses are considered: 1) having a uniform plate thickness with small deflection, 2) an infinite rigidity of the body around the membrane with a perfect embedding, 3) a perfect elastic behavior and a negligible mass of gage/protection. When the sensor is subjected to a certain pressure p on its upper surface, the resultant radial and tangential strains (ε_r and ε_t successively) are written in (eq. 3.2a 3.2b). E is the Young modulus, ν is the Poisson ratio, t is the active thickness, r is the radius and x is the distance from the plate center to the edge. At the plate center, a positive and equal radial and tangential strains are obtained. For $0 < x < r$, the radial strain decreases more rapidly than the tangential one. However, for $x = r$ a negative radial strain with a double magnitude of its value at the center is reached whereas a zero tangential strain is observed as shown in, (Figure 3.28(a)). Therefore, a diaphragm pattern called $N2K - 06 - S066H - 350\Omega$ with 6.35 mm in diameter ($r=3.175$ mm) is selected having two radial gages at its outer part and two tangential gages at its central part, (Figure 3.28(b)). For a full bridge configuration the sensor resultant deformation is obtained by applying (eq. 3.2c). Experimentally, the output of the Wheatstone bridge V_0 is measured between the middle nodes of the two voltage dividers (eq. 3.3a). When $R_1/R_2 = R_4/R_3$, the voltage output V_0 is zero and the bridge is in balance. A change in the resistance of any bridge leg leads to a nonzero output voltage. Since the diaphragm is built on four gages seeking high stability, a full Wheatstone bridge is used, (Figure 3.28(c)). The

strain is calculated using (eq. 3.3b) where $G=1000$ mv/v is the gain used to amplify the signal, $V_{Ex}=2.5$ V is the excitation voltage, $K=2$ the gage factor and $\Delta S_{measured}$ is the output signal.

$$\varepsilon_r = \frac{3 * p * (1 - \nu^2)}{8 * E * t^2} * (r^2 - 3x^2) \quad (3.2a)$$

$$\varepsilon_t = \frac{3 * p * (1 - \nu^2)}{8 * E * t^2} * (r^2 - x^2) \quad (3.2b)$$

$$\epsilon = 2[\varepsilon_r^{edge} - \varepsilon_t^{center}] \quad (3.2c)$$

$$V_0 = \frac{R_3}{R_3 + R_4} - \frac{R_2}{R_1 + R_2} \quad (3.3a)$$

$$\varepsilon = \left(\frac{2}{V_{Ex}KG(1 + \nu)} \right) \Delta S_{measured} \quad (3.3b)$$

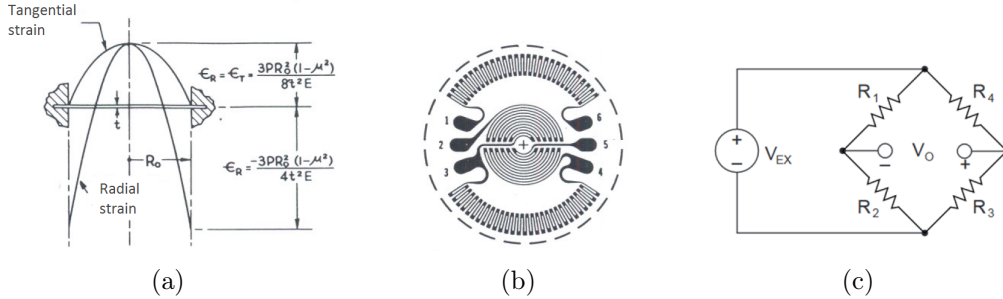


Figure 3.28: Diaphragm pattern (a) strains distribution for a clamped membrane (b) radial and tangential gages overview (c) full bridge configuration

3.3.3.1 Numerical application

Sensor deformation is validated by comparing the simulation results with the analytical model referring to (eq. 3.2a, eq. 3.2b and eq. 3.2c) where the radial and tangential strains are estimated (table 3.7). The magnitude of the pressure p is set equal to 200 MPa. The distance x is equal to zero and 3.175 mm (gage radius), t is equal to 4.5 mm and r is equal to 11.5 mm. A steel membrane is considered with $E=210$ GPa and ν equal to 0.3. The resultant numerical strain is affected by the boundary condition, when the number of the constrained nodes decreases the value

of the total strain becomes closer to the one of the analytical model.

r (mm)	P (MPa)	Analytical model		Numerical simulation			
				All nodes		Half nodes	
		ε_r	ε_t	ε_r	ε_t	ε_r	ε_t
0	200	2122	2122	2020	2020	2350	2350
3.175		1637	1960	1380	1815	1840	2240
P (MPa)		ε					
0		0		0		0	
200		-970		-1280		-1020	

Table 3.7: Analytical and simulation results with the resultant gage strain ε in (μ_m/m)

3.3.3.2 Calibration test

Two calibration tests are performed under an hydrostatic loading at 200 MPa of confining pressure (table 3.8). Unlike the first configuration (sec. 3.2) only normal set of the cap/aluminum cylindrical specimen can be used in this test due to the sensor shape and gage placement. The hydrostatic type sensor is replaced by the *s2* membrane sensor, (Figure 3.29). Unfortunately the mechanical effect was not tested for this type of gage. Calibration test results are gathered in (Figure 3.30) where the confining pressure is plotted versus the diaphragm deformation. A linear behavior is observed for both tests with a slight difference at the end. Experimental results are also compared with the numerical simulation curves. The sensor behavior is higher than the numerical curve with only half nodes fixed and lower than the numerical curve with all nodes fixed. We can consider that if the mechanical effect test was done, the sensor experimental curve will be corrected and then meet the half nodes fixed condition.

Test Name	Position	p_c (MPa)
Calib-5	normal	200
Calib-6	normal	200

Table 3.8: Details of calibration test using the diaphragm pattern

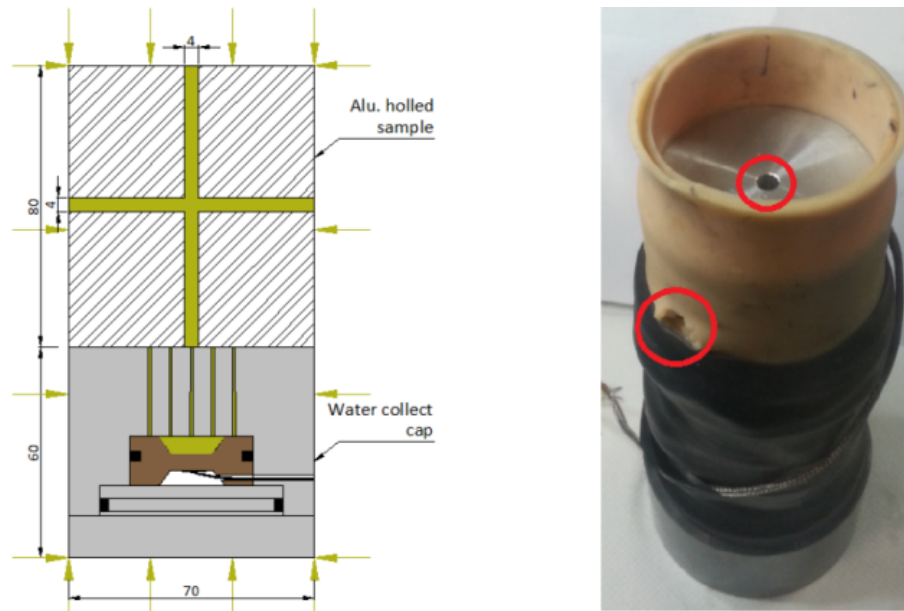


Figure 3.29: Membrane type sensor: normal calibration test (left): design (right): real picture

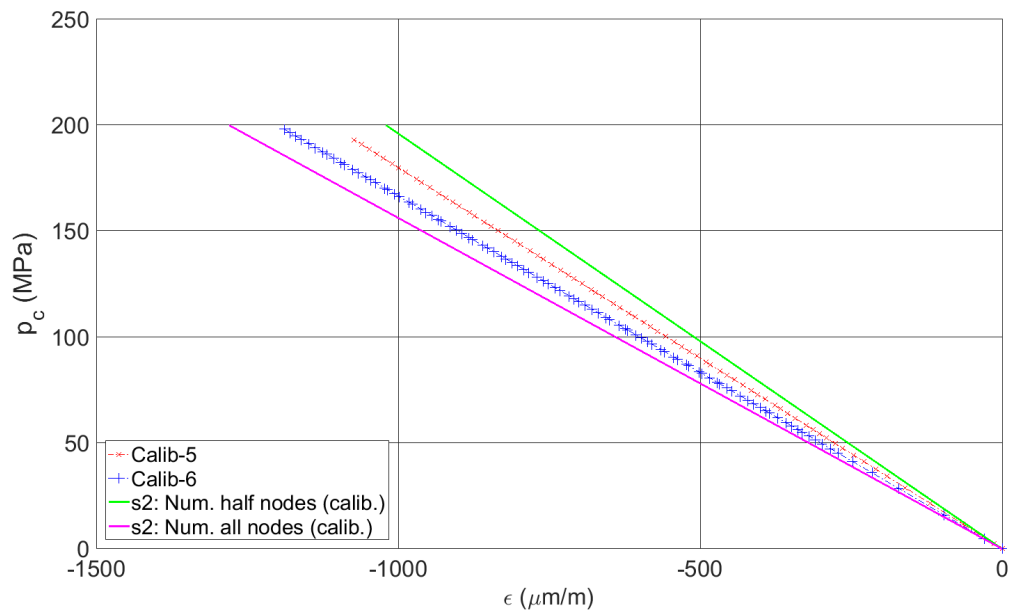


Figure 3.30: Calibration test results using the membrane sensor equipped with a diaphragm pattern: confining pressure vs. strain sensor

3.3.4 Quarter bridge: single gage

The sensor equipped with the diaphragm is then used to measure concrete pore pressure, three tests on a full saturated concrete samples are conducted but unfortunately no data acquisition was possible. In spite of all precaution and protection taken into account during preparation, connection wires have been cut and gage detachment has occurred as it is shown in (Figure 3.31). In consequence, the diaphragm gage is replaced by an available single gage having a circular support which forms a quarter Wheatstone bridge connected to the Giga DAS. This gage is placed at the center sensor where the highest strain is recorded and an epoxy is applied on its top seeking for system measurement protection as shown respectively in (Figure 3.32).



Figure 3.31: Lost of diaphragm pattern: (left) wires cut (right) gage detached



Figure 3.32: Single radial gage: (left) support and cosse gluing with wires welding (right) gage protection

3.3.4.1 Calibration test

A new calibration test is required on the membrane equipped with the single gage so that the slope of the strain-pressure curve is measured again. The same set of sample/cap explained in (sec. 3.3.3.2) is used. In addition, the mechanical effect

of the cap on the sensor is experimentally measured using a solid aluminum sample where only the outer side of the system is subjected to confining pressure as illustrated in (Figure 3.33). Tests details are shown in (table 3.9). The experimental set-up for this test is easier since no saturation of cap cavity is required. The total strain ϵ_t is considered to be the sum of two sub strain representing both tests (eq. 3.4a). The K_p slope is identified by performing a calibration test and the K_d slope is determined by performing the mechanical effect test, (eq. 3.4b).

$$\epsilon_t = K_d^{-1} * p_c + K_p^{-1} * p_i \quad (3.4a)$$

$$\epsilon_t = \begin{cases} K_d^{-1} * p_c & ; \text{if } p_c \neq 0 \text{ } p_i = 0 \\ (K_d^{-1} + K_p^{-1}) * p = K * p & ; \text{if } p_i = p_c = p \neq 0 \end{cases} \quad (3.4b)$$

Test name	Purpose	Position	p_c (MPa)	Slope K (GPa)
Calib-7	Calibration	normal	200	$K_p = 73.5$
ME-8	Mechanical effect	normal	200	$K_d = -573.1$
Resultant	—	—	200	$K = 84.3$

Table 3.9: Tests description performed on the membrane sensor using a single gage

Figure 3.34 depicts the results of the calibration and mechanical effect tests where the applied pressure is plotted versus the strain sensor at its central part. The experimental results are also compared with the numerical simulations shown in (Figure 3.24) detailed in (sec. 3.3.1.3). Experimentally, the mechanical effect test result (ME-8) causes a negative strain and it starts from the beginning of the test unlikely to the numerical simulation curves. The calibration test (Calib-7) response is larger than the numerical curves but once corrected by applying (eq. 3.4b), the resultant curve superposes with the half nodes numerical curve. This result reveals that in practice the sensor upper and lower surfaces are not totally constrained. However, during the interstitial pore pressure measurement test, the total deformation of the sensor ϵ_t , the applied confinement p , K_d and K_p are known and thus the pore pressure is calculated using (eq. 3.5).

$$p_i = \left(\epsilon_t - \frac{p_c}{K_d} \right) * K_p \quad (3.5)$$

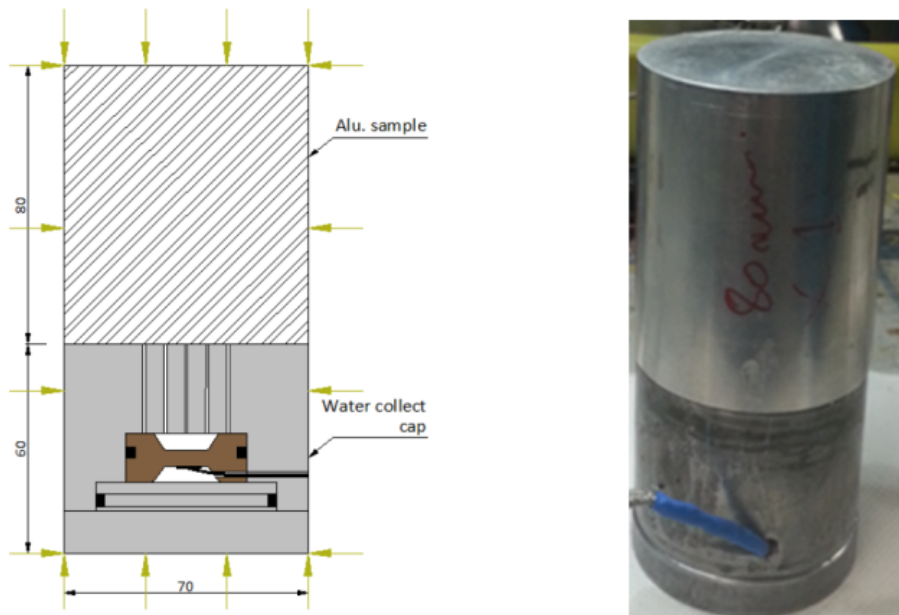


Figure 3.33: Membrane type sensor: principal of the mechanical effect (left): design (right): real picture

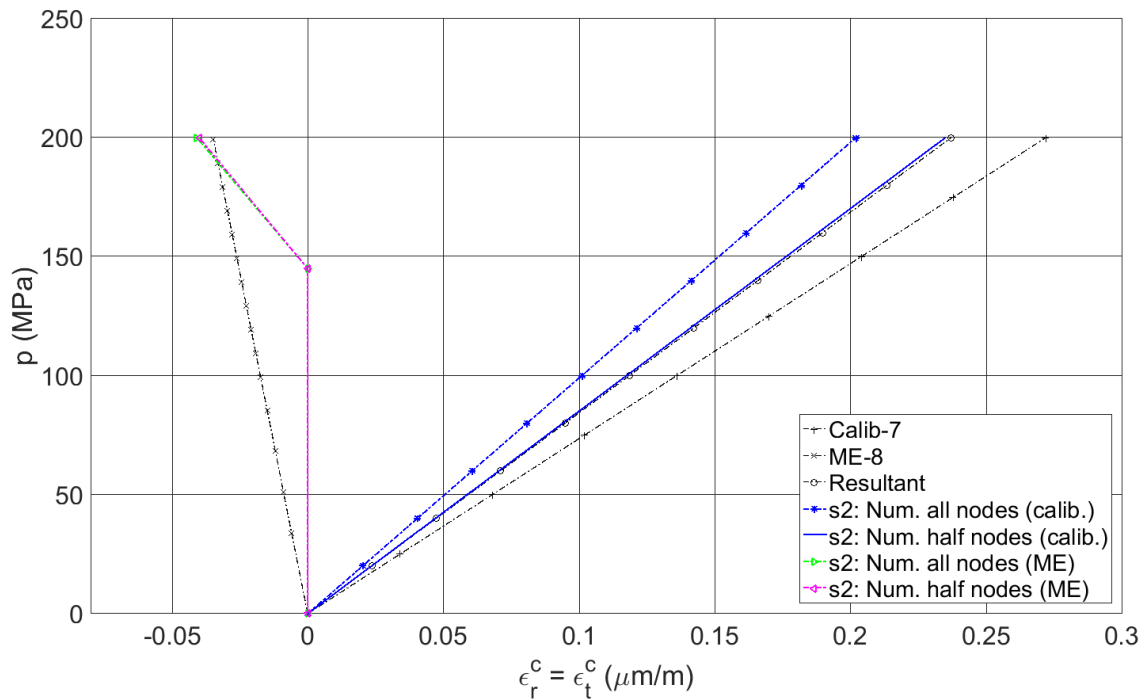


Figure 3.34: Experimental results of calibration test compared with the numerical calculations during a hydrostatic test

3.3.4.2 Interstitial pore pressure measurement in concrete samples

Hydrostatic test on a saturated concrete is performed at 300 MPa of confining pressure in order to measure the interstitial concrete pore pressure as described in (table 3.10) and plotted in (Figure 3.35). The represented pore pressure curve is divided into three phases: the first one corresponds to a null pore pressure in which the sensor is not yet deformed by the pressurized water (from 0 to 30 MPa of confinement). The second phase (from 30 to 150 MPa of confinement) where the pore pressure starts to increase rapidly where the free water inside the concrete exhibits a pressure. The third phase (from 150 to 300 MPa of confinement) where the pore pressure continues in increasing but linearly to reach a maximum value of 200 MPa.

Test name	Concrete	p_c (MPa)	Δt (min)	Interrupted	$p_{i,max}$ (MPa)
$p_i - 10$	R30A7	300	5	Non	196

Table 3.10: Pore pressure test description using the single gage

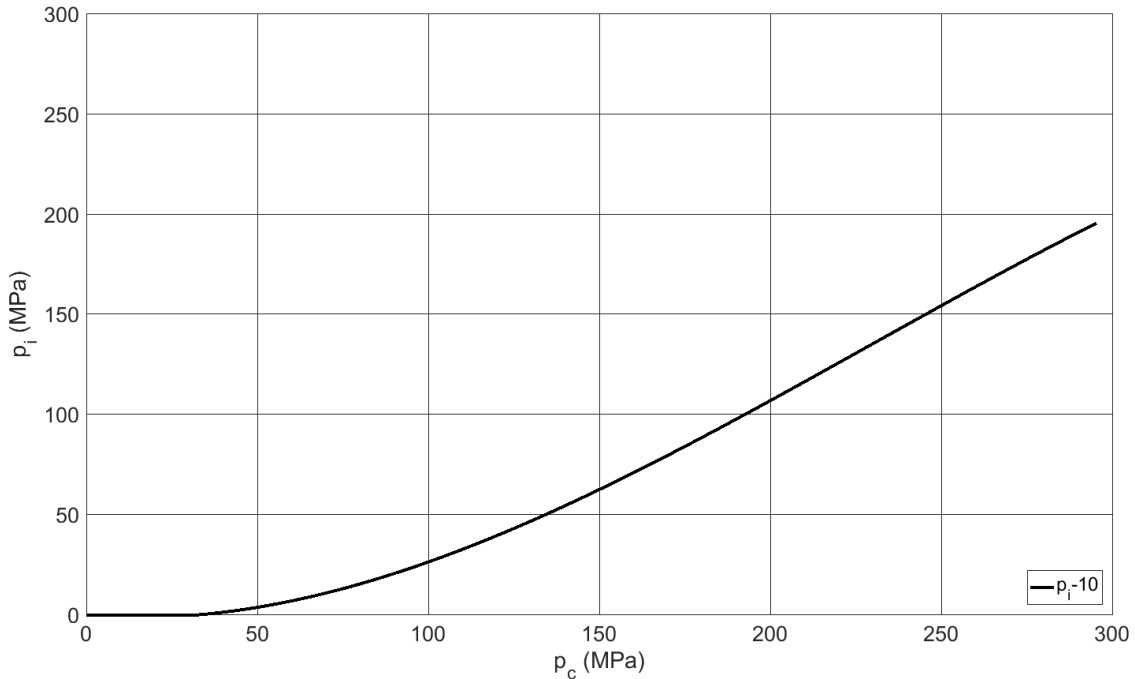


Figure 3.35: Pore pressure result on R30A7 concrete: pore pressure vs. confining pressure

3.4 Comparison between the hydrostatic and the membrane type sensor

Two main differences are observed between the two sensors. First, the gage is fully protected by using the membrane sensor since it is placed on its back face and not in contact with any fluid. Second, the gage signal output is amplified by a factor of 2.6 while comparing sensor sensitivity (sec. 3.3.1.3) and (sec. 3.2.4) presented in (Figure 3.36). It is also clear that the membrane sensor has proved its capability to register higher strain even at low and intermediate confining pressure.

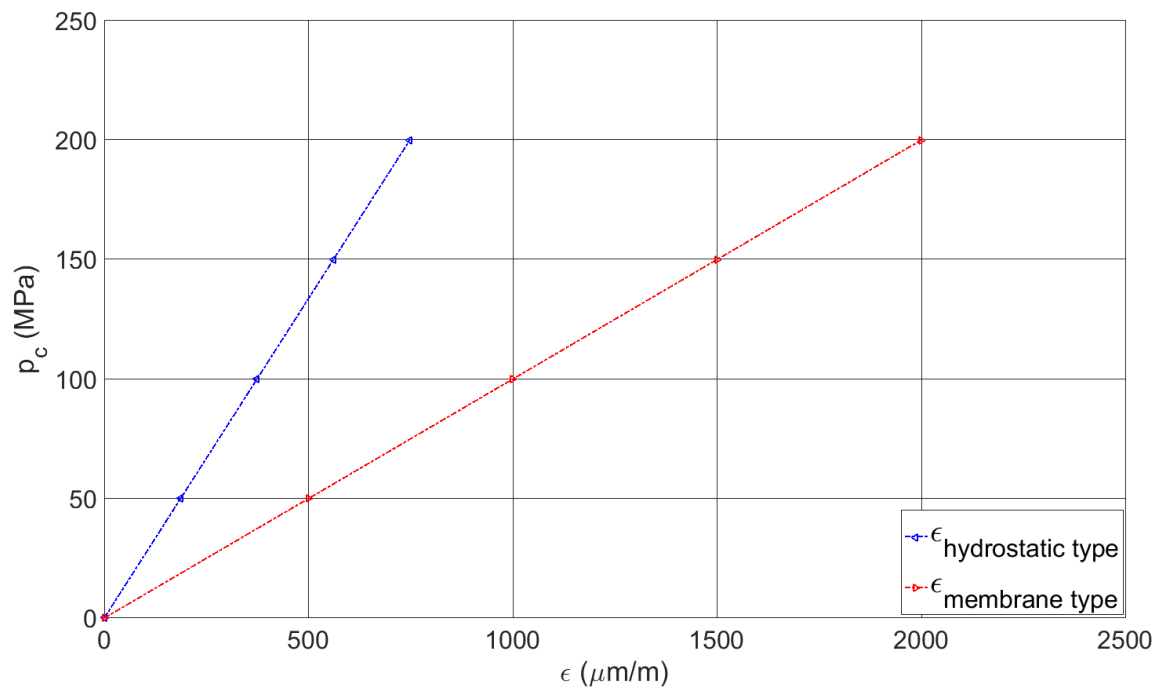


Figure 3.36: Comparison between the hydrostatic type and membrane sensor deformations: applied pressure vs. strain

3.5 New concept for pore pressure measurement

Since the performance of the used drainage system hangs on the method applied for assembly protection, a new device aiming to measure the pore pressure is proposed (Figure 3.37). Several problems at the sealing, gage and wires levels have been faced during the calibration and pore pressure measurement test while using the two sensors

configuration. These problems require a considerable effort to be solved. Therefore, the new technic has been designed and prepared to get ride from these inconveniences. The proposed water collecting cap is composed of two parts: the first one is the plug (cap upper part) which is moved to the top where micro-holes are executed directly on it. A threaded hole is also driven on the plug dedicated to saturate the cap free space, the hole can be closed by means of screw before the test. The sensitivity of the cap is linked to the thickness e of the second lower cap part. This thickness could be determined by means of numerical modeling in which, the effect of pore pressure acting on the cap inner side and the confining pressure acting on the outer side are considered. A deformable gage can be glued on the outer wall of 14 mm in height so that the whole system works as a flexible membrane (Figure 3.38). This solution requires a normal protection of the gage and wires system.

However, this concept was not completely validated by means of calibration and pore pressure tests due to technical problems on the Giga press.

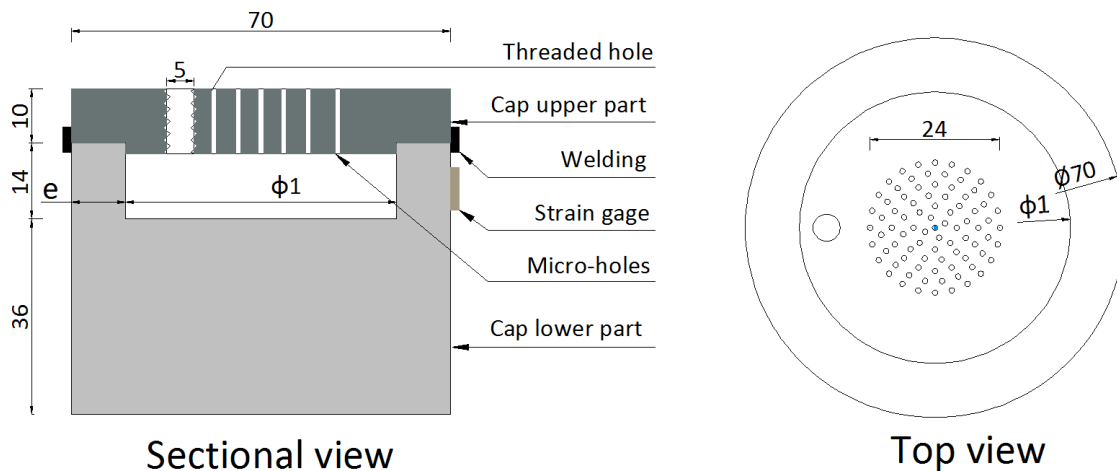


Figure 3.37: Design of pore pressure water collecting cap working on the membrane effect: (left) sectional view with a micro-holed cap equipped with a threaded hole, cap lower part, strain gage position (right) top view of the cap upper part



Figure 3.38: Water collecting cap with membrane effect: (left) real photo (right) gage application

3.6 Conclusion

In this chapter, two types of deformable sensor (hydrostatic and membrane types) were designed and calibrated in order to measure the interstitial pore pressure into saturated concrete samples. First sensors concept and modeling were illustrated. Second, the experimental procedure to prepare each test is detailed. From gage gluing, sensor and wires protection to the cap saturation and sample preparation. It has been shown that all these steps are important to guaranty the good performance of the system during pore pressure measurement of each test. A trial and error process is the best way to improve the measurement system despite the time it needs. Third, calibration test results was shown during which the known applied pressure loading is related to the sensor deformation. Both sensors calibration tests have led to promising results however the calibration of the membrane type sensor was more complicated. In addition, pore pressure preliminary results under hydrostatic loading were discussed. At the end, a new concept of pore pressure measurement where a water collecting cap working on the membrane effect concept is presented.

Result analysis of the interstitial pore pressure measurements

4.1 Introduction

This chapter presents the result analysis of the interstitial pore pressure measurement during hydrostatic test. A comparison between the hydrostatic and the membrane type sensors outcome is also illustrated. The effect of confining pressure and stress rate on the interstitial pore pressure measurement is displayed. The evolution of the interstitial pore pressure and the confining pressure with respect to the concrete volumetric strain is discussed at the end.

4.2 Interstitial pore pressure tests results

Table 4.1 summarizes all interstitial pore pressure tests that gave reliable results and which will be discussed in the following sections. The table includes the name of each test, the sensors used, the maximal measured pore pressure and the maximal concrete volumetric strain both correlated with the maximal confinement pressure. In addition, since the pore pressure of tests 1 and 7 exhibits a plateau while the confining is still increasing, a real value of this latter with its corresponding volumetric strain are admitted. Tests 1 to 8 represents the results issued from the hydrostatic type sensor whereas test 10 represent the result issued from the membrane type sensor. The pore pressure measurement during test 4 was lost at almost 400 MPa of confinement so that this latter with the volumetric strain are corrected. The test 9 was eliminated since it

failed at a low confinement pressure (approximately 150 MPa) and the the volumetric deformation of test 1 and 10 are not represented since they were not measured.

Test name	Sensor type	p_c (MPa)	p_i (MPa)	ϵ_v (%)	$p_{c,real}$ (MPa)	$\epsilon_{v,real}$ (%)
$p_i - 1$	Hydrostatic	600	120	—	280	—
$p_i - 2$	Hydrostatic	500	360	5,8	500	5,8
$p_i - 3$	Hydrostatic	500	360	7,1	500	7,1
$p_i - 4$	Hydrostatic	500	355	5,6	400	5
$p_i - 5$	Hydrostatic	500	425	6,5	500	6,5
$p_i - 6$	Hydrostatic	500	200	5,1	500	5,1
$p_i - 7$	Hydrostatic	500	210	7,3	290	5,3
$p_i - 8$	Hydrostatic	500	250	7,6	500	7,6
$p_i - 10$	Membrane	300	196	—	300	—

Table 4.1: Summary of the pore pressure measurement tests for both sensors type

4.3 Influence of confinement pressure

Results of both configurations are gathered in (Figure 4.1) where the concrete interstitial pore pressure is plotted versus the applied confining pressure during an hydrostatic loading. First, all the results can be divided into two trends of curves: an increase of the pore pressure slope with respect to the confining pressure (e.g: exponential trend) such as tests 2, 4, 5 and 10 and a linear increase of the pore pressure like tests 3, 6, 7 and 8 with respect to the confinement. Second, results of the hydrostatic type sensor are not all the same. In fact, tests 2, 3, 4 and 5 have a higher pore pressure values than the tests 6 and 8. For example at 400 and 500 MPa of confinement, a pore pressure ranging between 200-355 MPa and 250-420 MPa is respectively observed. In addition, test 5 and test 8 reserve the higher and lower interstitial pore pressure reaching 420 and 250 MPa consecutively at 500 MPa of confining pressure. Third, test 10 which derives from the membrane sensor seems to give the same trend of curve as the test 4. As it has been explained in chapter 3, the membrane sensor amplifies the signal which means that it is more sensitive to the pressure. In addition, the cap free space when the membrane sensor is used is lower than the space when the hydrostatic sensor is used. This means that even a small variation of the water volume could be detected by the membrane sensor. At the end, results discrepancy between all tests may be due to pores size distribution into concrete which may differs from sample to another and could affect the water transport within the pores.

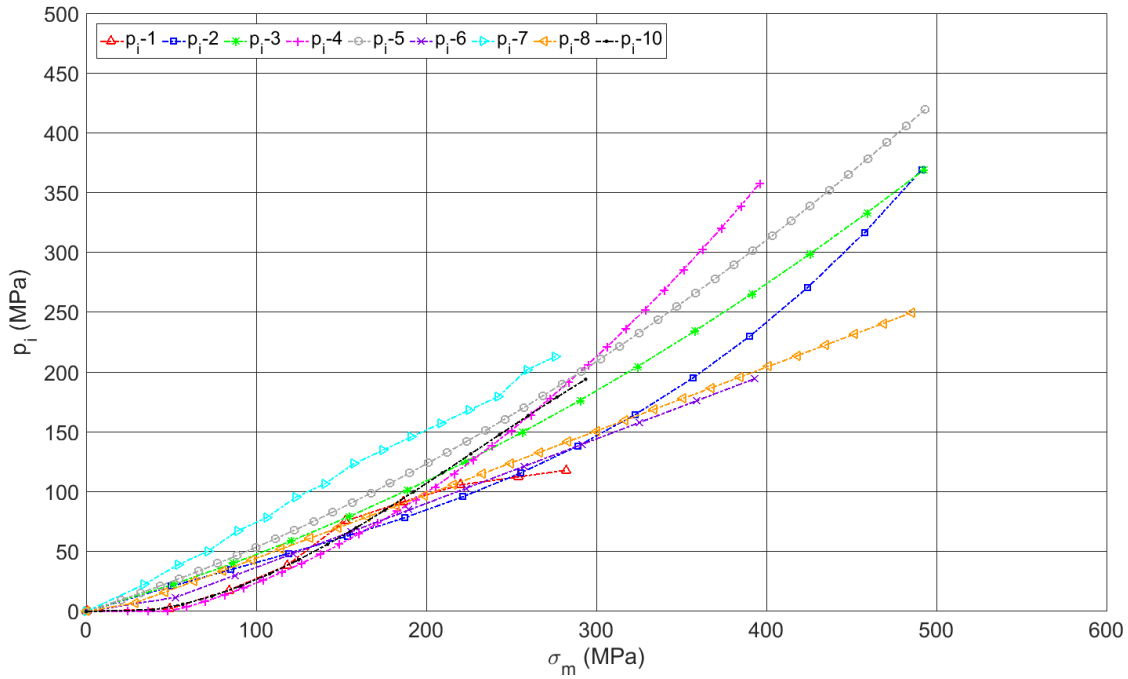


Figure 4.1: Results of interstitial pore pressure measurement on the R30A7 concrete using the hydrostatic and the membrane type sensors: p_i vs. σ_m

Concrete interstitial pore pressure evolution at the beginning of the confinement is shown in (Figure 4.2). The slopes of tests 2, 3, 5 and 7 are stiffer than the slopes of tests 1, 4, 6, 8 and 10. However these tests (2, 3, 5 and 7) are marked by an instantaneous increase of pore pressure once the hydrostatic loading pressure is applied. This behavior means that the concrete samples are fully saturated (S_r equal to 100%). On the contrary tests 1, 4 and 10 tests have conserved a null pore pressure for approximately 30 to 50 MPa of confinement which would perhaps mean that these samples are not perfectly saturated (S_r below 100%). In this case, the free water inside pores is not pressurized before the free air porosity is closed. In addition, this null pore pressure behavior could be due also to the late response of the hydrostatic or membrane type sensor when the water inside the concrete sample is pressurized. Figure 4.3 shows the mean curve of the interstitial pore pressure tests and the maximum pore pressure with its corresponding confinement for each test (taken from table 4.1: real values). At low confinement pressure (between 0 to 100 MPa), a linear increase of the pore pressure with respect to the confinement is observed where a slope equal to 0.5 can be attributed. Then a fast increase of the measured pore pressure is observed once the confinement exceeds 200 MPa where the slope becomes equal to 0.8.

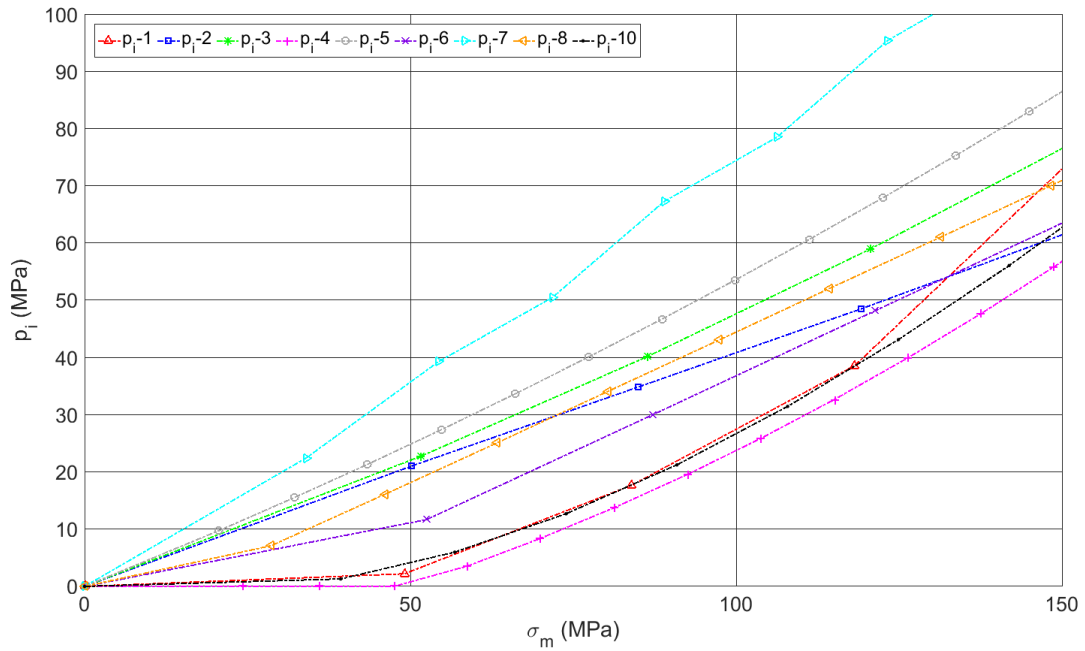


Figure 4.2: Results of interstitial pore pressure measurement on the reference concrete. Zoom on the first part of the plot: p_i vs. σ_m

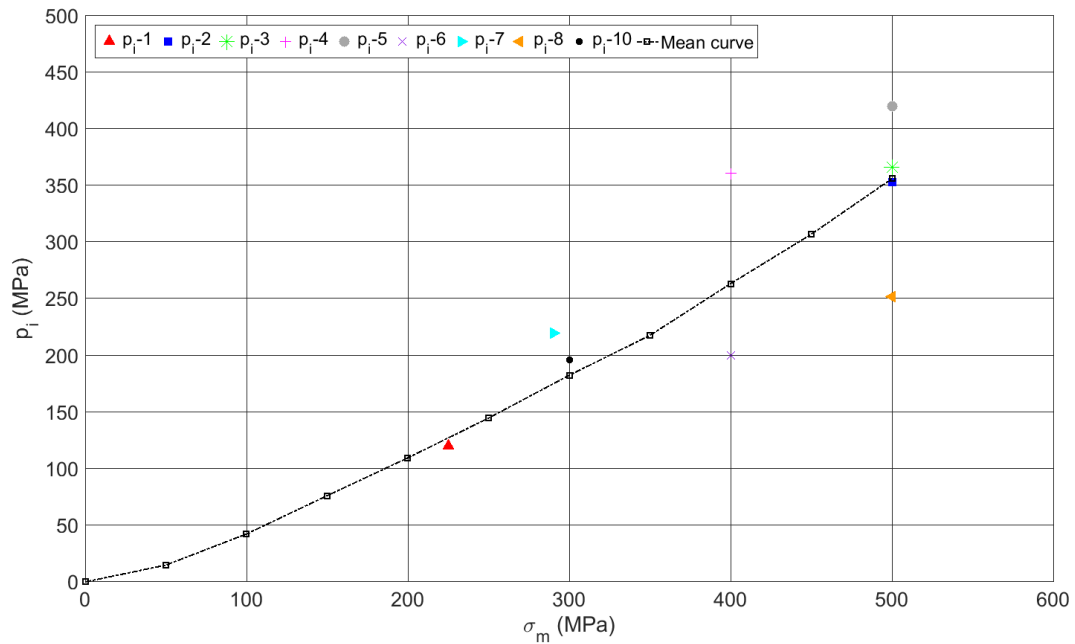


Figure 4.3: Mean value of the interstitial pore pressure measurement and maximum pore pressure reached for each test with respect to the applied confining pressure

4.4 Influence of loading rate

The Giga press allows to control the increase rate of the pressure inside the confining cell. The press allows a maximal pressure rate equal to 1000bar/min, (e.g: 500 MPa of confinement in 5 minutes which means 1.67 MPa/s). In this study, three types of stress rate have been implemented in order to study their effect on concrete pore pressure measurement. The rising time of the confining pressure t_c is set equal to 5, 10 and 15 min., which corresponds to a loading rate of 1.67, 0.83 and 0.55 MPa/s respectively.

The influence of loading rate on concrete pore pressure measurement is illustrated in (Figure 4.4). The tests 4 and 5 are performed at the lowest loading rate and show a higher pore pressure while comparing them to the tests 1, 2, 3 and 6 with highest loading rate. However, this analysis is not applicable to the test 7 which has the higher pore pressure. In addition, for intermediate loading rate such as test 8 and 10, their pore pressure measurement represent the lower and higher value at the end of each tests. Thus the loading rate effect is not easy to show from these results.

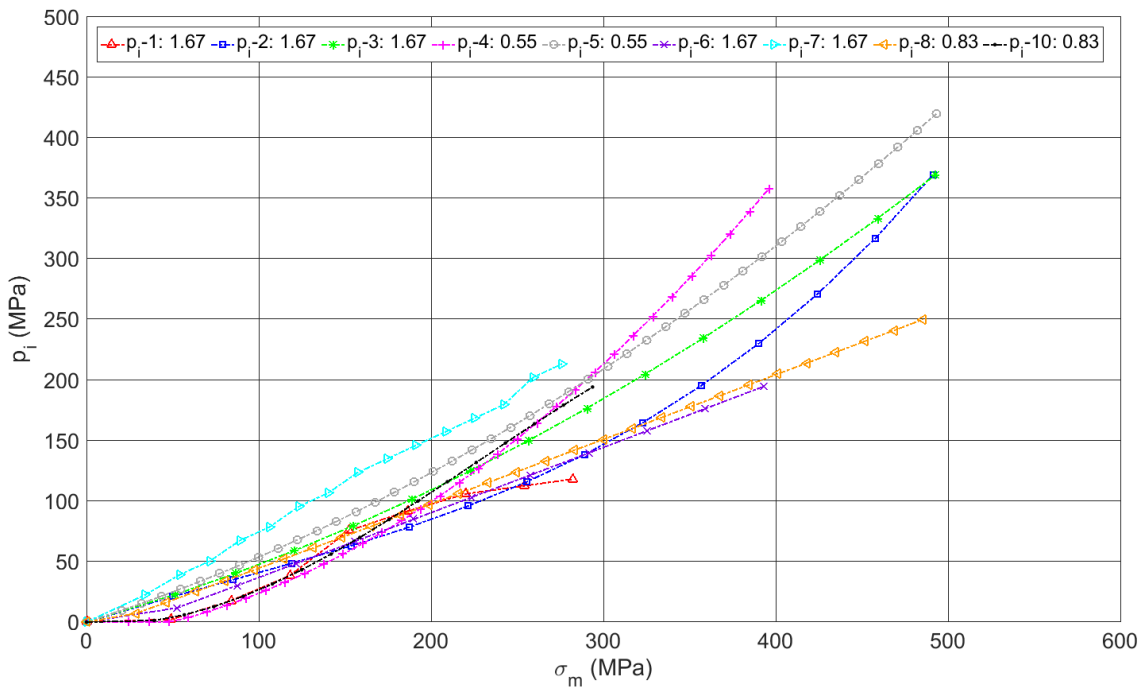


Figure 4.4: Results of interstitial pore pressure measurement with different loading rates on the reference concrete using the hydrostatic type and the membrane type sensor: p_i vs. σ_m

4.5 Concrete volumetric behavior

Concrete volumetric behavior while measuring the interstitial pore pressure are gathered in (Figure 4.5) and compared with the volumetric behavior of both dried and saturated reference concrete (R30A7) performed by [Vu, 2007]. The volumetric deformation is estimated based on the LVDT response, assuming an isotropic behavior, as explained in chapter 2. In general, concrete volumetric behavior passes through three phases. First, an elastic phase until approximately 40 MPa. Second, where the slope of the volumetric deformation starts to decrease due to the matrix damage, the compaction phase is then observed until 400 MPa of confinement. Third, concrete hardening phase where the slope of the volumetric deformation increases again. The last phase is more pronounced for saturated samples than for dried one as it was concluded from Vu's work.

It is observed that tests 2, 4, and 6 have approximately the same behavior of the two reference concrete tests (except for the beginning of the test 4) until the end of the loading part. The Curves of these tests are below the ones of the reference concrete for intermediate confinement (100 to 300 MPa) and then coincides with the saturated concrete curve at the end. The tests 3, 5 and 7 are characterized by a small elastic phase and an early beginning of the compaction phase which leads to a decrease in the slope of each curves. This behavior leads to a higher volumetric deformation from the same confinement than the referenced concretes. In contrast, the test 8 shows a typical elastic behavior at the beginning (until 100 MPa) then a change in the slope which also decreases very fast. However, all curves retrieve the same slope as the saturated sample beyond 200 MPa of confinement where the consolidation phase starts. The loading rate effect is not so clear from these results.

Figure 4.6 shows the mean curve of the concrete volumetric behavior for all the tests compared with the behavior of the two reference concretes. At low confinement pressure (between 0 to 200 MPa), a linear increase of the confinement pressure with respect to the volumetric strain is observed, a slope equal to 5 GPa can be attributed. Then the concrete behavior becomes stiffer with a slope equal to 10.5 GPa.

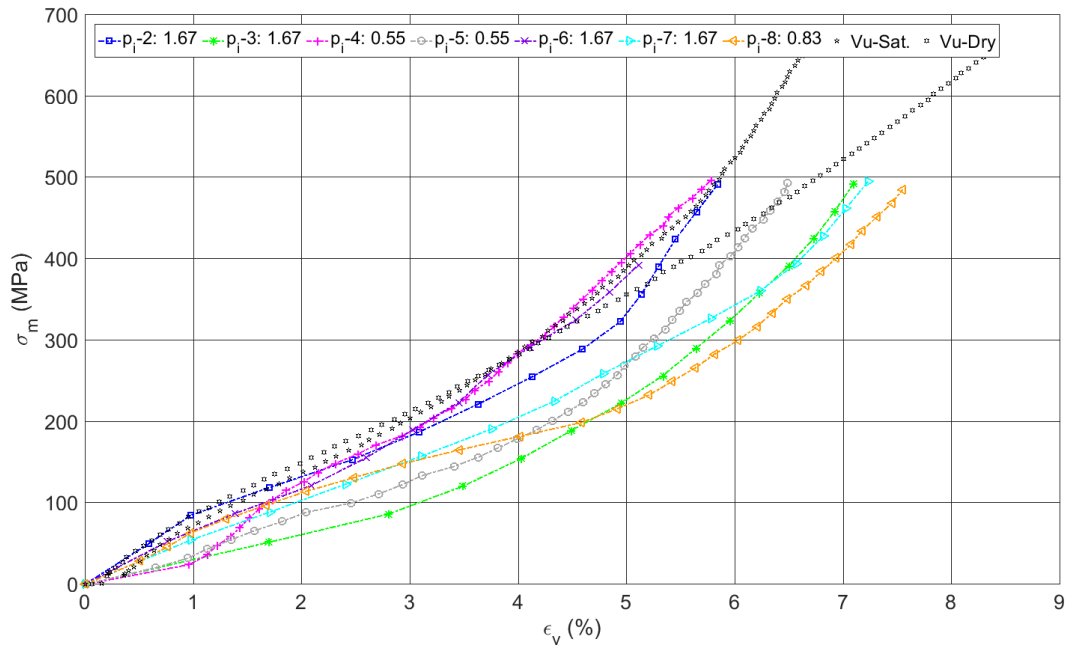


Figure 4.5: Volumetric behavior of concrete under hydrostatic loading during pore pressure measurements. Comparison with the two references concrete: pc vs. σ_m

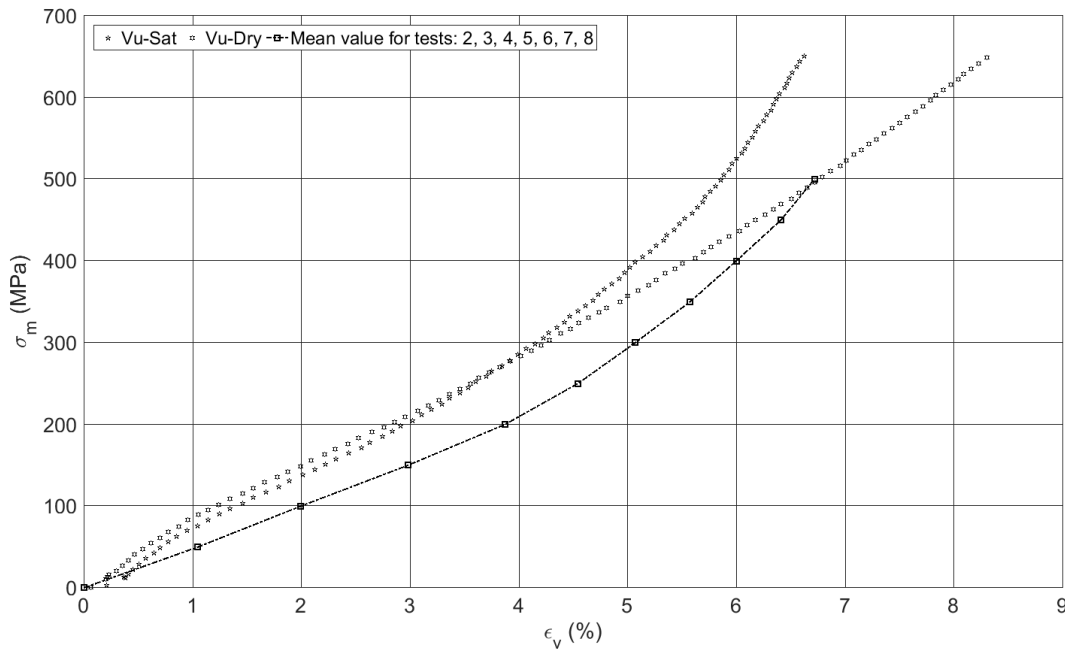


Figure 4.6: Mean volumetric behavior curve under hydrostatic loading during pore pressure measurements. Comparison with the two references concrete: pc vs. σ_m

In addition, the effect of concrete volumetric strain on the pore pressure evolution under high confining pressure is also investigated as shown in (Figure 4.7). A very low pore pressure is observed for the test 4 even though concrete has deformed under hydrostatic compression. Two separate effects may influence this result: the first one is linked to the experiment itself where either a late response of the hydrostatic sensor has occurred or the free cap space was not very well saturated. The second effect may be linked to the fact that the pore pressure increases when all the pores are completely closed and reveals that the concrete sample probably have a saturation ratio (S_r) lower than 100%. To make the analysis easier (Figure 4.8) depicts the mean value of the interstitial pore pressure versus the estimated concrete volumetric strain during pore pressure measurement. Maximum pore pressure with the corresponding volumetric strain for each test (taken from table 4.1: real values) are also presented. It is observed that at low volumetric strain ($\leq 5\%$) a linear increase of the pore pressure with respect to the volumetric strain appears where the slope is equal to 3 GPa. However for a volumetric strain ($\geq 5\%$), the curve changes in slope where the pore pressure increases more rapidly for a small variation of the volumetric strain with a value equal to 16 GPa. This behavior is attributed to the significant porosity closure developed during hydrostatic test at high confining pressure.

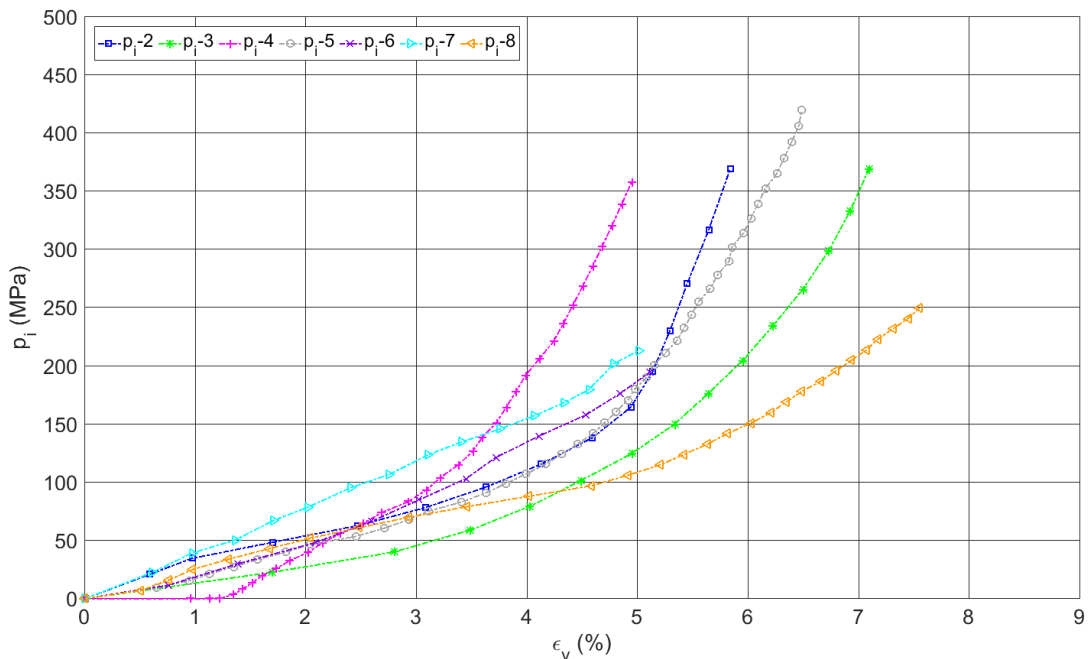


Figure 4.7: Pore pressure evolution with respect to concrete volumetric deformation

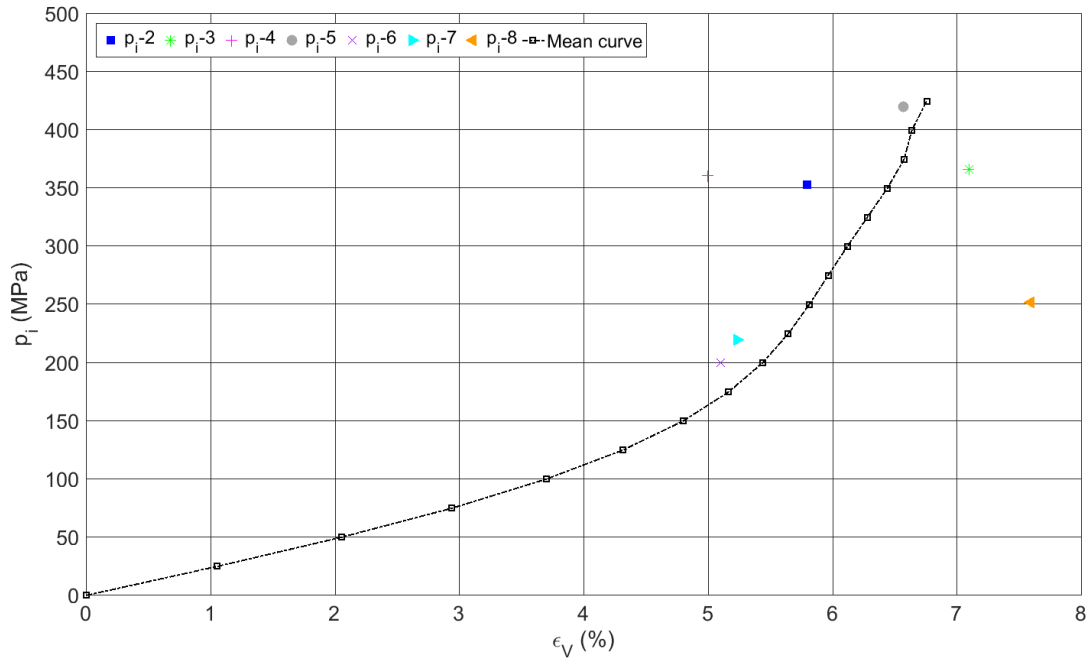


Figure 4.8: Mean value of the interstitial pore pressure measurement and maximum pore pressure reached for each test with respect to the volumetric strain

4.6 Conclusion

In this chapter the results of the interstitial pore pressure tests performed on the reference concrete using both sensors at high confinement pressure are compared. It has been shown that the pore pressure evolution with respect to the applied confinement passes through two phases: the first one where the pore pressure increases linearly with the confinement whereas the second one is marked by a change in the slope curve which become more stiffer. The effect of the loading rate on concrete pore pressure measurement was not pronounced and hard to explain for all the tests. Furthermore, the estimation of the concrete volumetric strain during pore pressure measurement permits the evaluation of the concrete volumetric behavior during pore pressure measurement. First, the mean stress versus volumetric strain curve shows that concrete volumetric behavior passes through three phases: the first phase where a very reduced elastic behavior is noticed comparing to the reference concrete. The second phase corresponds to a progressive damage of the cementitious matrix attributed to a gradual decrease of the tangent modulus. The last stage begins near 200 MPa of confinement, marked by an inflexion point, where the tangential stiffness increases again and the

slope of the curve becomes parallel to the reference saturated concrete one. At the end, the pore pressure variation with respect to the volumetric strain was evaluated and gives almost the same trend of curve. Two important stages is highlighted: a linear increase of the pore pressure with the volumetric strain followed by a faster increase of the pore pressure for higher volumetric strain. The slope of the mean curve becomes stiffer beyond approximately 200 MPa of confinement (compaction point) for which the porosity is considerably closed.

Modeling of concrete interstitial pore pressure

5.1 Introduction

This chapter presents a model which objective is to simulate the increase of concrete interstitial pore pressure due to the porosity closure mechanism observed under high confining pressure. The model takes into account the influence of the saturation ratio and the initial porosity of concrete. Results of the model are compared with the measured interstitial pore pressure and concrete volumetric behavior results performed experimentally.

5.2 Effective stress concept in PRM model

The aim of the coupled PRM (Pontiroli, Rouquand and Mazars) model is to simulate concrete structures subjected to impacts [Rouquand, 2002], [Pontiroli et al., 2004] [Malecot, 2009]. It is the resultant of two coupled model which make possible to simulate the response of the material according to many paths of stress. The first one is the damage model allowing the description of concrete degradation mechanism at low stress. The second model is an elastoplastic model called (KST) [Krieg, 2002], [Swenson and Taylor, 1983] developed to reproduce the behavior of concrete under high confinement. In order to take into account the effect of water on the material behavior, the effect stress concept has been introduced into the model. To do so, two types of approaches have been proposed. The first approach is the mixing law

(serial or parallel model) where the second approach is the poro-mechanics theory. Therefore, these approaches make possible to simulate the volumetric behavior of the partially saturated material and permit to relate the volumetric deformation to the mean stress and water pressure. The material is then decomposed into a solid phase, voids filled with air and voids filled with water. As long as the porosity filled with air has not been completely closed, the material is not consolidated and the water does not intervene in the behavior of the material, whatever the type of calculation used. Beyond the point of consolidation, the presence of water is taken into account for both the volumetric behavior (Figure 5.1: left) and the limit state curve (Figure 5.1: right).

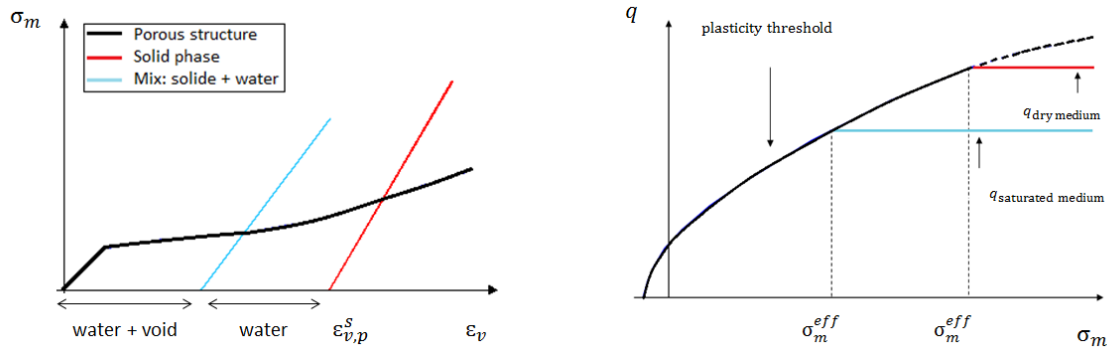


Figure 5.1: PRM coupled model with saturation ratio effect on the concrete: (a) volumetric behavior (b) deviatoric stress

5.2.1 Serial and parallel approach

To characterize the behavior of a porous medium at its homogenized scale, the mixing law approach (serial or parallel model) can be used, (Figure 5.2). According to the medium properties at the microscopic scale, the interaction between the solid and the fluid phases are taken into account by means of rheological models. In the serial type model, the average stress in the solid (s) phase is assumed equal to the pressure in the liquid (w) phase. In this case the total deformation is considered equal to the sum of the deformations of the solid phase and of the liquid phase, (eq. 5.1a 5.1b). In the parallel model, the volumetric deformation of the solid structure and of the voids are assumed identical. The total stress is then calculated by adding the stress of the solid structure to the pore pressure, (eq. 5.2a 5.2b).

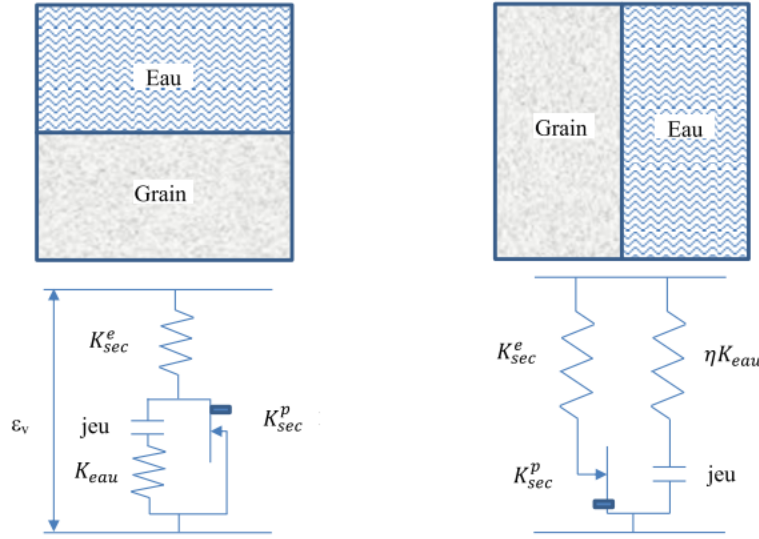


Figure 5.2: Schematic representation of: (left) serial (right) parallel model [Vu, 2013]

Serial model equations:

$$\sigma_{m(mix)} = \sigma_{m(s)} = p_w \quad (5.1a)$$

$$\epsilon_v = \epsilon_v^s + \epsilon_v^w \quad (5.1b)$$

Parallel model equations: η is the ratio of water over solid volume and $\epsilon_{v,p}^s$ is the plastic volumetric strain at the consolidation state.

$$\sigma_{m(mix)} = \sigma_{m(s)} + \eta p_w (\epsilon_v - \epsilon_{v,p}^s) \quad (5.2a)$$

$$\epsilon_v = \epsilon_v^s = \epsilon_v^w \quad (5.2b)$$

The mixture model was evaluated by [Malecot, 2009]. The volumetric behavior of the serial and parallel models were compared with the experimental data obtained experimentally on the R30A7 concrete (for different saturation ratio) subjected to hydrostatic loading, (Figure 5.3). It is worth to note that the volumetric behavior curve of the dried concrete is not represented since it was considered as an input of the model and thus it will coincide with the experimental curve. Results show that the assumption used to calculate the total stress in the parallel model is more realistic since the consolidation point (which corresponds to a total porosity closure) of this model is close with the change of slope observed in the experiments. However, the model reveals two important limitations: first, it overestimates the increase of

the concrete bulk modulus after being consolidated due to the presence of water. Second, the elastic behavior after the consolidation phase is quasi-linear which is not experimentally. Therefore, a new poro-mechanical model is proposed as a second approach to take into account the presence of free water inside pores (sec. 5.2.2).

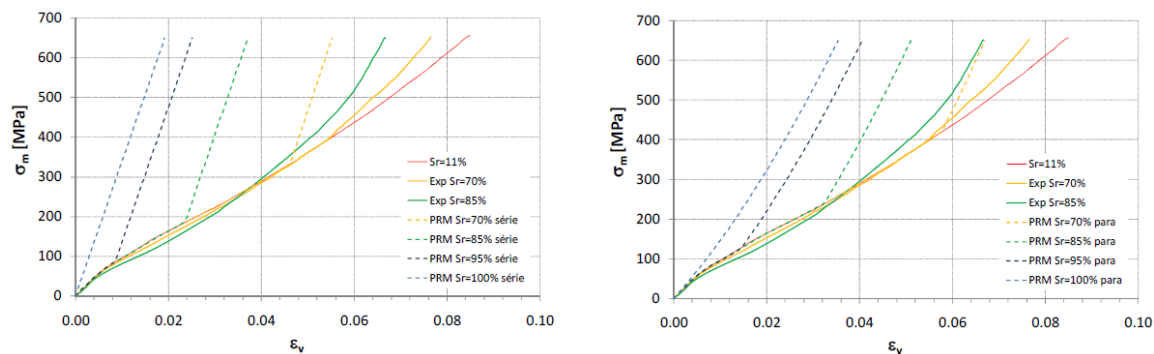


Figure 5.3: Concrete behavior for different saturation ratios under hydrostatic loading: mean stress vs. volumetric strain. Results comparison with PRM (a) serial (b) parallel model, [Malecot, 2009]

5.2.2 Poro-mechanical approach

The poro-mechanics theory considers that the porous medium is composed of two continuous media: a deformable skeleton and a fluid filling the voids of this latter [Coussy, 1995], (Figure 5.4). The concept of the effective stress is introduced to separate the fluid pressure in the total stress calculation. The total mean stress is supposed to be the sum of the mean stress transmitted by the skeleton at the macroscopic scale and the water pore pressure corrected by the Biot's coefficient b , (eq. 5.3a). The pore pressure p is calculated based on the Mie-Grüneisen equation of pressure state (eq. 5.3b) where C_0 and ρ_0 are the speed sound and density of water respectively. Γ_0 and s are two Mie-Grüneisen coefficients. E_m is the internal energy per unit mass. In the model, this energy is assumed to be negligible for normal water temperature and atmospheric pressure.

In the context of the poro-elasticity theory, it was shown by [Coussy, 1995] that the pore pressure can be linked, to the volumetric strain at the homogenized scale ϵ_v by means of (eq. 5.4a) where: M the Biot's modulus (eq. 5.4b), b is the Biot's coefficients (eq. 5.4c) and ν_f is the relative fluid mass flow (neglected since the ratio between the water volume inside the cap and the specimen is infinitesimal). K , K_s and K_w represent the bulk modulus of the drained material, of the consolidated

skeleton and of the fluid respectively [Heukamp et al., 2001]. The Biot's coefficient can be evaluated depending on each case. For example if $K \ll K_s$, it means that the material is very soft and a very slight contact between grains occurs. In this case b is close to 1 and the Terzaghi effective stress concept is recovered. In contrast, when $K \simeq K_s$ the porosity tends to zero leading to a zero b coefficient (as considered in the parallel model). Finally, the ratio between K/K_s , can be estimated using a homogenization of the drained porous medium as stated by [Kendall et al., 1983], (eq. 5.4c).

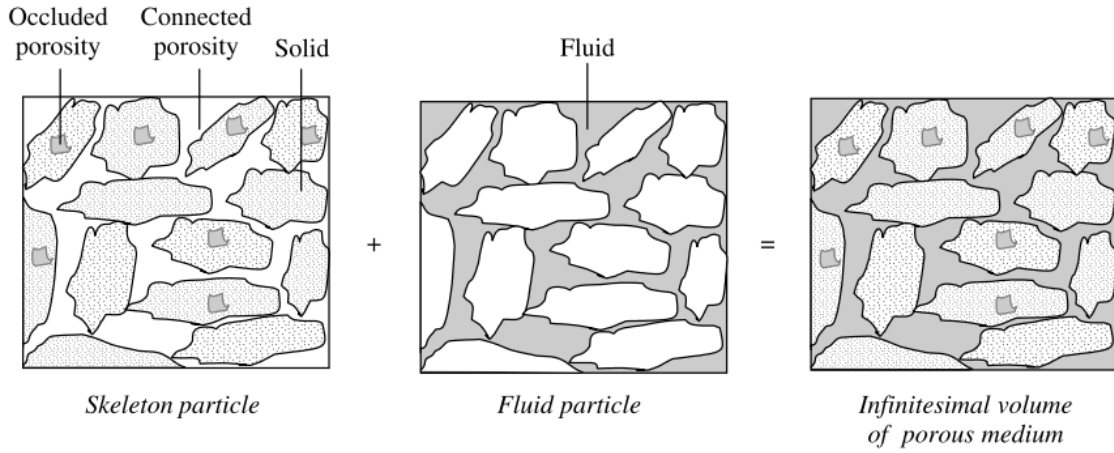


Figure 5.4: The porous medium matrix as the superposition of two continuous media: a skeleton particle and a fluid particle, [Coussy, 1995]

$$\sigma_{m(mix)} = \sigma_{m(s)} + b p_w \quad (5.3a)$$

$$p_w = \frac{\rho_0 C_0^2 (\epsilon_v - \epsilon_{v,p}^s)}{(1 - s(\epsilon_v - \epsilon_{v,p}^s))^2} \left(1 - \frac{\Gamma_0 (\epsilon_v - \epsilon_{v,p}^s)}{2}\right) + \Gamma_0 \rho_0 E_m \quad (5.3b)$$

$$p_w = M(b\epsilon_v + \nu_f) \quad (5.4a)$$

$$M = \frac{b - \phi}{K_s} + \frac{\phi}{K_w} \quad (5.4b)$$

$$b = 1 - \frac{K}{K_s} = 1 - (1 - \phi)^3 \quad (5.4c)$$

5.3 Concrete behavior under high confining level

The closure of porosity which happens when concrete is subjected to hydrostatic loading at high confining pressure has been experimentally investigated by many authors, [Burlion et al., 1998], [Gabet et al., 2008] [Vu, 2007], [Zingg, 2013]. Under such kind of solicitation, the concrete compaction is observed leading to two phenomena which appear simultaneously: the damage of the material structure and the porosity closing. The cohesive structure of concrete disappears progressively and is replaced by a granular stacking. Using the same concept, many complementary hypotheses are needed in order to apply the poro-mechanical model for pore pressure prediction modeling.

1) Concrete physical properties:

At its initial state two fundamental properties of the reference (R30A7) concrete are supposed to be known: its initial porosity ϕ_0 which is assumed to be between 12 to 15% (depending on the used measurement method) and its saturation ratio S_r which represents the percentage of voids filled by water identified before each test.

2) Hydrostatic behavior of drained concrete under loading:

It is assumed that the concrete volumetric behavior of the model during the loading phase coincides with the experimental one of the dry concrete curve (S_r equal to 11%). However, this behavior is not elastic but we assume in the following that the poro-mechanics equations remain valid.

3) Hydrostatic behavior of the skeleton:

In poro-mechanics, the skeleton represents the solid phase (aggregates and cement hydrate) which is assumed to remain elastic during the loading phase. The skeleton modulus of compressibility K_s is set equal to 38 GPa. It is estimated by using the homogenizing technic between the compressibility modulus of aggregates which is equal to 39 GPa according to [Camborde, 1999] on the one side and of hydrates which is equal to 33 GPa according to [Ulm et al., 2004] on the other side considering their respective volume in the concrete composition.

4) Hydrostatic behavior of drained concrete under unloading:

To reproduce the phenomenon of concrete porosity closure, it is necessary to model the evolution of the elastic properties of the drained concrete during the loading phase with respect to the mean stress. Referring to the hydrostatic cyclic test performed by [Poinard et al., 2012] on the R30A7 concrete (Figure 5.5: left), the variation of the volumetric bulk modulus K_v is less important at the beginning of the loading phase and increases as the consolidation process occurs, (Figure 5.5: right).

Thus, in order to evaluate the evolution of the porosity closure, it is suggested first that the concrete volumetric bulk modulus K_v evolves according to an exponential law (eq. 5.5a). Second, the total strain is split into an elastic and a plastic strains (eq. 5.5b). The elastic strain is identified by admitting that it derives from the skeleton mean stress and the elastic bulk modulus considering only the solid phase of concrete. Therefore, the plastic strain is calculated by subtracting the elastic strain from the total one (eq. 5.5c). Third, the variation of the porosity is estimated to be equal to the variation of the plastic strain since the latter corresponds to the beginning of the concrete compaction phase (eq. 5.5d). Finally, the rate of closed pores ϵ_ϕ is quantified in function of the porosity variation and the initial porosity (eq. 5.5e) and thus the rate of pores which still opened (F_r) can be deduced (eq. 5.5f).

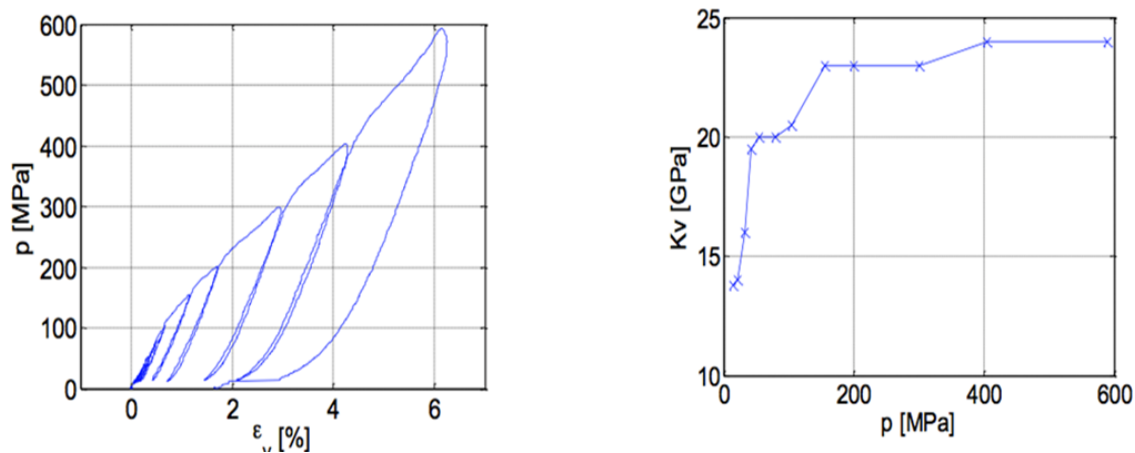


Figure 5.5: Cyclic hydrostatic test up to 600 MPa on the R30A7 concrete: (left) volumetric behavior (right) evolution of concrete bulk modulus [Poinard et al., 2012]

$$K_v = K_s - (K_s - K) \exp\left(\frac{\sigma_{m,(dry)}^s}{\sigma_1}\right) \quad (5.5a)$$

$$\epsilon_{v,(dry)}^t = \epsilon_v^e + \epsilon_v^p \quad (5.5b)$$

$$\epsilon_v^p = \epsilon_{v,(dry)}^t - \frac{\sigma_{m,(dry)}^s}{K_v} (1 - \phi_0) \quad (5.5c)$$

$$\Delta\phi = -\Delta\epsilon_v^p \quad (5.5d)$$

$$\epsilon_\phi = \frac{\Delta\phi}{\phi_0} \quad (5.5e)$$

$$F_r = 1 - \epsilon_\phi \quad (5.5f)$$

Table 5.1 shows the parameters used to estimate the porosity closure. As explained in the previous section, the skeleton mean stress and the total volumetric concrete strain are taken from an hydrostatic test conducted during [Vu, 2007] thesis on a dried R30A7 concrete. In the same way, the elastic properties E , ν are used to quantify the initial elastic bulk modulus K . The consolidation pressure of concrete σ_1 , which is an adjustment parameter, is supposed to be equal to 1 GPa. The influence of initial concrete porosity on the pores closure process is studied by applying the proposed equations (using a Matlab code) for two initial porosities value (ϕ_0 equal to 12 and 15%). On the one side, the concrete bulk modulus, which is independent of the initial porosity, underestimates the experimental value, (Figure 5.6: left). On the other side, the percentage of pores which still opened is higher for high initial porosity at a given deformation, this means that the model is also capable to link the initial porosity with the rate of closed pores, (Figure 5.6: right).

Parameters	Designation	Unit	Value
$\sigma_{m,(dry)}^s$	mean stress of dry concrete	MPa	tabular
$\epsilon_{v,(dry)}^t$	volumetric strain of dry concrete	%	tabular
σ_1	consolidation mean stress	GPa	1
K_s	skeleton bulk modulus (consolidated)	GPa	38
K	initial elastic bulk modulus	GPa	12.5
ϕ_0	initial porosity	%	12-15

Table 5.1: Parameters for porosity closure estimation

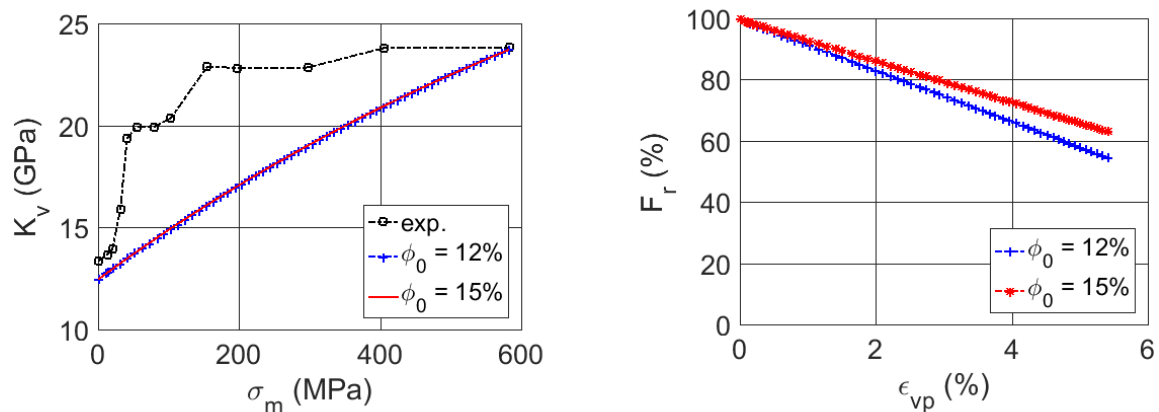


Figure 5.6: Evolution of the concrete bulk modulus: (left) comparison between the model and the experimental curve (right) opened pores with respect to the plastic strain for both initial porosities

5.4 Evaluation of the pore pressure

Geo-materials such as concrete can be decomposed into a solid phase and a void phase which is filled whether by air or by water. When the medium is subjected to a mechanical loading such as hydrostatic compression, the skeleton takes up the force first and the liquid phase remains at its initial state while the volumetric strain is low. As the loading increases, the skeleton starts to deform inducing cracks appearance around the pores. The reduction of the void volume leads to an irreversible strain. As long as there is air void (free of water), the interstitial pore pressure does not change much because of the air compressibility that is very high. But when all the air voids disappear (porosity collapse), the water enters in contact with the skeleton. From this moment any additional deformation is applied to both phases. Thus, the increase in interstitial pore pressure corresponds to a simultaneous compression of skeleton and water. However, a small decrease in volume results in a significant increase in pressure. Figure 5.1 reflects this mechanism which is adapted in the model. For example the consolidation of a partially saturated medium occurs faster than a dry one.

The analytical model developed in this study aiming to reproduce the evolution of the pore pressure is divided into two major steps. The first step aims to calculate the pore pressure, (eq. 5.6a to 5.6e). At the beginning, the variation of the porosity already estimated thanks to (eq. 5.5d) is used to update the current porosity state (eq. 5.6a) which is implemented by its turn to determine the Biot's coefficient (eq.

5.6b). Then the current porosity closure is calculated with respect to the porosity variation and the actual one (eq. 5.6c). If the porosity closure is lower than the air ratio inside the sample (case of partially saturated concrete) the water strain remains null otherwise it is activated (eq. 5.6d). The first step is ended by the calculation of the pore pressure based on the Mie-Grüneisen formula (eq. 5.6e).

$$\phi = \phi_0 + \Delta\phi \quad (5.6a)$$

$$b = 1 - (1 - \phi^3) \quad (5.6b)$$

$$\epsilon_\phi = \frac{\Delta\phi}{\phi} \quad (5.6c)$$

$$\epsilon_v^w = \begin{cases} 0 & \text{if } \epsilon_\phi \leq 1 - S_r \\ \epsilon_\phi & \text{if } \epsilon_\phi > 1 - S_r \end{cases} \quad (5.6d)$$

$$p_w = \frac{\rho_0 C_0^2 \epsilon_v^w}{(1 - s\epsilon_v^w)^2} \left(1 - \frac{\gamma_0 \epsilon_v^w}{2}\right) \quad (5.6e)$$

$$K_w = \begin{cases} 0 & \text{if } p_w = 0 \\ \Delta p_w / \Delta \epsilon_v^w & \text{if } p_w \neq 0 \end{cases} \quad (5.6f)$$

$$M^{-1} = \frac{b - \phi}{K_s} - \frac{\phi}{K_w} \quad (5.6g)$$

$$\epsilon_v = \begin{cases} \epsilon_{v,(dry)}^t & \text{if } p_w = 0 \\ \epsilon_{v,p(dry)}^t + p_w / Mb & \text{if } p_w \neq 0 \end{cases} \quad (5.6h)$$

$$\sigma_m^t = \sigma_{m,(dry)}^s + bp_w \quad (5.6i)$$

The second step tends to determine the mean stress at the macroscopic scale, (eq. 5.6e to 5.6i). The water bulk modulus is the ratio of the pore pressure to the water volumetric strain and it is equal to zero when the pore pressure is null, (eq. 5.6f). After that, the Biot's modulus, which is already defined, is calculated, (eq. 5.6g). The concrete volumetric strain is supposed equal to the volumetric strain of the dry concrete if the pore pressure is null (condition 3). Otherwise it is calculated based on (eq. 5.6h) by adding the contribution of the pore pressure and the volumetric plastic strain of the dry concrete. This latter is defined once the pores are totally closed and thus it vary with respect to the saturation ratio (see Figure. 5.8). Finally the total mean stress, which is the sum of the mean stress of the skeleton phase at the dry state and the corrected pore pressure, is computed (eq. 5.6i). In order to converge, the

porosity variation is updated after each calculation step by assuming that it is equal to the difference between the estimated volumetric strain and the dry volumetric one. Table 5.2 presents the parameters used to estimate the volumetric strain and mean stress within the model.

Parameters	Designation	Unit	Value
ρ_0	water density	Kg/m ³	1000
s	Mie-Gruneisen coefficient	–	1.75
γ_0	Mie-Gruneisen coefficient	–	0.28
C_0	acoustic wave velocity	m/s	1500
K_{w_0}	initial water bulk modulus	GPa	2.733

Table 5.2: Parameters for pore pressure estimation

5.4.1 Influence of the initial porosity and saturation ratio

In order to study the effect of the initial porosity and of the saturation ratio, on the concrete pore pressure modeling and the resulting mean stress behavior, analytical calculations (using a Matlab code) have been conducted using the described model. The saturation ratio and the initial porosity are set as detailed in (table 5.3).

	Run 1	Run 2	Run 3	Run 4
S_r (%)	100	95	85	11
ϕ_0 (%)	12 - 15			

Table 5.3: Values of saturation ratios and initial porosities used in the modeling

Figure 5.7 presents a comparison of the analytical results for different saturation ratios and initial porosities. The pore pressure is plotted versus the applied mean stress (confinement pressure in case of an hydrostatic test). It is observed that, when the saturation ratio increases, the pore pressure increases. As explained before, the increase of confining pressure on pores is effective only when all the air voids are closed which is more pronounced for higher saturated concrete (e.g: 200 MPa of confinement is required to close all the pores for S_r equal to 85% against 100 MPa for S_r equal to 95%). Results also reveals that for the same saturation ratio, the higher the initial porosity is the lower the pore pressure is for a given mean stress. As it was shown before referring to (Figure 5.6: right), the rate of pores which still opened is more enhanced when the initial porosity is low, which means that high confinement

is needed to obtain the same pore pressure if the porosity is higher.

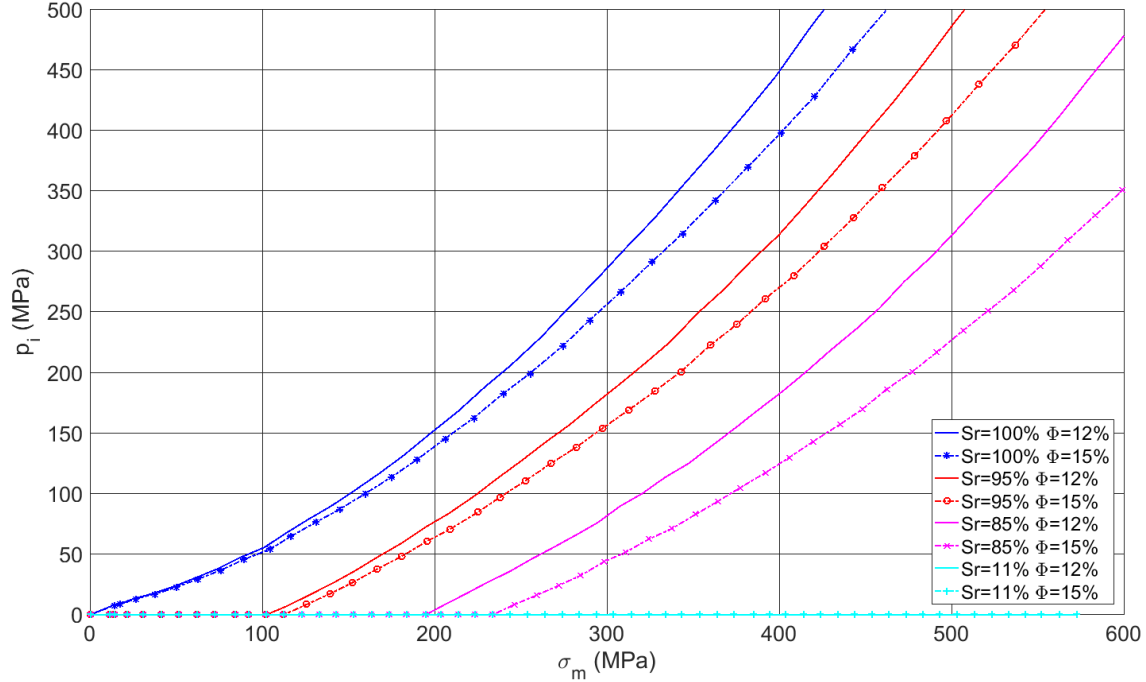


Figure 5.7: Concrete pore pressure modeling in concrete under hydrostatic loading: pore pressure vs. mean stress for different saturation ratios and initial porosities

Figure 5.8 shows a comparison between the analytical mean stress for different saturation ratios and initial porosities and the experimental results obtained for both dried and saturated concrete [Vu, 2007]. The model gives very good results for saturation degrees equal to 85 and 95%. For high saturation ratio, the consolidation point as well as the progressive increase of stiffness are well reproduced. The model significantly underestimates the deformations when the concrete is fully saturated. This is probably explained by the high sensitivity of the model to the saturation ratio. It is also observed that the effect of the initial porosity decreases when the saturation ratio decreases. The analytical dry curve coincides with the experimental one since the mean stress is considered as an input parameter.

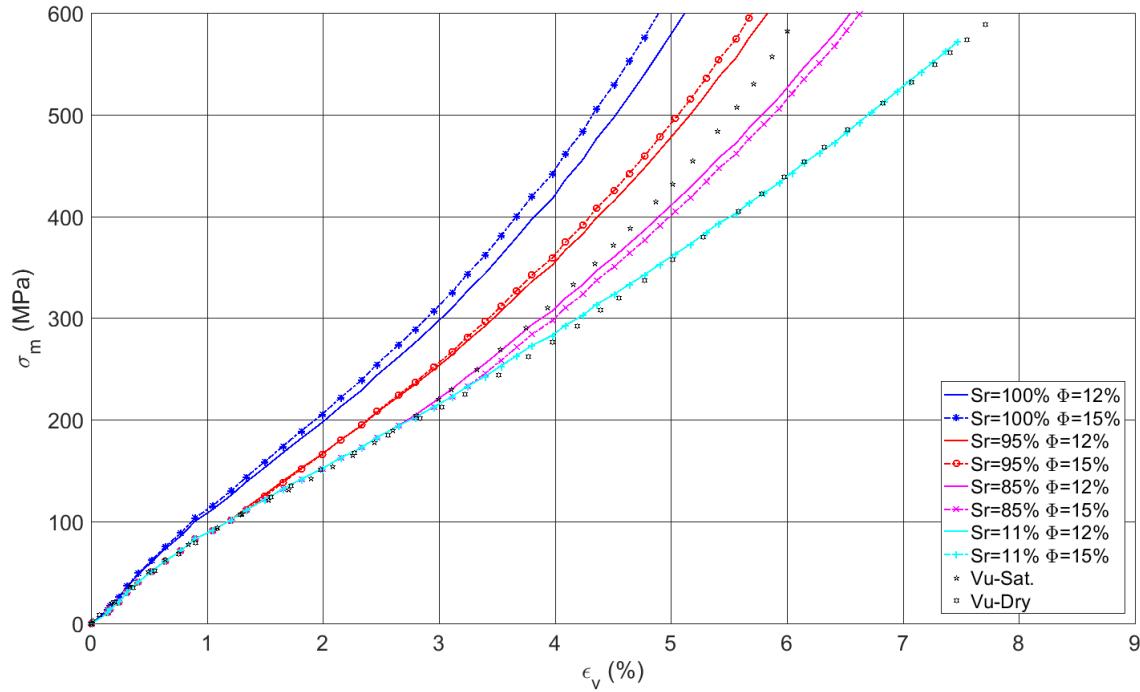


Figure 5.8: Concrete volumetric behavior modeling under hydrostatic pressure: mean stress vs. volumetric strain for different saturation ratios and initial porosity compared with the dry and saturated R30A7

5.5 Pore pressure comparison

Figure 5.9(a) shows a comparison between the numerical modeling curves (for high S_r equal to 100, 98 and 95 % and both initial porosities) and the resultant pore pressure measurement test with its range of variation with respect to the confinement. This latter is plotted versus the mean stress (hydrostatic pressure). Numerical estimation of the pore pressure for high saturation ratio (from 100 to 95 %) and both initial porosities display a great capability to cover experimental results. It is clear that the maximum range of the experimental curve lies very close to the analytical curve having a saturation ratio higher than 95%. It is also noticed that a better estimation of the pore pressure occurs at high initial porosity. A closer look on the results is exposed in, (Figure 5.9(b)). The analytical curve with 98% of saturation ratio estimates very good the minimum value of the experimental result where a very low pore pressure is recorded from 0 to 50 MPa of confinement. This result reveals the capability of the model to reproduce the behavior of a non saturated sample where the pore pressure is not measured until the pores closure.

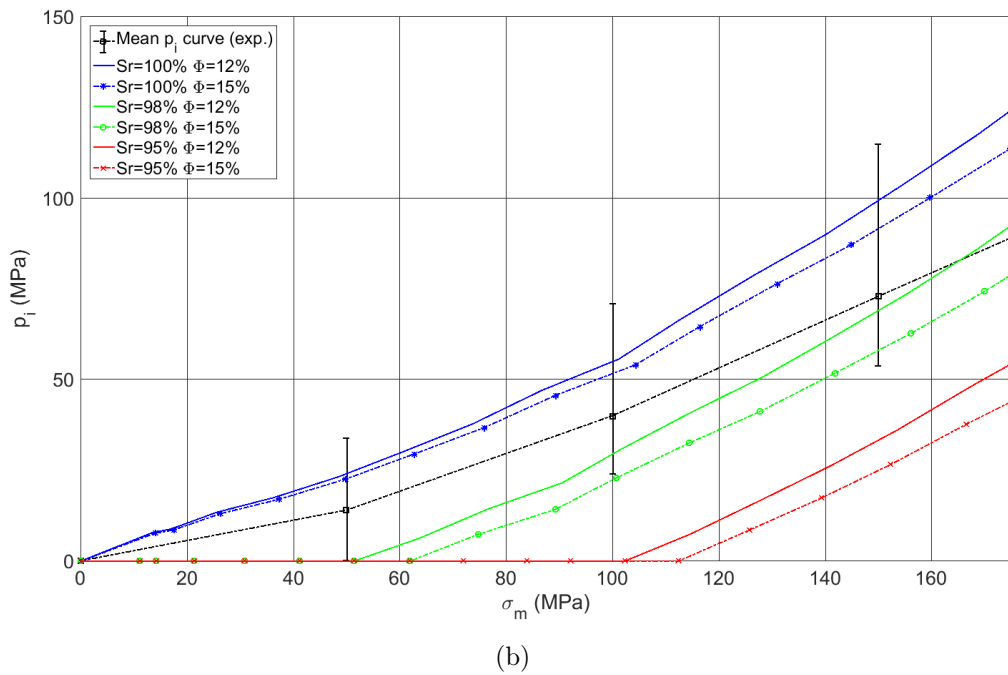
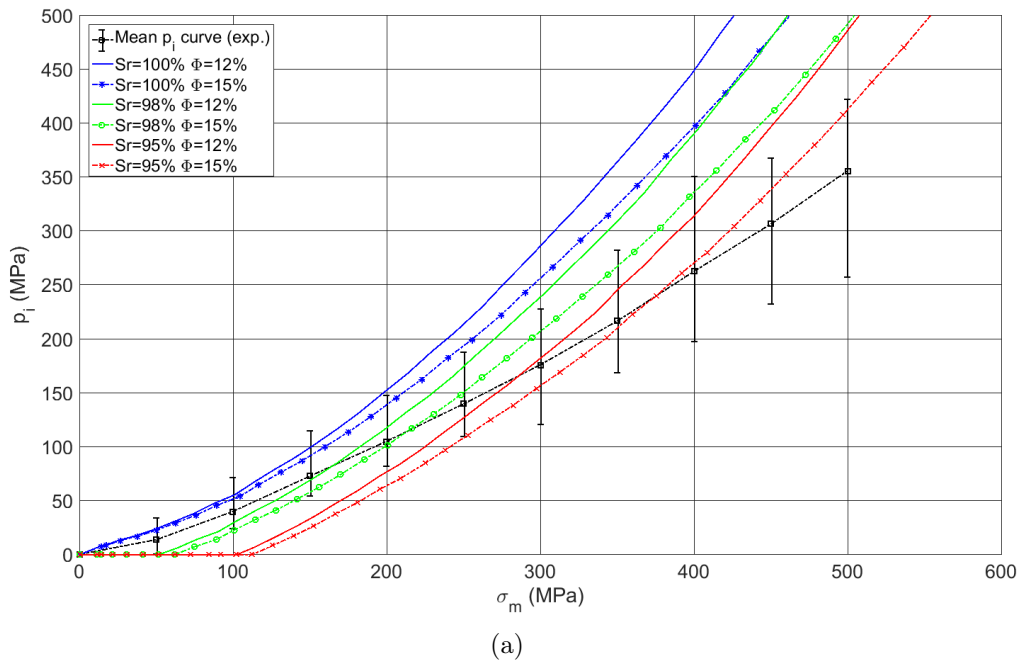


Figure 5.9: Concrete behavior under hydrostatic loading. Interstitial pore pressure vs. mean pressure: (a) experimental measurement with variation range and poro-mechanical modeling (b) zoom on the first part

Furthermore, Figure 5.10 depicts the pore pressure versus the volumetric strain of the poro-mechanical model curves compared with the experimental mean value with its range of variation. It is clear that the model overestimates the behavior of concrete for S_r higher than 98%, this is due to the high sensitivity of the volumetric strain to the saturation ratio. However, the model (for S_r equal to 95%) shows a promising results while comparing it with the minimum experimental curve.

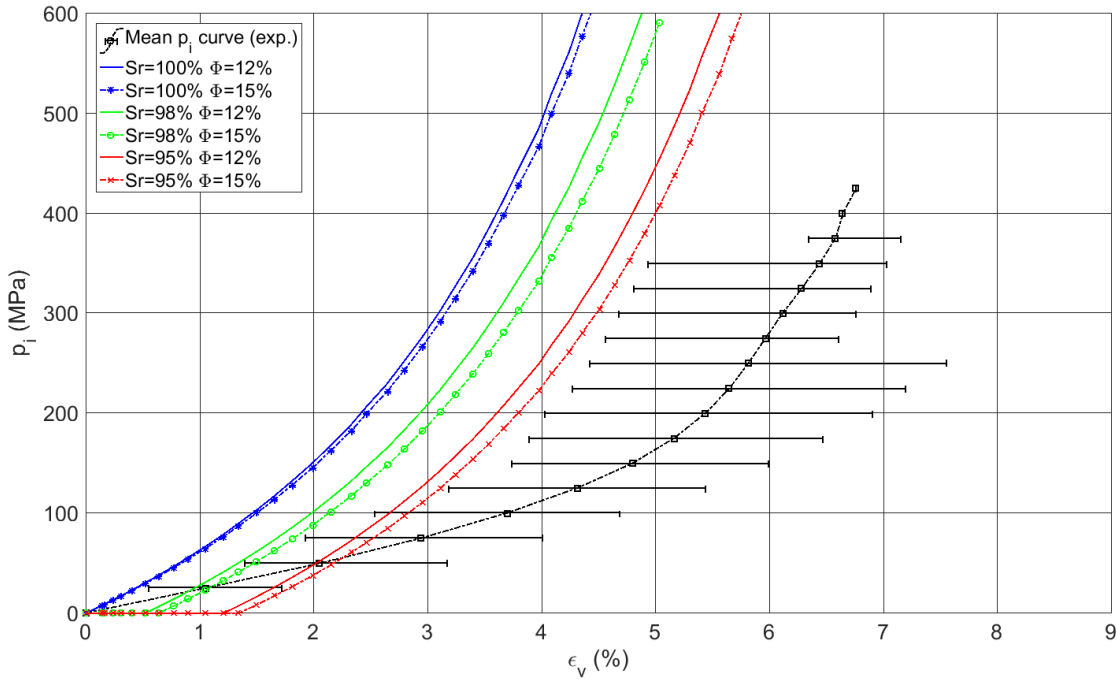


Figure 5.10: Concrete behavior under hydrostatic loading. Interstitial pore pressure vs. volumetric strain: experimental measurement with variation range and poro-mechanical modeling

5.6 Experimental identification of the Biot coefficient

The Biot's coefficient is identified referring to the experimental test results previously discussed in chapter 4. To take into account the effect of free water into concrete when pressurized, the poro-mechanical approach is also adapted. It assumes that the mechanics concepts in continuum mechanics are still valid at the macroscopic scale when the two phases (liquid + solid) overlap [Coussy, 1995]. Thus, it is assumed that the concrete mean stress at the saturated state is the sum of the concrete mean stress at the dried state and the contribution of water pressure corrected by the

Biot's coefficient b [Biot, 1941], [Biot, 1957], (eq. 5.7a). This coefficient is one of the most important parameter for coupling between mechanical variable such as stress or strain and the pore pressure [Zimmerman et al., 1957], [Zimmerman, 2000]. Based on the assumption made herein this coefficient could be estimated using (eq. 5.7b). Experimentally, these mean stresses are issued from tests performed under undrained condition carried out by [Vu, 2007] (e.g: $\sigma_{m,(sat)}^t$ for saturated sample and $\sigma_{m,(dry)}^s$ for dry one). They are displayed with the interstitial pore pressure resultant curve as shown in, (Figure 5.11).

$$\sigma_{m,(sat)}^t = \sigma_{m,(dry)}^s + b * p_w \quad (5.7a)$$

$$b = \frac{\sigma_{m,(sat)}^t - \sigma_{m,(dry)}^s}{p_w} \quad (5.7b)$$

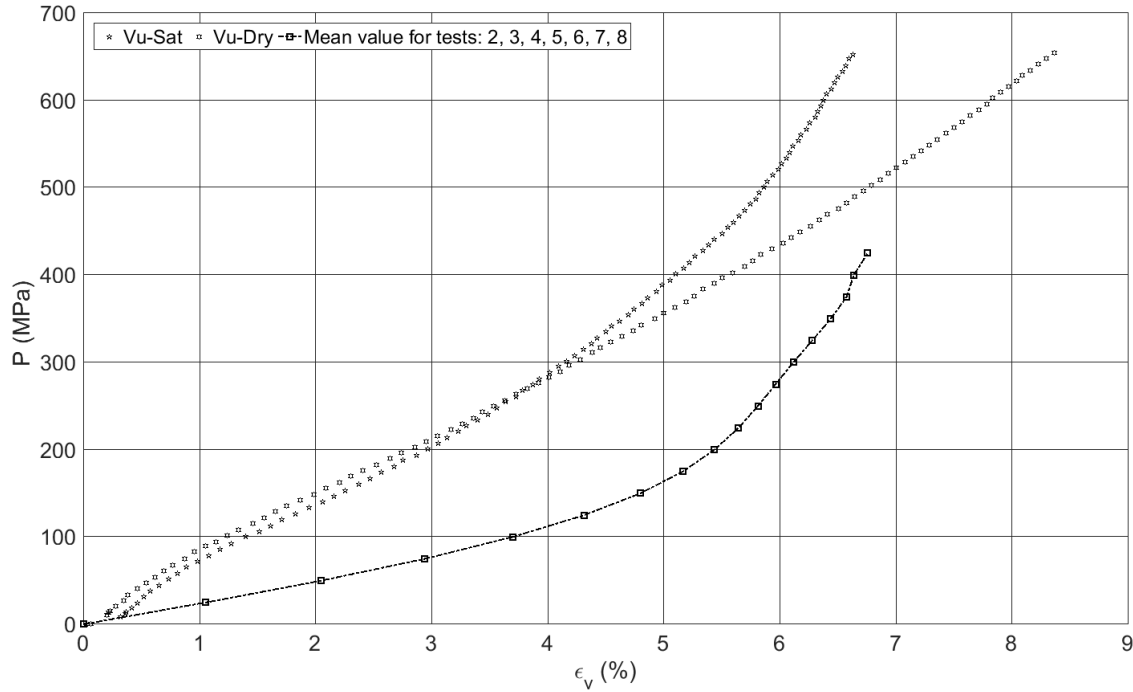


Figure 5.11: Concrete volumetric behavior of dried and saturated concrete [Vu, 2007] along with the mean pore pressure measurement test under hydrostatic loading: pressure vs. volumetric strain

Figure 5.12 depicts the mean curve of the Biot's coefficient based on (eq. 5.7b) versus the volumetric strain along with the maximum values of b for tests 2 to 8. The

Biot's coefficient effect starts to appear very lately for a volumetric strain equal to 3.5 % and remains linear until the end. This is due to the fact that the volumetric behavior of the dried and saturated concrete remain very close until approximately the end of the compaction phase (250 MPa). In addition, the lower the pore pressure is, the higher the b coefficient is, which means that the pore pressure contribution becomes more important.

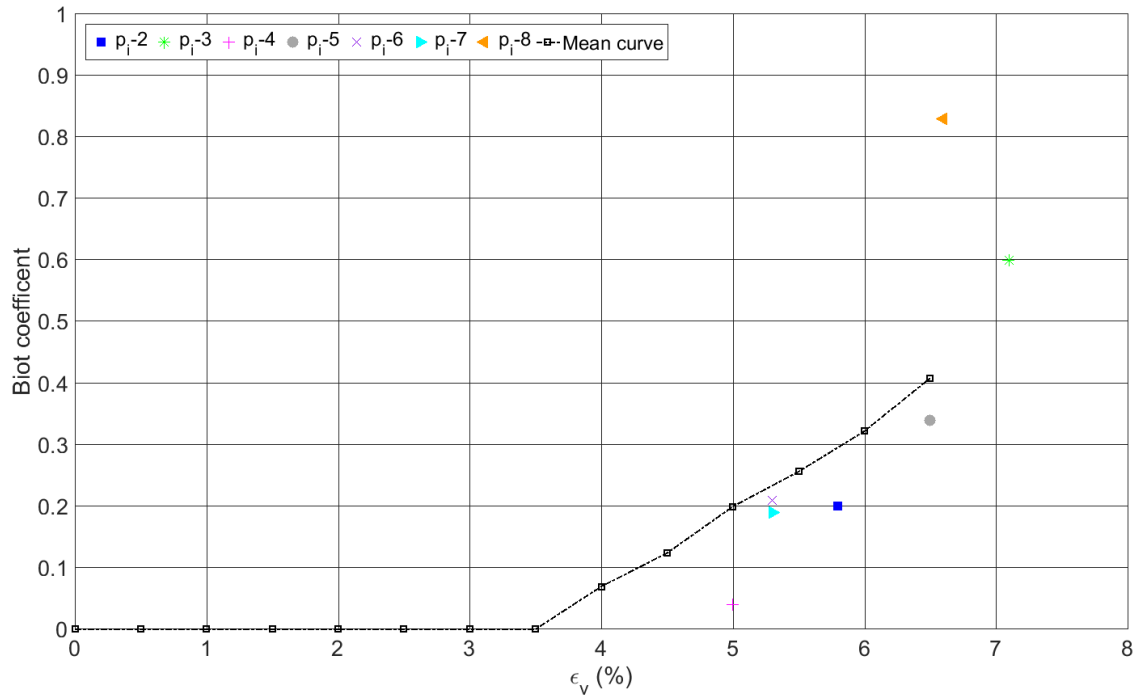


Figure 5.12: Mean value of the Biot's coefficient and maximum Biot's coefficient for each test with respect to the volumetric strain

5.7 Conclusion

In this chapter the concept of the effective stress is reviewed. Two approaches aiming to take into account the influence of pore pressure into concrete under high stress levels is discussed. The mixed law approach (serial or parallel) and the poro-mechanical approach within the framework of the Biot-Coussy theory were well explained. A numerical modeling based on the poro-mechanical concept in which, the effect of pore pressure is taken into account, is developed. The first part of the model was dedicated to evaluate the evolution of the porosity closure whereas the second part is built to estimate concrete pore pressure at high confinement level. After that,

analytical results are compared with experimental ones by changing two parameters at the beginning (the initial concrete porosity and the concrete saturation ratio). The model showed a good capability to reproduce the evolution of the interstitial pore pressure with respect to the applied confinement. In addition, the model has shown a promising results when it is compared with the interstitial pore pressure plotted with respect to the volumetric strain. At the end, an experimental identification of the Biot's coefficient gives us an idea on its evolution under hydrostatic loading.

Conclusion and perspectives

The use of massive structures for safety purpose is still increasing. These structures are mainly made of concrete, an attractive material due to its easy use and high hardness, implemented as a structural and impact-resistant component. The necessity to protect army bunkers and nuclear power plants from missile impact, or civil buildings from natural risks such as tornadoes or earth-quakes, has prompted several studies on concrete under extreme loading conditions. The present work is interested in the hydrostatic behavior of a very wet concrete under high confining level. It comes as continuity for a wider research project started from 2004 to study the effect of triaxial loading on the concrete behavior. In order to complete efforts of previous researchers, the magnitude of the interstitial pore pressure into concrete, which remained unknown under high confining pressure, is measured. The work presented in this thesis consisted in both experimental and modeling investigations.

Bibliographic review provided a general introduction of the thesis project. First, concrete is treated at the meso-scale (e.g: aggregate and matrix) where the behavior of each meso-constituents under high triaxial stress is presented. The effect of the water over cement ratio, initial matrix porosity and saturation ratio have been investigated under several loading paths. It has been shown that the presence of water inside concrete pores has the most significant effect on its behavior under many types of loading (e.g: triaxial, oedometric static tests at high confinement and dynamic shear and tension). Two approaches are presented in order to model the behavior of concrete when subjected to an impact test (e.g: continuous and discrete). Both models reveal that the concrete behavior could be very well reproduced when the effect of water inside concrete is taken into account. At the end, pore pressure measurement technics and poro-mechanical properties identification during triaxial test on geo-materials are highlighted.

The second and third chapters are dedicated to the experimental protocol used in this thesis. From concrete formulation to its preparation for a hydrostatic test, all the steps are clearly explained. A general overview of the Giga press and the available types of tests are also described. It is shown that the press is not equipped with a drainage system so that only undrained test, without pore pressure measurement, can be performed. Therefore, both chapters show the development of a new device aiming to measure the concrete pore pressure under high confining pressure. The assembly is consisted of a water collecting cap having micro-holes to guaranty the water flow, a deformable sensor and a movable plug. The concept, design, calibration and limitation of each sensor are discussed.

The fourth chapter is devoted for the analysis of the results. It has been shown that, the R30A7 concrete pore pressure can reach high values ranging between 250 to 400 MPa under a hydrostatic loading of 500 MPa of confinement. Two trends of pore pressure behavior with respect to the confinement are highlighted. First a linear increase of the pore pressure with respect to the confinement followed by a change in the slope which becomes stiffer. The same behavior of the pore pressure with respect to the volumetric strain is also noticed. The concrete volumetric behavior is evaluated for each sample and compared with both dried and saturated reference one under undrained conditions. Results reveal that, all the volumetric curves lies below the saturated one having a deflection point at 200 MPa of confinement marked by porosity significant closure.

The fifth chapter describes a poro-mechanical model, developed at the macroscopic scale, since neither the parallel nor the serial models are capable to reproduce the concrete behavior when saturated. The macroscopic analytical model is implemented in order to reproduce the porosity closure of concrete and to estimate the concrete volumetric behavior and the pore pressure evolution under high confinement. The model, with its two input parameters: the initial porosity and saturation ratio, shows a good capability to estimate the experimental results. The pore pressure evolution and the concrete volumetric behavior were well reproduced. At the end of this chapter an experimental identification of the Biot's coefficient was carried out. By applying the effective stress concept and based on the poro-mechanical approach the Biot's coefficient was estimated by correcting the volumetric behavior of the dried concrete with the pore pressure value already measured.

Perspectives

This work of measurement and modeling of the interstitial pore pressure in concrete under severe mechanical loading is far from finished and has many perspectives. First, an optimization modeling of the new water collecting cap with membrane effect (presented in chapter 3) can be achieved. This work can lead to the appropriate cap thickness (sensitivity) and the adequate material properties which can resist under the high confinement applied. After that, calibration and interstitial pore pressure measurement tests can be performed on saturated concrete samples. The new results could be then verified with the current study results. Second, the effect of the initial concrete porosity might be studied by performing pore pressure measurement test on concrete sample having different initial porosity. Two concrete types already studied before (already casted also) would be the adequate candidates for the new study. The first one is the light performance concrete (LPC) having very porous structure (porosity $\geq 16\%$) and a high performance concrete (HPC) having a very low porous structure (porosity $\leq 8\%$). Once saturated and since both concretes have a big difference in the quantity of free water stacked inside their pores, a different values of pore pressure measurement can be obtained. Results of these tests could be also compared with the one of the reference concrete. Furthermore, since the deviatoric behavior of concrete is highly influenced by the water presence as shown in the literature, it would be interesting to measure the interstitial pore pressure on very wet concrete under triaxial loading at high confining pressure. So that, the new cap design should take into consideration this kind of loading. At the end, numerical modeling of either finite or discrete elements model can be enhanced by taking into account the evolution of the interstitial pore pressure issued from this study.

Bibliography

- [Akers and Phillips, 2004] Akers, S. A. and Phillips, B. R. (2004). Concrete modeled as an inhomogeneous material: Numerical simulation of contact detonations charges. *In 18th International Symposium on military Aspects of Blast and Shock*.
- [Backers, 2004] Backers, T. (2004). *Fracture Toughness Determination and Micromechanics of Rock Under Mode I and Mode II Loading*. PhD thesis, University of Potsdam, Germany.
- [Baroghel Bouny et al., 1999] Baroghel Bouny, V., Mainguy, M., Lassabatere, T., and Coussy, O. (1999). Characterization and identification of equilibrium and transfer moisture properties for ordinary and high performance cementitious materials. *Cement and Concrete Research*, 29:1225–1238.
- [Bazant et al., 1986] Bazant, Z. P., Bishop, F. C., and Chang, T. (1986). Confined compression tests of cement paste and concrete up to 300 ksi. *ACI journal proceedings*, 83:553–560.
- [Benniou et al., 2016] Benniou, H., Daudeville, L., and Malecot, Y. (2016). *Modélisation par éléments discrets du comportement des matériaux cimentaires sous impact sévère prise en compte du taux de saturation*. PhD thesis, Université Grenoble Alpes.
- [Biot, 1941] Biot, M. (1941). General theory of three-dimensional consolidation. *J Appl Phys.*, 12:155–164.
- [Biot, 1957] Biot, M. (1957). The elastic coefficients of the theory of consolidation. *J Appl Mech.*, 24:594–601.

- [Bischoff and Perry, 1995] Bischoff, P. and Perry, S. (1995). Impact behavior of plain concrete loaded in uniaxial compression. *Journal of Engineering Mechanics*, 121:685–693.
- [Bischoff and Perry, 1991] Bischoff, P. H. and Perry, S. H. (1991). Compressive behaviour of concrete at high strain rates. *Materials and Structures*, 24(6):425–450.
- [Bolomey, 1935] Bolomey, J. (1935). Granulation et prévision de la résistance probable des bétons. *Travaux* 19, 30:228–232.
- [Burlion, 1997] Burlion, N. (1997). *Compaction des bétons: éléments de modélisation et caractérisation expérimentale*. PhD thesis, Ecole Normale Supérieure de Cachan, France.
- [Burlion et al., 1998] Burlion, N., Gatuingt, F., Pijaudier Cabot, G., and Dahan, N. (1998). Concrete under high compaction: a new experimental method. *Fracture mechanics of concrete structures*, pages 605–614.
- [Burlion et al., 2001] Burlion, N., Pijaudier-Cabot, G., and Dahan, N. (2001). Experimental analysis of compaction of concrete and mortar. *International Journal for Numerical and Analytical Methods in Geomechanics*, 25:1467–1486.
- [Camborde, 1999] Camborde, F. (1999). *Modélisation du comportement dynamique du béton. Application aux problèmes d’impacts et d’explosions*. PhD thesis, Laboratoire de Détection et de Géophysique, CEA.
- [Coussy, 1995] Coussy, O. (1995). Mechanics of porous continua. In *New York, NY, USA, 1995*.
- [Cundall and Strack, 1979] Cundall, P.-A. and Strack, O.-D.-L. (1979). A discrete numerical model for granular assemblies. *Geotechnique*, 29:47–65.
- [Daudeville and Malecot, 2011] Daudeville, L. and Malecot, Y. (2011). Concrete structures under impact. *European Journal of Environmental and Civil Engineering*, 15(sup1):101–140.
- [Donzé et al., 2009] Donzé, F.-V., Richefeu, V., and Magnier, S. (2009). Advances in discrete element method applied to soil, rock and concrete mechanics. *Electronic Journal of Geotechnical Engineering*, 8:44.

- [Erzar, 2010] Erzar, B. (2010). *Ecaillage, cratérisation et comportement en traction dynamique de bétons sous impact: approches expérimentales et modélisation*. PhD thesis, Université de Metz.
- [Erzar and Forquin, 2010] Erzar, B. and Forquin, P. (2010). An experimental method to determine the tensile strength of concrete at high rates of strain. *Experimental Mechanics*, 50(7):941–955.
- [Erzar and Forquin, 2011a] Erzar, B. and Forquin, P. (2011a). Experiments and mesoscopic modelling of dynamic testing of concrete. *Mechanics of Materials*, 43(9):505–527.
- [Erzar and Forquin, 2011b] Erzar, B. and Forquin, P. (2011b). Experiments and mesoscopic modelling of dynamic testing of concrete. *Appl. Mech. Mater.*, 43(9):505–527.
- [Erzar and Forquin, 2011c] Erzar, B. and Forquin, P. (2011c). Free water influence on the dynamic tensile behaviour of concrete. *Appl. Mech. Mater.*, 82:45–50.
- [Feret, 1892] Feret, R. (1892). Sur la compacité des mortiers hydrauliques. *Annales des Ponts et Chaussées Série 7*, 4:5–164.
- [Forquin, 2011] Forquin, P. (2011). Influence of free water and strain-rate on the shear behaviour of concrete. *Applied mechanics and materials*, 82:148–153.
- [Forquin and Erzar, 2010] Forquin, P. and Erzar, B. (2010). Dynamic fragmentation process in concrete under impact and spalling tests. *International Journal of Fracture*, 1-2:193–215.
- [Forquin et al., 2013] Forquin, P., Piotrowska, E., and Gary, G. (2013). Experimental characterization of the confined behaviour of concrete . influence of saturation ratio and strain-rate. Technical report, Université Grenoble alpes3Sr laboratory.
- [Forquin and Sallier, 2013] Forquin, P. and Sallier, L. (2013). A testing technique to characterise the shear behaviour of concrete at high strain rates. *Dynamic behavior of materials*, 1:531–536.
- [Forquina et al., 2008] Forquina, P., Gary, G., and Gatuingt, F. (2008). A testing technique for concrete under confinement at high rates of strain. *International Journal of Impact Engineering*, 35:425–446.

- [Frangin, 2008] Frangin, E. (2008). *Adaptation de la méthode des éléments discrets à l'échelle de l'ouvrage en béton armé : une approche couplée éléments discrets/éléments finis*. PhD thesis, Université Joseph Fourier, Grenoble.
- [Gabet, 2006] Gabet, T. (2006). *Comportement triaxial du béton sous fortes contraintes : Influence du trajet de chargement*. PhD thesis, Université Joseph Fourier.
- [Gabet et al., 2008] Gabet, T., Malecot, Y., and Daudeville, L. (2008). Triaxial behaviour of concrete under high stresses: Influence of the loading path on compaction and limit states. *Cement and Concrete Research*, 38(3):403–412.
- [Ghabezloo et al., 2012] Ghabezloo, G., Sulem, J., Guédon, S., Martineau, F., and Saint-Marc, J. (2012). Poromechanical behavior of hardened cement paste under isotropic loading. *Cement and Concrete Research*, 42:789–797.
- [Gran and Frew, 1979] Gran, J. K. and Frew, D. J. (1979). In-target radial stress measurements from penetration experiments into concrete by ogive-nose steel projects. *International Journal of Impact Engineering*, 19:715–726.
- [Hart, 2000] Hart, D. J. (2000). *Laboratory measurements of poroelastic constants and flow parameters and some associated phenomena*. PhD thesis, University of Wisconsin—Madison.
- [Hentz et al., 2004] Hentz, S., Donzé, F.-V., and Daudeville, L. (2004). Identification and validation of a discrete element model for concrete. *Journal of Engineering Mechanics*, 130(6):709–719.
- [Hentz et al., 2005] Hentz, S., Donzé, F.-V., and Daudeville, L. (2005). Discrete elements modeling of a reinforced concrete structure submitted to a rock impact. *Italian Geotechnical Journal*, 39(4):83–94.
- [Heukamp et al., 2001] Heukamp, F. H., Ulm, F. J., and Germaine, J. T. (2001). Mechanical properties of calcium-leached cement pastes triaxial stress states and the influence of the pore pressures. *Cement and Concrete research*, 31:767–774.
- [Hild, 2015] Hild, F. (2015). Mechanics of materials on characteristic parameters involved in dynamic fragmentation processes. *Mechanics of Materials*, 80:340–350.
- [Hu and Skoczylas, 2017] Hu, C. and Skoczylas, F. (2017). Poro-mechanical properties evolution under hydrostatic stress after induced damage. *23eme Congrès Français de Mécanique, Lille, 28 Août au 1er Septembre 2017*.

- [Hughes, 1984] Hughes, G. (1984). Hard missile impact on reinforced concrete. *Nuclear Engineering and Design*, 77(1):23–35.
- [Ingraham et al., 2017] Ingraham, M. D., D.Bauer, S., J.Issen, K., and Dewers, T. (2017). Evolution of permeability and biot coefficient at high mean stresses in high porosity sandstone. *International Journal of Rock Mechanics and Mining Sciences*, 96:1–10.
- [Kendall et al., 1983] Kendall, K., Howard, A., Birchall, J., Pratt, P., B.A., P., and S.A., J. (1983). The relation between porosity, microstructure and strength, and the approach to advanced cement-based materials. *Phil. Trans. R. Soc. Lond. A*, 310:139-153.
- [Klepaczko and Brara, 2001] Klepaczko, J. and Brara, A. (2001). An experimental method for dynamic tensile testing of concrete by spalling. *International Journal of Impact Engineering*, 25:387–409.
- [Kolsky, 1949] Kolsky, H. (1949). An investigation of the mechanical properties of materials at very high rates of loading. Technical report, Proceedings of the Physical Society.
- [Krieg, 2002] Krieg, R. D. (2002). A simple constitutive description for soils and crushable foams. Technical report, Sandia National Laboratories report, SC-DR-72-0833, Albuquerque, New Mexico.
- [Li et al., 2005] Li, Q. M., Reid, S. R., Wen, H. M., and Telford, A. R. (2005). Local impact effects of hard missiles on concrete targets. *International Journal of Fracture*, 32:224–284.
- [Ling et al., 2016] Ling, K., He, J. P., and S., P. W. (2016). Comparisons of biot’s coefficients of bakken core samples measured by three methods comparisons of biot’s coefficients of bakken core samples measured by three methods. *The 50th US Rock Mechanics / Geomechanics Symposium, Houston, Texas, USA*.
- [Luding, 2008] Luding, S. (2008). Introduction to discrete element methods. *Discrete modelling of geomaterials*, 12(7):785–826.
- [Malecot, 2009] Malecot, Y. (2009). Modélisation du comportement triaxial du béton sous très forte contrainte : prise en compte du taux de saturation et de la composition du béton. Technical report, University of Colorado, Boulder.

- [Malvar and Ross, 1998] Malvar, L. and Ross, C. (1998). Review of strain rate effects for concrete in tension. *Materials Journal*, 95(6):735–739.
- [Mazars, 1984] Mazars, J. (1984). *Application de la mécanique de l'endommagement au comportement non linéaire et à la rupture du béton de structure*. PhD thesis, Université de Paris VI.
- [Mellinger and Birkimer, 1966] Mellinger, F. and Birkimer, D. (1966). Measurements of stress and strain on cylindrical test specimens of rock and concrete under impact loading. Technical report, DEPARTMENT OF THE ARMY, Ohio River Division Laboratories, Corps of Engineers.
- [Montenegro and Carol, 2007] Montenegro, O. and Carol, I. (2007). Fracture toughness test for soil-cement samples in mode ii. *ICEM13 conference, Alexandroupolis, Greece*.
- [Nowakowski, 2012] Nowakowski, A. (2012). The law of effective stress for rocks in light of results of laboratory experiments. *Archives of Mining Sciences*, 57:1027–1044.
- [Ozbolt et al., 2014] Ozbolt, J., Sharma, A., Irhan, B., and Sola, E. (2014). Tensile behavior of concrete under high loading rates. *International Journal of Impact Engineering*, 69:55–68.
- [Ozbolt et al., 2013] Ozbolt, J., Weerheijm, J., and Sharma, A. (2013). Dynamic tensile resistance of concrete – split hopkinson bar test. *VIII International Conference on Fracture Mechanics of Concrete and Concrete Structures*.
- [Piotrowska and Forquin, 2014] Piotrowska, E. and Forquin, P. (2014). Dynamic behavior of high strength concrete in quasi oedometric compression test: experimental investigation. Technical report, Université Grenoble alpes.
- [Poinard et al., 2012] Poinard, C., Piotrowska, E., Malecot, Y., Daudeville, L., and Landis, E. (2012). Compression triaxial behavior of concrete: the role of the mesostructure by analysis of x-ray tomographic images. *European Journal of Environmental and Civil Engineering*, 16 (supp. 1):115–136.
- [Poirier, 1996] Poirier, S. (1996). *Etude expérimentale du comportement de la pression interstitielle et de son influence sur le comportement physico-mécanique d'un*

- matériau poreux intact ou fracturé par essais triaxiaux non-drainés*. PhD thesis, Université du Québec, Chicoutimi.
- [Pontiroli et al., 2004] Pontiroli, C., Rouquand, A., and Mazars, J. (2004). Predicting concrete behaviour from quasi-static loading to hypervelocity impact. an overview of the prm model. *European Journal of Environmental and Civil Engineering*, 14(6-7):703–727.
- [Pontiroli et al., 2010] Pontiroli, C., Rouquand, A., and Mazars, J. (2010). Predicting concrete behaviour from quasi-static loading to hypervelocity impact. an overview of the prm model. *European Journal of Environmental and Civil Engineering*, 14(6-7):703–727.
- [Pontiroli et al., 2015] Pontiroli, C., Rouquand, A., and Mazars, J. (2015). Concrete behaviour under ballistic impacts: effects of materials parameters to penetration resistance and modeling with prm model. *Conference: Computational Modeling of Concrete and Concrete Structures (EURO-C 2014)*.
- [Rouquand, 2002] Rouquand, A. (2002). Présentation d’un modèle du comportement du béton et des géomatériaux, application au calcul de structures et aux effets des armes conventionnelles. Technical report, Délégation Générale pour l’Armement, Centre d’études de Gramat.
- [Rousseau, 2009] Rousseau, J. (2009). *Modélisation numérique du comportement dynamique de structures sous impact sévère avec un couplage éléments discrets / éléments finis*. PhD thesis, Université Joseph Fourier, Grenoble.
- [Safa et al., 2010] Safa, K., Forquin, P., and Gary, G. (2010). Influence of free water on the quasi-static and dynamic strength of concrete in confined compression tests. *Cement and Concrete Research*, 40:321–333.
- [Schuler, 2007] Schuler, H. (2007). Evaluation of an experimental method via numerical simulations. *International conference on fracture mechanics of concrete and concrete structures*, pages 607–611.
- [Schuler et al., 2006] Schuler, H., Mayrhofer, C., and Thoma, K. (2006). Spall experiments for the measurement of the tensile strength and fracture energy of concrete at high strain rates. *International Journal of Impact Engineering*, 32:1635–1650.

- [Sfer et al., 2002] Sfer, D., Carol, I., Gettu, R., and Etse, G. (2002). Study of the Behavior of Concrete under Triaxial Compression. *Journal of Engineering Mechanics*, 128:156–163.
- [Shiu, 2008] Shiu, W.-J. (2008). *Impact de missiles rigides sur structures en béton armé : analyse par la méthode des éléments discrets*. PhD thesis, Université Joseph Fourier - Grenoble 1.
- [Sulem and Ouffroukh, 2005] Sulem, J. and Ouffroukh, H. (2005). Shear banding in drained and undrained triaxial tests on saturated sandstone: porosity and permeability evolution. *International Journal of Rocks Mechanics and Mining Sciences*, 43:292–310.
- [Swenson and Taylor, 1983] Swenson, D. V. and Taylor, L. M. (1983). A finite element model for the analysis of tailored pulse simulation of boreholes. *International Journal for Numerical and Analytical Methods in Geo-mechanics*, 7-4:469–48.
- [Terzaghi, 1936] Terzaghi, K. (1936). The shearing resistance of saturated soils and the angle between planes of shear. In: *Proc. Int. Conf. Soil Mech. And Found. Eng., Casagrande, A. and Rutledge P.C. and Watson J.D. (eds), Harvard University*, I:54–56.
- [Thiot-ingénierie, 2004] Thiot-ingénierie (2004). La croix blanche 46130 saint michel loubéjou. Technical report.
- [Tran et al., 2012] Tran, V.-T., Donzé, F.-V., and Chareyre, B. (2012). Numerical simulation of saturated and non-saturated concretes under high confining pressure using coupled fluid flow–discrete element model, university of technical education ho chi minh city. In *The 2012 International Conference on Green Technology and Sustainable Development (GTSD2012)*.
- [Tran et al., 2011] Tran, V.-T., Donzé, F.-V., and Marin, P. (2011). A discrete element model of concrete under high triaxial loading. *Cement and Concrete Composites*, 33(9):936–948.
- [Ulm et al., 2004] Ulm, F. J., Constantinides, G., and Heukamp, F. H. (2004). Is concrete a poromechanics material? a multiscale investigation of poroelastic properties. *Material and structures*, 37:256:43–58.

- [Vu, 2013] Vu, X.-D. (2013). *Study of the behavior of concrete slabs subjected to impact : characterization of the material behavior, modeling and validation*. PhD thesis, Université Joseph Fourier.
- [Vu, 2007] Vu, X.-H. (2007). *Caractérisation expérimentale du béton sous fort confinement : influences du degré de saturation et du rapport eau/ciment*. PhD thesis, Université Joseph Fourier.
- [Vu et al., 2009] Vu, X.-H., Malecot, Y., Daudeville, L., and Buzaud, E. (2009). Experimental analysis of concrete behavior under high confinement: effect of the saturation ratio. *International Journal of Solids and Structures*, 46:1105–1120.
- [Watkins, 1983] Watkins, J. (1983). Fracture toughness test for soil-cement samples in mode ii. *Int. J. Fract.*, 23:135–138.
- [William and William, 1992] William, M. M. and William, R. M. (1992). The bonded electrical resistance strain gage. Technical report, Oxford University Press; 1 edition, April 30.
- [Yurtdas et al., 2005] Yurtdas, I., Peng, H., Burlion, N., and Skoczylas, F. (2005). Influence of water by cement ratio on mechanical properties of mortars submitted of drying. *Cement and Concrete Research*.
- [Zimmerman, 2000] Zimmerman, R. (2000). Coupling in poroelasticity and thermoelasticity. *International Journal of Rock Mechanics and Mining Sciences*, 37:79–87.
- [Zimmerman et al., 1957] Zimmerman, R., Somerton, W. H., and King, M. S. (1957). Compressibility of porous rocks. *Journal of Geophysical Research*, 91:12765–12777.
- [Zingg, 2013] Zingg, L. (2013). *Influence de la porosité et du degré d'humidité interne sur le comportement triaxial du béton*. PhD thesis, Université de Grenoble.
- [Zingg et al., 2016] Zingg, L., Baroth, J., and Malecot, Y. (2016). Influence of cement matrix porosity on the triaxial behaviour of concrete. *Cement and Concrete Research*, 80:52–59.
- [Zukas, 1992] Zukas, J. A. (1992). Penetration and perforation of solids, impact dynamics. Technical report, Krieger Publishing Company.

List of Figures

1	Missile impact effects on concrete target: (a) penetration (b) cone cracking (c) spalling (d) cracks on (i) proximal face and (ii) distal face (e) scabbing (f) perforation and (g) overall target response, [Li et al., 2005]	1
2	Horizontal slice of the R30A7 sample for an hydrostatic cyclic loading: (a) initial state (b) at 200 MPa (c) 400 MPa (d) 650 MPa, [Poinard et al., 2012]	2
3	Lower cap equipped with a pressure transducer, [Hart, 2000]	4
1.1	Volumetric behavior in hydrostatic test for three materials: limestone rocks, SAM21 concrete and mortar, [Akers and Phillips, 2004]	6
1.2	Mechanical behavior of the limestone rocks, SAM21 concrete and mortar subjected to: (left) simple compression test (right) triaxial test at 300 MPa of confinement, [Akers and Phillips, 2004]	7
1.3	Simple compression tests with different(W/C) ratios: (left) R30A7 concrete, [Vu, 2007] (right) mortar samples, [Yurtdas et al., 2005]	8
1.4	Simple compression tests on R30A7, LP and HP concretes with different initial matrix porosities (ϕ_0): (left) axial stress vs. strains (right) mean stress vs. volumetric strain, [Zingg et al., 2016]	9
1.5	Simple compression test compression with different saturation ratios (S_r): (left) R30A7, [Vu, 2007] (right) HP concrete, [Zingg, 2013]	9
1.6	Triaxial test concept: (a) loading path (b) sample device used for strain measurement	11

1.7	Volumetric behavior of ordinary concrete with different W/C ratio under triaxial loading. Mean stress vs. volumetric strain at: (left) 100 MPa (right) 600 MPa of confinement, [Vu, 2007]	12
1.8	Deviatoric behavior of ordinary concrete with different W/C ratio under triaxial loading. Deviatoric stress vs. strains at: (left) 100 MPa (right) 600 MPa of confinement, [Vu, 2007]	12
1.9	Volumetric behavior of R30A7, LP and HP concretes. Mean stress vs. volumetric strain at: (left) 50 MPa (right) 600 MPa of confinement, [Zingg et al., 2016]	13
1.10	Deviatoric behavior of concretes of R30A7, LP and HP concretes. Deviatoric stress vs. axial strain under: 50 MPa (left) (right) 600 MPa of confinement, [Zingg et al., 2016]	13
1.11	Results of triaxial tests on O, LP and HP concretes at the (left) saturated and (right) dried states. Mean stress vs. volumetric strain under: (a) 100 MPa (b) 600 MPa of confinement, [Zingg, 2013]	14
1.12	Stress limits states. Deviatoric stress vs. mean stress: (a) Ordinary (b) Low performance (c) High performance concretes, [Zingg et al., 2016]	16
1.13	Concrete specimen jacketed by the steel confinement cell during quasi-oedometric confined test, [Burlion et al., 1998]	16
1.14	Quasi-oedometric tests on ordinary concrete with different saturation ratio: (left) mean stress vs. volumetric strain (right) deviatoric stress vs. mean stress, [Forquin et al., 2013]	17
1.15	Quasi-oedometric tests on high performance concrete with different saturation ratio: (left) mean stress vs. volumetric strain (right) deviatoric stress vs. mean stress, [Piotrowska and Forquin, 2014]	18
1.16	Set up of a quasi-oedometric test using the SHPB technique, [Forquina et al., 2008]	19
1.17	Dynamic quasi-oedometric test on ordinary and high performance concretes. Mean stress vs. volumetric strain: (left) dry (right) saturated states, [Piotrowska and Forquin, 2014]	19
1.18	Dynamic quasi-oedometric test on ordinary and high performance concrete. Deviatoric stress vs. mean stress: (left) dry (right) saturated states, [Piotrowska and Forquin, 2014]	19
1.19	Dynamic quasi-oedometric test on the MB50 concrete at the dry and saturated states: (left) mean stress vs. volumetric strain (right) deviatoric stress vs. mean stress, [Safa et al., 2010]	20

1.20	Quasi-static and dynamic PTS tests on dry and saturated ordinary concrete: shear strength vs. strain rate, [Forquin, 2011]	21
1.21	Spalling test device and instrumentation: projectile, input bar, specimen and strain gages, [Erzar, 2010]	22
1.22	Quasi-static and dynamic tensile tests: tensile strength vs. strain rate for both dry and saturated ordinary and MB50 concretes, [Erzar and Forquin, 2011a]	22
1.23	Experimental and numerical (FEM) comparison: (left) hydrostatic results on saturated concrete (right) triaxial results on dried concrete, [Pontiroli et al., 2015]	26
1.24	Experimental and numerical (FEM) comparison of 800 mm thick target with impact velocity 347 m/s: axial deceleration vs. time, [Pontiroli et al., 2015]	26
1.25	Experimental and numerical (DEM) comparison: (left) hydrostatic results (right) triaxial results on dried and saturated concretes, [Benniou et al., 2016]	27
1.26	Experimental and numerical (DEM) comparison of 800 mm thick target with impact velocity 347 m/s: axial deceleration vs. time, [Benniou et al., 2016]	28
1.27	Assembly of the triaxial press, [Poirier, 1996]	29
1.28	Concrete pore pressure evolution vs. deviatoric stress for different confinement pressure, [Poirier, 1996]	30
1.29	Drained tests on rock: (a) deviatoric stress vs. strains (b) volumetric strain vs. axial strain, [Sulem and Ouffroukh, 2005]	31
1.30	Undrained tests on rock: (a) deviatoric stress vs. strains (b) volumetric strain vs. axial strain, [Sulem and Ouffroukh, 2005]	31
1.31	Undrained tests on rock: pore pressure vs. axial strain, [Sulem and Ouffroukh, 2005]	32
1.32	Triaxial tests on sandstone rock: (a) Biot's coefficient (b) pore pressure evolutions versus the differential stress, [Nowakowski, 2012]	33
2.1	Preparation stages: (left) coring of concrete block and samples extraction (middle) concrete surface treatment (right) samples conservation into a saturated environment	37

2.2	Porosity measurement: (left) dry, saturated and submerged sample masses (right) experimental set up used to measure concrete submerged mass	38
2.3	Schenck Press: (left) general view (right) instrumentation of a concrete specimen by using the circular steel collar	39
2.4	Results of the simple compression test on the ordinary concrete: axial stress vs. strains	40
2.5	Overview of the triaxial press GIGA	41
2.6	Schematic illustration of the triaxial press GIGA: (left) general scheme of the press (right): cross-sectional view of the confining cell	42
2.7	Available loading path of the triaxial press GIGA	42
2.8	LVDT calibration test: (left) 14 cm (right) 8 cm specimen length	45
2.9	Calibration test result on a steel specimen of 8 cm in length: confinement pressure vs. gage and LVDT displacements	45
2.10	Principal caps dimensions and shapes adapted for both sample lengths and diameters: (a) 10.5 by 5 cm (b) 14 by 7 cm	46
2.11	Provisional concept: (left) set up before modification (right) modified set up with principal cap and water collect cavity combination	47
2.12	Recent concept with the water collect cap integration	48
2.13	Drainage cap with micro-holes, plug and sealing joint (left) design (right) real concept	48
2.14	Device protection with multiple-layer of <i>Latex & noprne</i> membranes	49
2.15	concrete surface porosity and <i>Sikatop</i> application: (a) before (b) after	49
2.16	Sample and water collect cap arrangement and concept: (left) calibration test on perforated aluminum sample (right) pore pressure test on concrete	50
2.17	Previous results: (left) drainage cap equipped with sensor (right) calibration test result: confining pressure vs. plate strain, [Zingg, 2013]	51
3.1	Aluminum sensor type hydrostatic: (left) sectional plan of the cap with the hydrostatic load sensor (right) size and loading type of the cylindrical sensor	54
3.2	Picture of the aluminum sensor type hydrostatic: (left) water collect cap, plug, sealing joint and the hydrostatic sensor (right) sensor placed inside the water collecting cap	55

3.3	Hydrostatic type sensor: reversed calibration test (left) design (right) real picture	56
3.4	Hydrostatic type sensor: normal calibration test design	57
3.5	Experimental procedure: (left) sponge attached on concrete lower surface (middle) applying of protective membranes (right) saturation of the water collecting cap before the test	57
3.6	Device weak points: (left) membrane penetration (right) wires cut at cap/specimen interface	58
3.7	Device protection: (c,d) wires passage protection (e) protective membrane at the interface (f) gage protection	59
3.8	Calibration test results on the aluminum sensor type hydrostatic: hydrostatic loading pressure p_c vs. sensor volumetric deformation ϵ_v (positive in compression)	60
3.9	First interstitial pore pressure measurement results on R30A7 concrete: pore pressure vs. confining pressure	62
3.10	Hydrostatic test on saturated R30A7 samples: pore pressure vs. confining pressure	63
3.11	Steel sensor type membrane (a) sectional plan of the cap with the membrane sensor (b) picture of the cap with the membrane sensor	64
3.12	General design of the membrane sensor with the gage and sealing joint positions	65
3.13	The design and geometry of different suggested sensors (left) s1 (middle) s2 (right) s3	65
3.14	Applied pore pressure p_i on the sensor upper surface (left) all nodes blocked vertically (right) half nodes blocked vertically	66
3.15	Mechanical effect on the water collect cap lateral surface with the boundary condition: displacement u_{pc} due to the confining pressure	67
3.16	Mechanical effect on the sensor lateral surface: transmitted displacement from the cap to the sensor (left) all nodes fixed (right) half nodes fixed	67
3.17	Sensor Von Misses stress distribution for 400 MPa of water pressure and both kind of boundary conditions. Left column nodes are all fixed, right column half of nodes are fixed: (a) s1 (b) s2 (c) s3	69
3.18	Sensor sensitivity: strains comparison for the three types of sensor for both boundary conditions: applied pressure vs. radial (or tangential) strain at the sensor center back face, (positive strain in tension)	70

3.19	Sensor radial (or tangential) strain field at the sensor central part calculated for 400 MPa of pressure for both boundary conditions. Left column all nodes fixed, right column half nodes fixed: (a) s1 (b) s2 (c) s3	71
3.20	Water collect cap displacement for 400 MPa of pressure: simulation result of the lateral displacement field	72
3.21	Water collect cap displacement for 400 MPa of pressure: applied pressure vs. cap inner displacement with and without counting the tolerance	73
3.22	Sensor <i>s2</i> radial (tangential) strain field at the central part for an applied displacement ($u_{pc} + u_{tol.}$) equal to -0.0268 mm: (left) all nodes (right) half nodes fixed	73
3.23	Mechanical effect on the sensor sensitivity after applying the tolerance: p_c vs. $\epsilon < 0$ in compression	74
3.24	Calibration and mechanical effect on the sensor sensitivity after applying the tolerance: p vs. strain ϵ	74
3.25	Sensor protection (a) joints made of two sub-items (b) joint insertion (c) application of the metal clamp (d) aluminum grooved shield . . .	75
3.26	Test preparation: (left) cap saturation (right) sensor insertion	76
3.27	Test preparation: (left) application of the wires protective metal clamp shield (right) sensor lifting device	77
3.28	Diaphragm pattern (a) strains distribution for a clamped membrane (b) radial and tangential gages overview (c) full bridge configuration .	78
3.29	Membrane type sensor: normal calibration test (left): design (right): real picture	80
3.30	Calibration test results using the membrane sensor equipped with a diaphragm pattern: confining pressure vs. strain sensor	80
3.31	Lost of diaphragm pattern: (left) wires cut (right) gage detached . . .	81
3.32	Single radial gage: (left) support and cosse gluing with wires welding (right) gage protection	81
3.33	Membrane type sensor: principal of the mechanical effect (left): design (right): real picture	83
3.34	Experimental results of calibration test compared with the numerical calculations during a hydrostatic test	83
3.35	Pore pressure result on R30A7 concrete: pore pressure vs. confining pressure	84
3.36	Comparison between the hydrostatic type and membrane sensor deformations: applied pressure vs. strain	85

3.37	Design of pore pressure water collecting cap working on the membrane effect: (left) sectional view with a micro-holed cap equipped with a threaded hole, cap lower part, strain gage position (right) top view of the cap upper part	86
3.38	Water collecting cap with membrane effect: (left) real photo (right) gage application	87
4.1	Results of interstitial pore pressure measurement on the R30A7 concrete using the hydrostatic and the membrane type sensors: p_i vs. σ_m	91
4.2	Results of interstitial pore pressure measurement on the reference concrete. Zoom on the first part of the plot: p_i vs. σ_m	92
4.3	Mean value of the interstitial pore pressure measurement and maximum pore pressure reached for each test with respect to the applied confining pressure	92
4.4	Results of interstitial pore pressure measurement with different loading rates on the reference concrete using the hydrostatic type and the membrane type sensor: p_i vs. σ_m	93
4.5	Volumetric behavior of concrete under hydrostatic loading during pore pressure measurements. Comparison with the two references concrete: p_c vs. σ_m	95
4.6	Mean volumetric behavior curve under hydrostatic loading during pore pressure measurements. Comparison with the two references concrete: p_c vs. σ_m	95
4.7	Pore pressure evolution with respect to concrete volumetric deformation	96
4.8	Mean value of the interstitial pore pressure measurement and maximum pore pressure reached for each test with respect to the volumetric strain	97
5.1	PRM coupled model with saturation ratio effect on the concrete: (a) volumetric behavior (b) deviatoric stress	100
5.2	Schematic representation of: (left) serial (right) parallel model [Vu, 2013]	101
5.3	Concrete behavior for different saturation ratios under hydrostatic loading: mean stress vs. volumetric strain. Results comparison with PRM (a) serial (b) parallel model, [Malecot, 2009]	102
5.4	The porous medium matrix as the superposition of two continuous media: a skeleton particle and a fluid particle, [Coussy, 1995]	103

5.5	Cyclic hydrostatic test up to 600 MPa on the R30A7 concrete: (left) volumetric behavior (right) evolution of concrete bulk modulus [Poinard et al., 2012]	105
5.6	Evolution of the concrete bulk modulus: (left) comparison between the model and the experimental curve (right) opened pores with respect to the plastic strain for both initial porosities	107
5.7	Concrete pore pressure modeling in concrete under hydrostatic loading: pore pressure vs. mean stress for different saturation ratios and initial porosities	110
5.8	Concrete volumetric behavior modeling under hydrostatic pressure: mean stress vs. volumetric strain for different saturation ratios and initial porosity compared with the dry and saturated R30A7	111
5.9	Concrete behavior under hydrostatic loading. Interstitial pore pressure vs. mean pressure: (a) experimental measurement with variation range and poro-mechanical modeling (b) zoom on the first part	112
5.10	Concrete behavior under hydrostatic loading. Interstitial pore pressure vs. volumetric strain: experimental measurement with variation range and poro-mechanical modeling	113
5.11	Concrete volumetric behavior of dried and saturated concrete [Vu, 2007] along with the mean pore pressure measurement test under hydrostatic loading: pressure vs. volumetric strain	114
5.12	Mean value of the Biot's coefficient and maximum Biot's coefficient for each test with respect to the volumetric strain	115

List of Tables

1.1	Summary of different tests available in the literature showing the influence of saturation ratio (S_r), water over cement ratio (W/C), initial porosity (ϕ_0) and strain rate ($\dot{\epsilon}$) where (SC) simple compression, (TXT) triaxial, (S-QOC and D-QOC) static or dynamic quasi oedometric compression, (D-S and D-T) dynamic shear or tensile tests. O, LP and HP: ordinary, low and high performance concretes. σ_c , σ_m , σ_s , σ_t and q are the: compressive, mean, shear, tensile and deviatoric strengths. NI, SI and HI means: no, slight and high influence	23
2.1	Ordinary concrete sample mass for the three states: dry, saturated and submerged with porosity accessible to water estimation	39
2.2	Mechanical properties of the ordinary concrete	40
3.1	Description of calibration test: sample/cap configuration, condition and identified slope value	60
3.2	Description of the preliminary hydrostatic test on concrete using the hydrostatic sensor type: test name, concrete type, loading time, test condition, maximum interstitial pore pressure	61
3.3	Description of the preliminary hydrostatic test on concrete using the hydrostatic sensor type: test name, concrete type, loading time, test condition, maximum interstitial pore pressure	63
3.4	The dimensions of the different proposed sensors (in mm)	65
3.5	The maximum Von Misses stress for the three types of sensor for both boundary conditions	69
3.6	Calculation details: cap displacement and sensor deformation	72

3.7	Analytical and simulation results with the resultant gage strain ϵ in (μ_m/m)	79
3.8	Details of calibration test using the diaphragm pattern	79
3.9	Tests description performed on the membrane sensor using a single gage	82
3.10	Pore pressure test description using the single gage	84
4.1	Summary of the pore pressure measurement tests for both sensors type	90
5.1	Parameters for porosity closure estimation	106
5.2	Parameters for pore pressure estimation	109
5.3	Values of saturation ratios and initial porosities used in the modeling	109